

1 SPECIAL COLLECTION

2 ISOTOPES, MINERALS, AND PETROLOGY: HONORING JOHN VALLEY

3  
4 Cui et al., 2018 American Mineralogist

5  
6 **Questioning the Biogenicity of Neoproterozoic Superheavy Pyrite by SIMS**

7  
8 Huan Cui<sup>1,2</sup>, Kouki Kitajima<sup>1,2</sup>, Michael J. Spicuzza<sup>1,2</sup>, John H. Fournelle<sup>1</sup>, Adam Denny<sup>2</sup>, Akizumi  
9 Ishida<sup>1,2,3</sup>, Feifei Zhang<sup>4</sup>, John W. Valley<sup>1,2</sup>

10 <sup>1</sup> NASA Astrobiology Institute, University of Wisconsin, Madison, Wisconsin 53706, USA

11 <sup>2</sup> Department of Geoscience, University of Wisconsin, Madison, Wisconsin 53706, USA

12 <sup>3</sup> Department of Earth Science, Tohoku University, Sendai, Miyagi Prefecture 980-8577, Japan

13 <sup>4</sup> School of Earth and Space Exploration, Arizona State University, Tempe, Arizona 85287, USA

14  
15 \*Corresponding author: [Huan.Cui@wisc.edu](mailto:Huan.Cui@wisc.edu) (H. Cui)

16  
17 **ABSTRACT**

18 The Neoproterozoic sulfur isotope ( $\delta^{34}\text{S}$ ) record is characterized by anomalously high  $\delta^{34}\text{S}_{\text{pyrite}}$   
19 values. Many  $\delta^{34}\text{S}_{\text{pyrite}}$  values are higher than the contemporaneous  $\delta^{34}\text{S}_{\text{sulfate}}$  (i.e.,  $\delta^{34}\text{S}_{\text{pyrite}} > \delta^{34}\text{S}_{\text{sulfate}}$ ),  
20 showing reversed fractionation. This phenomenon has been reported from the Neoproterozoic post-glacial  
21 strata globally and is called “Neoproterozoic superheavy pyrite”. The commonly assumed biogenic  
22 genesis of superheavy pyrite conflicts with current understanding of the marine sulfur cycle. Various  
23 models have been proposed to interpret this phenomenon, including extremely low concentrations of  
24 sulfate in seawaters or porewaters, or the existence of a geographically isolated and geochemically  
25 stratified ocean. Implicit and fundamental in all these published models is the assumption of a biogenic  
26 origin for pyrite genesis, which hypothesizes that the superheavy pyrite is syngenetic (in water column) or  
27 early diagenetic (in shallow marine sediments) in origin and formed via microbial sulfate reduction  
28 (MSR). In this study, the Cryogenian Datangpo Formation in South China, which preserves some of the  
29 highest  $\delta^{34}\text{S}_{\text{pyrite}}$  values up to +70‰, is studied by secondary ion mass spectrometry (SIMS) at  
30 unprecedented spatial resolutions (2  $\mu\text{m}$ ). Based on textures and the new sulfur isotope results, we  
31 propose that the Datangpo superheavy pyrite formed via thermochemical sulfate reduction (TSR) in  
32 hydrothermal fluids during late burial diagenesis, and therefore lacks a biogeochemical connection to the  
33 Neoproterozoic sulfur cycle. Our study demonstrates that SEM-SIMS is an effective approach to assess  
34 the genesis of sedimentary pyrite using combined SEM petrography and  $\mu\text{m}$ -scale  $\delta^{34}\text{S}$  measurements by  
35 SIMS. The possibility that pervasive TSR has overprinted the primary  $\delta^{34}\text{S}_{\text{pyrite}}$  signals during late  
36 diagenesis in other localities may necessitate the reappraisal of some of the  $\delta^{34}\text{S}_{\text{pyrite}}$  profiles associated  
37 with superheavy pyrite throughout Earth's history.

38 **Key words:** microbial sulfate reduction (MSR), thermochemical sulfate reduction (TSR), secondary ion  
39 mass spectrometry (SIMS), scanning electron microscopy (SEM), sulfur isotopes, framboidal pyrite

40  
41 **INTRODUCTION**

42 The Neoproterozoic Era (1000–541 Ma) marks a transitional period in Earth's history that is  
43 characterized by a considerable rise in atmospheric oxygen, a gradual transformation in ocean redox  
44 conditions, and the rise of animal life (Halverson and Shields-Zhou, 2011; Narbonne et al., 2012; Shields-  
45 Zhou et al., 2012; Xiao, 2014). Notably, the Cryogenian Period (ca. 720–635 Ma) witnessed two episodes

46 of global-scale low-latitude glaciation: the Sturtian glaciation (717–660 Ma) and the Marinoan glaciation  
47 (>639–635 Ma) (Hoffman et al., 1998; Rooney et al., 2015; Hoffman et al., 2017). These glaciations have  
48 been widely regarded as among the most profound ice ages in Earth's history. Sedimentological and  
49 paleomagnetic studies suggest that glaciers during the Cryogenian glaciations may have approached the  
50 equatorial latitudes, forming a "Snowball Earth" (Kirschvink, 1992; Hoffman et al., 1998; Hoffman and  
51 Schrag, 2002). Although the Neoproterozoic fossil record shows an Ediacaran (635–541 Ma) emergence  
52 of early animal life (Xiao et al., 2016), molecular clock studies suggest that the origin of the animal phyla  
53 may have occurred in early Neoproterozoic (Runnegar, 1982; Peterson et al., 2004). Therefore, a precise  
54 biogeochemical reconstruction of the Neoproterozoic Era is critical to understanding the environmental  
55 context of early animal life evolution.

56 A remarkable feature of the Neoproterozoic chemostratigraphy is the anomalously high pyrite  
57 sulfur isotope ( $\delta^{34}\text{S}_{\text{pyrite}}$ ) values, many of which are higher than the inferred contemporaneous seawater  
58  $\delta^{34}\text{S}_{\text{sulfate}}$  values (i.e.,  $\delta^{34}\text{S}_{\text{pyrite}} > \delta^{34}\text{S}_{\text{sulfate}}$ ) that are reconstructed from coexisting sulfate phases (e.g.,  
59 anhydrite, carbonate-associated sulfate) (Fig. 1; Appendix 1). These pyrites are commonly known as  
60 "superheavy pyrite" (Liu et al., 2006; Ries et al., 2009; Fike et al., 2015). The biogeochemical origin and  
61 palaeoenvironmental implications of the Neoproterozoic superheavy pyrite have puzzled geochemists for  
62 decades (Hayes et al., 1992; Fike et al., 2015). In marine sulfur cycles,  $\delta^{34}\text{S}_{\text{pyrite}}$  signals can never be  
63 higher than coexisting  $\delta^{34}\text{S}_{\text{sulfate}}$  signals (Canfield, 2001a; Böttcher, 2011; Canfield and Farquhar, 2012),  
64 therefore the occurrence of superheavy pyrite challenges the canonical understanding of the sulfur isotope  
65 systems.

66 Multiple studies have reported anomalously high  $\delta^{34}\text{S}$  values in the Cryogenian Period (Fig. 1;  
67 Appendix 1), including the Datangpo Formation in South China (Wu et al., 2016 and references therein),  
68 the Tapley Hill Formation in Australia (Hayes et al., 1992; Gorjan et al., 2000), the Court and Rasthof  
69 formations in Namibia (Hurtgen et al., 2002; Gorjan et al., 2003), the Bonahaven Dolomite Formation in  
70 Scotland (Parnell and Boyce, 2017), and the Arena Formation in East Greenland (Scheller et al., 2018).  
71 Notably, reported superheavy pyrites in these formations all overlie the Sturtian glacial diamictite, leading  
72 to the speculation of a potential linkage between the superheavy pyrite and the Sturtian glaciation (Gorjan  
73 et al., 2000; Hurtgen et al., 2002).

74 Largely based on the post-glacial occurrence of the superheavy pyrites, a tantalizing hypothesis  
75 links the genesis of superheavy pyrite to a Snowball Earth glaciation (Gorjan et al., 2000; Hurtgen et al.,  
76 2002). In this scenario, the ocean during the Sturtian glaciation was covered with a thick ice sheet,  
77 therefore terrestrial sulfate input by riverine fluxes was significantly reduced or shut off. Continuous  
78 pyrite burial via microbial sulfate reduction (MSR) in the subglacial ocean drove seawater  $\delta^{34}\text{S}_{\text{sulfate}}$  to  
79 extremely high values. During deglaciation, the high- $\delta^{34}\text{S}_{\text{sulfate}}$  water mass generated and maintained  
80 during the Snowball Earth upwelled onto continental shelf environments, causing the precipitation of  
81 superheavy pyrite in post-glacial successions at a global scale.

82 The above hypothesis is attractive in that it links the genesis of superheavy pyrites to the Sturtian  
83 glaciation. If correct, then extremely high seawater  $\delta^{34}\text{S}_{\text{sulfate}}$  values hypothesized in the terminal Sturtian  
84 oceans are expected to be reflected in syngenetic or early authigenic pyrite in diamictite intervals  
85 assuming a certain fractionation between  $\delta^{34}\text{S}_{\text{sulfate}}$  and  $\delta^{34}\text{S}_{\text{sulfide}}$ . Insofar as pyrite authigenesis could  
86 represent a broad spectrum of conditions from syndepositional to postdepositional, pyrites can be  
87 remarkably zoned or heterogeneous. Therefore, conventional >mm-scale  $\delta^{34}\text{S}_{\text{pyrite}}$  analysis of mineral  
88 concentrates extracted from bulk samples may be useful in constraining the  $\delta^{34}\text{S}_{\text{sulfate}}$  signals of  
89 contemporaneous seawater. To test this hypothesis, it is critical to target early authigenic pyrite in  
90 diamictite samples and analyze the  $\delta^{34}\text{S}_{\text{pyrite}}$  values in situ at micron-scale.

91 The focus of this study is the Cryogenian strata in South China (Fig. 2). Superheavy pyrite has  
92 been widely reported from the Cryogenian Datangpo Formation in South China with anomalously high

93  $\delta^{34}\text{S}_{\text{pyrite}}$  values up to ca. +70‰ (Liu et al., 2006; Li et al., 2012; Wu et al., 2016). The post-Sturtian  
94 seawater  $\delta^{34}\text{S}_{\text{sulfate}}$  value is estimated to be ca. +26‰ based on nodular and “chicken wire” anhydrite in  
95 Australia (Gorjan et al., 2000), or no more than ca. +50‰ based on carbonate-associated sulfate (CAS)  
96 analysis of the Cryogenian carbonates in Australia, Namibia (Hurtgen et al., 2005) and South China (Lang,  
97 2016). Based on these  $\delta^{34}\text{S}_{\text{sulfate}}$  constraints, many of the published  $\delta^{34}\text{S}_{\text{pyrite}}$  values from the Cryogenian  
98 Datangpo Formation are much higher than the inferred coeval seawater  $\delta^{34}\text{S}_{\text{sulfate}}$  values (Fig. 1; Appendix  
99 1).

## 100 INTERROGATING THE SUPERHEAVY PYRITE

101 To understand the origin of the superheavy pyrite, two outstanding questions should be addressed.  
102 First, how to create and maintain a high- $\delta^{34}\text{S}_{\text{sulfate}}$  reservoir? Based on current knowledge of sulfur isotope  
103 systems, to generate high- $\delta^{34}\text{S}_{\text{pyrite}}$  values requires a sulfate reservoir with even higher  $\delta^{34}\text{S}_{\text{sulfate}}$ . Therefore,  
104 the existence of a sulfate reservoir with extremely high- $\delta^{34}\text{S}_{\text{sulfate}}$  has been invoked in multiple models.  
105 Models for such high- $\delta^{34}\text{S}_{\text{sulfate}}$  reservoirs show a wide spectrum of geological settings: an ice-covered  
106 ocean during a hard snowball-Earth glaciation (Gorjan et al., 2000; Walter et al., 2000; Gorjan et al., 2003;  
107 Parnell and Boyce, 2017), a restricted basin with limited access to the open ocean (Li et al., 2012), an  
108 isolated porewater system (Chen et al., 2008), a sulfate minimum zone in the water column (Logan et al.,  
109 1995), a stratified ocean with substantial burial of pyrite in the euxinic deep ocean (Logan et al., 1995;  
110 Canfield, 2004), or a local euxinic water mass with active emissions of low- $\delta^{34}\text{S}_{\text{org}}$  organic sulfur (Lang,  
111 2016; Lang et al., 2016).

112 Second, how to reverse sulfur isotope fractionations ( $\Delta^{34}\text{S}_{\text{sulfate-sulfide}}$ ) to negative values? During  
113 microbial sulfate reduction (MSR),  $\delta^{34}\text{S}_{\text{pyrite}}$  can approach, but not be higher than, the coexisting  $\delta^{34}\text{S}_{\text{sulfate}}$   
114 signals. Therefore, to produce reversed  $\Delta^{34}\text{S}_{\text{sulfate-sulfide}}$  values, the sulfur reservoirs of  $\delta^{34}\text{S}_{\text{sulfate}}$  and  
115  $\delta^{34}\text{S}_{\text{sulfide}}$ , respectively, have to be decoupled. In other words, two coexisting, but separated, sulfur  
116 reservoirs are needed to explain the reversed values of  $\Delta^{34}\text{S}_{\text{sulfate-sulfide}}$ . Such conditions are uncommon in  
117 marine environments.

118 Implicit among most of the published models is the notion that the superheavy pyrite formed via  
119 MSR. However, this assumption has not been tested. To test this assumption and reevaluate published  
120 models, an integrated approach that combines both basin-scale field observation and  $\mu\text{m}$ -scale SIMS  
121  $\delta^{34}\text{S}_{\text{pyrite}}$  analysis coupled to SEM-based petrography is required. For example, pyrite formed in seawater  
122 (i.e., open system) vs. in pore waters (i.e., restricted system) could result in different patterns of  $\delta^{34}\text{S}_{\text{pyrite}}$   
123 at  $\mu\text{m}$  scale when Rayleigh fractionation occurs. Higher  $\delta^{34}\text{S}_{\text{pyrite}}$  values are expected to be strongly zoned  
124 in late-stage overgrowths of pyrite if it forms in an increasingly fractionated pore-water system. In  
125 contrast, pyrite formed in the marine water column should record relatively low  $\delta^{34}\text{S}_{\text{pyrite}}$  values without  
126 strong heterogeneity in  $\delta^{34}\text{S}_{\text{pyrite}}$  at  $\mu\text{m}$  scale. In addition, pyrite formed during early syndepositional  
127 diagenesis vs. late burial diagenesis could also be reflected in paragenesis, and revealed by petrography.

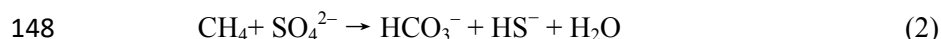
128 In this study, we aim to test published models for the genesis of Neoproterozoic superheavy  
129 pyrite in South China using the novel SEM-SIMS approach. Detailed petrographic observations by  
130 scanning electron microscopy (SEM) and in situ  $\mu\text{m}$ -scale  $\delta^{34}\text{S}_{\text{pyrite}}$  analysis by secondary ion mass  
131 spectrometry (SIMS) were performed for the pyrite samples. The SIMS  $\delta^{34}\text{S}_{\text{pyrite}}$  analyses are coupled  
132 with detailed petrographic observations by scanning electron microscopy (SEM) and trace elements by  
133 electron-probe microanalysis (EPMA). Based on these new results, a  $\delta^{34}\text{S}_{\text{sulfide}}$  constraint that is directly  
134 based on early authigenic pyrites for the Sturtian glacial ocean was achieved for the first time. These data  
135 evaluate if the seawater  $\delta^{34}\text{S}_{\text{sulfide}}$  signal during the terminal Sturtian glaciation was as heavy as inferred by  
136 previous studies (Gorjan et al., 2000; Hurtgen et al., 2002). Alternatively, we will test if superheavy pyrite  
137 formed via thermochemical sulfate reduction (TSR) during a post-depositional hydrothermal event. This  
138 is in strong contrast with the widely accepted assumption, held for decades, of a microbial sulfate  
139 reduction (MSR) origin for the Neoproterozoic superheavy pyrite in South China.

## 140 BACKGROUND

141 Current interpretations of the deep-time  $\delta^{34}\text{S}$  records apply fractionations of sulfur isotopes  
142 between sulfate and sulfide ( $\Delta^{34}\text{S}_{\text{sulfate-sulfide}} = \delta^{34}\text{S}_{\text{sulfate}} - \delta^{34}\text{S}_{\text{sulfide}}$ ). Before fully investigating the  
143 Neoproterozoic superheavy pyrite, a brief review of sulfur isotopes is necessary.

### 144 Microbial sulfate reduction (MSR)

145 Microbial sulfate reduction is the dominant mechanism that fractionates sulfur isotopes in marine  
146 environments. It is often expressed as the following simplified reactions:



149 Most MSR occurs at temperatures lower than  $\sim 100^\circ\text{C}$  (Jørgensen et al., 1992). During MSR,  
150 sulfate-reducing bacteria reduce sulfate to sulfide and form pyrite with  $\delta^{34}\text{S}$  values lower than the  
151 coexisting sulfate (i.e.,  $\delta^{34}\text{S}_{\text{sulfide}} < \delta^{34}\text{S}_{\text{sulfate}}$ ) (Kaplan and Rafter, 1958; Kaplan and Rittenberg, 1964;  
152 Canfield, 2001a; Böttcher, 2011). MSR-induced sulfur isotope fractionation  $\Delta^{34}\text{S}_{\text{sulfate-sulfide}}$  up to +40‰  
153 has been produced in lab experiments (Canfield, 2001b). More recently, experiments with pure cultures of  
154 sulfate reducers show a maximal  $\Delta^{34}\text{S}_{\text{sulfate-sulfide}}$  of +66‰ at sulfate concentrations ( $[\text{SO}_4^{2-}]$ ) similar to  
155 modern seawater at 28 mM (Sim et al., 2011a). Even larger  $\Delta^{34}\text{S}_{\text{sulfate-sulfide}}$  values of up to +72‰ have  
156 been found in natural samples (Wortmann et al., 2001; Canfield et al., 2010; Sim et al., 2011a).

157 Sulfate concentrations ( $[\text{SO}_4^{2-}]$ ) in solutions can strongly influence the magnitude of  $\Delta^{34}\text{S}_{\text{sulfate-}}$   
158  $\text{sulfide}$ . Experimental studies of microbial cultures demonstrate that the degree of MSR-induced sulfur  
159 isotope fractionation in both seawater and freshwater can be increasingly suppressed as  $[\text{SO}_4^{2-}]$  decreases,  
160 and  $\Delta^{34}\text{S}_{\text{sulfate-sulfide}}$  approaches zero when  $[\text{SO}_4^{2-}]$  is less than 200  $\mu\text{M}$  (Habicht et al., 2002). However, a  
161 more recent study based on Lake Matano (Indonesia) suggests large fractionations ( $>20\%$ ) at sulfate  
162 levels below 200  $\mu\text{M}$  (Crowe et al., 2014).

163 In addition, environmentally controlled experiments suggest that the magnitude of MSR-induced  
164 sulfur isotope fractionation is also related to strain-specific factors (Fike et al., 2015; Bradley et al., 2016),  
165 intracellular metabolite levels (Wing and Halevy, 2014), and sulfate reduction rate that is dependent on  
166 the availability of organic substrates as electron donors (Canfield et al., 2010; Leavitt et al., 2013; Leavitt,  
167 2014; Fike et al., 2015; Gomes and Hurtgen, 2015). The magnitude of  $\Delta^{34}\text{S}_{\text{sulfate-sulfide}}$  is found to be  
168 inversely proportional to the cell-specific sulfate reduction rate (csSRR) (Harrison and Thode, 1958;  
169 Kaplan and Rittenberg, 1964; Chambers et al., 1975; Sim et al., 2011a; Sim et al., 2011b; Sim et al., 2012;  
170 Leavitt et al., 2013; Fike et al., 2015). This inverse relationship between  $\Delta^{34}\text{S}_{\text{sulfate-sulfide}}$  and csSRR is  
171 consistent with observations in modern marine sediments, particularly in the sulfate–methane transition  
172 zone (SMTZ) where MSR rate reaches a maximum in the presence of an upward methane flux and a  
173 downward sulfate flux (Jørgensen et al., 2004; Lin et al., 2016b). Additionally, sedimentation rate could  
174 also play a role in controlling the expression of  $\Delta^{34}\text{S}_{\text{sulfate-sulfide}}$ . Studies suggest that higher sedimentation  
175 rate could cause smaller  $\Delta^{34}\text{S}_{\text{sulfate-sulfide}}$  and higher  $\delta^{34}\text{S}_{\text{pyrite}}$  values, and conversely, lower sedimentation  
176 rate could cause larger  $\Delta^{34}\text{S}_{\text{sulfate-sulfide}}$  and lower  $\delta^{34}\text{S}_{\text{pyrite}}$  values (Goldhaber and Kaplan, 1975; Claypool,  
177 2004; Pasquier et al., 2017).

178 In marine environments, bacterial sulfur disproportionation (BSD) could also play a significant  
179 role in fractionating the sulfur isotopes. During BSD, sulfides produced through MSR are re-oxidized to  
180 elemental sulfur, and then subsequently disproportionated to sulfate and sulfide, by coupling with the  
181 reduction of  $\text{O}_2$ ,  $\text{NO}_3^-$ , iron or manganese compounds (Canfield and Thamdrup, 1994; Canfield and Teske,  
182 1996; Canfield, 2001a; Fike et al., 2015). Disproportionation reactions can significantly augment the

183 fractionation of sulfur isotopes, resulting in isotopic contrasts between reactant sulfate and product sulfide  
184 with  $\Delta^{34}\text{S}_{\text{sulfate-sulfide}}$  greater than +70‰. The involvement of BSD has been proposed to occur in the rock  
185 record of multiple geological intervals (Canfield and Teske, 1996; Johnston et al., 2005; Fike et al., 2006;  
186 Wu et al., 2015b; Cui et al., 2016b; Kunzmann et al., 2017).

187 Published studies of MSR-derived pyrite in sedimentary rocks typically show strong  
188 heterogeneity in  $\delta^{34}\text{S}_{\text{pyrite}}$  values at  $\mu\text{m}$  scales (Machel et al., 1997; Kohn et al., 1998; Machel, 2001;  
189 Wacey et al., 2010; Williford et al., 2011; Lin et al., 2016b; Meyer et al., 2017; Peng et al., 2017; Gomes  
190 et al., 2018; Marin-Carbonne et al., 2018). This is largely due to a biogenic nature of MSR and the  
191 involvement of Rayleigh fractionation in restricted pore waters (Kohn et al., 1998; McLoughlin et al.,  
192 2012; Wacey et al., 2015). As MSR proceeds in pore water environments, the restricted flow of  
193 porewaters and Rayleigh fractionation causes progressively lower  $\Delta^{34}\text{S}_{\text{sulfate-sulfide}}$ , higher  $\delta^{34}\text{S}_{\text{sulfate}}$ , and  
194 consequently higher  $\delta^{34}\text{S}_{\text{sulfide}}$  values (Kaplan and Rafter, 1958; Kaplan and Rittenberg, 1964; Canfield,  
195 2001a).

196 Rayleigh fractionation of sulfur isotopes can be expressed at both stratigraphic meter-to-  
197 kilometer- and micrometer-scales. (1) Stratigraphically,  $\delta^{34}\text{S}$  values of both porewater sulfate and  
198 authigenic pyrite typically increase with greater burial depth (Goldhaber and Kaplan, 1980; Borowski et  
199 al., 2000; Canfield, 2001a; Fike et al., 2015); (2) At micrometer scales, as pyrite grains continuously grow  
200 during diagenesis, the late-stage pyrite overgrowth typically records higher  $\delta^{34}\text{S}_{\text{pyrite}}$  values than the early-  
201 stage pyrite (e.g., Raiswell, 1982; McKibben and Riciputi, 1998; Ferrini et al., 2010; Williford et al., 2011;  
202 Fischer et al., 2014; Drake et al., 2015; Lin et al., 2016b; Drake et al., 2017). Both phenomena reflect the  
203 occurrence of Rayleigh fractionation in the broad spectrum of post-depositional process. Therefore, strong  
204 heterogeneity in  $\delta^{34}\text{S}_{\text{pyrite}}$  is predicted to be common in MSR-dominated environments.

205 Taken together, MSR could cause significant fractionation between sulfate and sulfide. The  
206 controlling factors of  $\Delta^{34}\text{S}_{\text{sulfate-sulfide}}$  in marine environments are non-unique. Multiple factors may play a  
207 role, including sulfate concentration, MSR rate, organic carbon availability, and sulfide re-oxidation.  
208 Rayleigh fractionation of sulfur isotopes in restricted pore waters could cause strong  $\delta^{34}\text{S}$  heterogeneity at  
209 both stratigraphic and mineral scales.

## 210 Thermochemical sulfate reduction (TSR)

211 Thermochemical sulfate reduction is an abiotic process by which sulfate is reduced by organic  
212 matter during heating. The temperatures of TSR are typically higher than 110 °C (Goldstein and  
213 Aizenshtat, 1994; Machel et al., 1995; Worden et al., 1995; Machel, 2001; Jiang et al., 2015). The  
214 reactants and products of TSR and MSR can be very similar, therefore distinguishing these two sulfate-  
215 reduction pathways is not straightforward and often requires multiple lines of evidence (Machel et al.,  
216 1995; Machel, 2001).

217 The  $\Delta^{34}\text{S}_{\text{sulfate-sulfide}}$  induced by TSR remains poorly constrained compared with that of the MSR.  
218 Lab experiments show that the TSR rate is strongly dependent on temperatures (Kiyosu, 1980; Kiyosu  
219 and Krouse, 1990). The TSR-induced values of  $\Delta^{34}\text{S}_{\text{sulfate-sulfide}}$  caused by hydrocarbons at  $T > 200^\circ\text{C}$  are  
220 typically around 25‰ (Ohmoto and Goldhaber, 1997). However, disequilibrium  $\Delta^{34}\text{S}_{\text{sulfate-sulfide}}$  values  
221 ranging from +20.8‰ to -5.0‰ have also been reported in TSR experiments using amino acids  
222 (Watanabe et al., 2009). Published lab experiments suggest that the  $\Delta^{34}\text{S}_{\text{sulfate-sulfide}}$  value at equilibrium is  
223 ~40‰ (Friedman and O'Neil, 1977) or ~30‰ (Ohmoto and Lasaga, 1982; Ohmoto, 1986; Ohmoto and  
224 Goldhaber, 1997; Seal, 2006) at the temperature of ~200 °C.

225 The occurrence of TSR has been widely reported in hydrocarbon reservoirs (Orr, 1974; Orr, 1977;  
226 Machel, 1987; Heydari and Moore, 1989; Worden et al., 1995; Riciputi et al., 1996; Worden and Smalley,  
227 1996; Worden et al., 2000; Cai et al., 2001; Cai et al., 2003; Cai et al., 2004; Zhu et al., 2007a; Zhu et al.,

228 2007b; Hao et al., 2008; Machel and Buschkuehle, 2008; Jiang et al., 2014; King et al., 2014; Cai et al.,  
229 2015; Jia et al., 2015; Jiang et al., 2015; Zhu et al., 2015; Biehl et al., 2016; Fu et al., 2016; Liu et al.,  
230 2016; Olanipekun and Azmy, 2018). It was revealed that TSR can play a significant role in enhancing the  
231 secondary porosity and permeability of carbonate reservoirs (Jiang et al., 2018).

232 TSR has also been invoked as an important process in ore deposits (Rye and Ohmoto, 1974;  
233 Powell and Macqueen, 1984; Ghazban et al., 1990; Tompkins et al., 1994; Randell and Anderson, 1996;  
234 Alonso et al., 1999; Cooke et al., 2000; Peevler et al., 2003; Kelley et al., 2004a; Kelley et al., 2004b;  
235 Basuki et al., 2008; Gadd et al., 2017; Sośnicka and Lüders, 2018). Hydrothermal sulfate-bearing fluids  
236 that percolated through preexisting evaporites could react with organic matter and form pyrite deposits.

237 TSR could also be critical in interpreting the sulfur isotope records of the early Earth. It has been  
238 found that TSR could produce anomalous mass-independent fractionation (MIF) signals of sulfur isotopes  
239 ( $\Delta^{33}\text{S} = +0.1$  to  $+2.1\text{‰}$  and  $\Delta^{36}\text{S} = -1.1$  to  $+1.1\text{‰}$ ) by using specific amino acids (Watanabe et al., 2009;  
240 Oduro et al., 2011), which may have been largely overlooked in the study of the early Earth (Watanabe et  
241 al., 2009; Ohmoto et al., 2014). In a more recent study,  $\delta^{34}\text{S}_{\text{pyrite}}$  signals up to  $+90\text{‰}$  have been found in  
242 the early Paleoproterozoic succession (2.415 Ga) in South Africa, which have been interpreted as  
243 resulting from late fluids during burial metamorphism and late diagenesis (Johnson et al., 2013).

244 In summary, the occurrence of TSR has been widely reported from hydrocarbon reservoirs and  
245 ore deposits. TSR has also been invoked in the study of sulfur isotope signals of the deep-time records.  
246 The TSR-induced  $\Delta^{34}\text{S}_{\text{sulfate-sulfide}}$  is relatively less constrained than that of the MSR, but  $\Delta^{34}\text{S}_{\text{sulfate-sulfide}}$  are  
247 dependent on temperatures with smaller fractionations in higher temperatures.

## 248 GEOLOGICAL SETTINGS

### 249 Stratigraphy and paleogeography

250 The focus of this study is the Cryogenian Tiesi'ao and Datangpo formations in South China (Fig.  
251 2A–C). The Tiesi'ao and Datangpo formations have been widely regarded as a glacial-postglacial  
252 transition in South China. The Tiesi'ao Formation is a glacial diamictite interval of the Sturtian glaciation.  
253 The overlying Datangpo Formation is typically subdivided into three members by local mining companies,  
254 which are, in ascending order, Member 1 black shale with basal Mn-rich carbonate intervals, Member 2  
255 gray shale, and Member 3 siltstone (Fig. 2C) (Xu et al., 1990; Zhou et al., 2004; Qin et al., 2013; Zhu et  
256 al., 2013; Xie et al., 2014; Wu et al., 2016). The Mn-rich carbonate interval in the basal Datangpo  
257 Formation has been proposed to be the Sturtian "cap carbonate" (Yu et al., 2017) and is the main target for  
258 Mn mining in South China (Wu et al., 2016).

259 Paleogeographic reconstructions in previous studies reveal that a southeast facing (present  
260 direction) passive margin on the Yangtze block was developed during the breakup of the Rodinia  
261 supercontinent (Fig. 2A, B) (Jiang et al., 2003; Wang and Li, 2003; Hoffman and Li, 2009; Li et al.,  
262 2013). Therefore a rift basin was formed in South China during the Cryogenian Period (Fig. 2C). The  
263 Datangpo Formation is mainly distributed in the slope and basinal facies (Xu et al., 1990; Xiao et al.,  
264 2014; Wu et al., 2016).

### 265 Age constraints

266 The ages of the Neoproterozoic strata in South China are relatively well constrained. Based on a  
267 TIMS U–Pb age of  $662.9 \pm 4.3$  Ma (Zhou et al., 2004) and a SIMS U–Pb age of  $667.3 \pm 9.9$  Ma (Yin et  
268 al., 2006) analyzed from zircons in the tuff beds within the Mn-rich carbonate interval of the basal  
269 Datangpo Formation (Fig. 2C), the Tiesi'ao diamictite and Mn-rich carbonate couplet is constrained to be  
270 of the Sturtian age (Zhou et al., 2004; Yin et al., 2006).

271 Stratigraphically upward, the Datangpo Formation is overlain by the Cryogenian Nantuo  
272 diamictite, and then the Ediacaran Doushantuo (635–551 Ma) and Dengying (551–541 Ma) formations. A  
273 SIMS U–Pb age of  $654.5 \pm 3.8$  Ma from an ash bed immediately below the Nantuo Formation provides a  
274 maximum age for the upper boundary of the Datangpo Formation (Zhang et al., 2008). Based on a TIMS  
275 U–Pb age of  $635.2 \pm 0.6$  Ma analyzed from a tuff bed within the cap dolostone right above the Nantuo  
276 diamictite, the Nantuo Formation is constrained to be a Marinoan counterpart (Condon et al., 2005). The  
277 ages from South China and other basins suggest that the Cryogenian glaciations are synchronous at a  
278 global scale (Calver et al., 2013; Lan et al., 2015a; Lan et al., 2015b; Rooney et al., 2015; Song et al.,  
279 2017).

## 280 **Distribution of the superheavy pyrite**

281 Superheavy pyrites with bulk  $\delta^{34}\text{S}$  values up to ca. +70‰ have been reported in the postglacial  
282 Datangpo Formation (Fig. 1) (Wang et al., 1985; Tang, 1990; Li et al., 1996; Chu et al., 1998; Li et al.,  
283 1999a; Tang and Liu, 1999; Chu et al., 2001; Yang et al., 2002; Chu et al., 2003; Liu et al., 2006; Zhou et  
284 al., 2007; Chen et al., 2008; Feng et al., 2010; Li et al., 2012; Zhang et al., 2013; Zhu et al., 2013; Zhang,  
285 2014; Wu et al., 2015a; Wang et al., 2016; Wu et al., 2016). A comprehensive compilation of the  
286 distributions of the Datangpo superheavy pyrite at a basin scale reveals a close association with ancient  
287 faults (see Fig. 12 in Wu et al., 2016). Similarly, the Datangpo manganese deposits are also associated  
288 with ancient faults (Qin et al., 2013; Zhou et al., 2013). Field studies of the Datangpo Formation show  
289 abundant textures that suggest pervasive overprint by hydrothermal fluids triggered by tectonic events.  
290 These textures include faulting, host rock breccia, sharp-sided quartz veins, calcite, gypsum, and barite  
291 infillings and veins (Xu et al., 1990; Chen and Chen, 1992; He et al., 2013a; He et al., 2013b; Zhang et al.,  
292 2013; Pan et al., 2016).

## 293 **SAMPLES**

294 Most chemostratigraphic studies analyze  $\delta^{34}\text{S}_{\text{pyrite}}$  from mg-size aliquots of powder obtained  
295 at >mm-scale by crushing or drilling samples. These procedures homogenize samples that may be zoned  
296 or heterogeneous at  $\mu\text{m}$ -to-mm scale. In contrast, the SIMS analysis of this study sputtered 2- $\mu\text{m}$  diameter  
297 pits ( $\sim 1\text{-}\mu\text{m}$  deep) in situ from polished surfaces that had been imaged by SEM, representing samples over  
298 a million times smaller than in conventional analysis (<ng vs. >mg). By SIMS, it is only practical to  
299 examine a relatively small number of hand samples, but SEM examination makes it possible to select  
300 representative or critical regions and a large amount of data can be efficiently obtained at this scale. The  
301 information density per sample can be extraordinarily high by SIMS yielding information that is  
302 inaccessible by other means (Eldridge et al., 1989; Valley and Kita, 2009; Williford et al., 2016; Cui et al.,  
303 2018). Thus, the best-preserved, most-representative samples were selected for detailed analysis in this  
304 study.

305 The studied drill core (ZK1105, drilled in September 2015) is composed of the Cryogenian  
306 Tiesi'ao Formation and Datangpo Formation at the Daotuo mine ( $28^{\circ}07'04''\text{N}$ ,  $108^{\circ}52'26''\text{E}$ ), Songtao  
307 County, eastern Guizhou Province in South China (Fig. 2B). The Daotuo mine represents the largest  
308 known Mn ore reserve (up to 142 Mt in carbonates) in China (Qin et al., 2013; Zhu et al., 2013; Wu et al.,  
309 2016), and records bulk  $\delta^{34}\text{S}_{\text{pyrite}}$  values as high as ca. +70‰ (Fig. 1) (Zhu et al., 2013; Wu et al., 2016),  
310 providing a good opportunity for the study of superheavy pyrite and Mn metallogenesis.

311 Four samples were selected from the ZK1105 drill core for detailed SEM-SIMS  $\delta^{34}\text{S}_{\text{pyrite}}$  study  
312 (Figs. 2C, 3, 4). **Sample 1** (drill core Hy59) is a diamictite specimen from the uppermost Tiesi'ao  
313 Formation. **Sample 2** (drill core Hy55) is a Mn-rich carbonate specimen from the lower Member 1 of the  
314 Datangpo Formation. **Sample 3** (drill core Hy31) is black shale from the upper Member 1 of the Datangpo  
315 Formation. **Sample 4** (drill core Hy1) is from lower Member 2 of the Datangpo Formation. These four  
316 samples cover the main lithologies (diamictite, Mn-rich carbonates, and shale) and pyrite morphology

317 (including pyrite framboids, pyrite overgrowth, and euhedral to subhedral pyrite grains, respectively) (Fig.  
318 4). Individual pyrite grains were imaged by SEM with back-scattered electrons (BSE) and secondary  
319 electrons (SE) prior to SIMS analysis. Mineral chemistry was verified by SEM energy-dispersive  
320 spectrometry (EDS) and electron-probe microanalysis (EPMA).

## 321 METHODS

### 322 SIMS analysis

323 Samples in this study were analyzed by a CAMECA IMS 1280 at the WiscSIMS (Wisconsin  
324 Secondary Ion Mass Spectrometry) Lab, Department of Geoscience, University of Wisconsin–Madison.  
325 The analyses include three SIMS sessions. During session 1 (Oct. 18-19, 2018) and session 3 (June 8,  
326 2017), sulfur two-isotopes ( $^{32}\text{S}$ ,  $^{34}\text{S}$ ) were measured with a 2- $\mu\text{m}$ -diameter beam size. During session 2  
327 (May 22, 2017), sulfur three isotopes ( $^{32}\text{S}$ ,  $^{33}\text{S}$ ,  $^{34}\text{S}$ ) were measured with a 10- $\mu\text{m}$ -diameter beam size.

328 The UWPy-1 standard (pyrite from the Balmat Mine, NY,  $\delta^{34}\text{S} = 16.04 \pm 0.18\%$ ,  $\Delta^{33}\text{S} = -0.003$   
329  $\pm 0.009\%$ , 2SD, V-CDT) (Ushikubo et al., 2014) was used to calibrate analyses of pyrite. Sulfur isotope  
330 ratios are reported in standard per mil (‰) notation relative to V-CDT, calculated as  $\delta^{34}\text{S}_{\text{unknown}} =$   
331  $[(^{34}\text{S}/^{32}\text{S})_{\text{unknown}} / (^{34}\text{S}/^{32}\text{S})_{\text{VCDT}} - 1] \times 1000$ . Measured ratios of  $^{34}\text{S}/^{32}\text{S}$ , were divided by the V-CDT value  
332 of  $^{34}\text{S}/^{32}\text{S} = 1/22.6436$  (Ding et al., 2001), and were calculated as “raw”  $\delta$ -values  $\delta^{34}\text{S}_{\text{raw}}$  before converting  
333 to the V-CDT scale based on eight analyses of UWPy-1 that bracket each group of 10-15 sample analyses.  
334 All the data can be found in the online appendices ([Appendices 2–6](#)).

335 **SIMS sessions 1 and 3 ( $^{32}\text{S}$ ,  $^{34}\text{S}$  analysis; 2- $\mu\text{m}$  beam size).** Measurements of  $^{34}\text{S}/^{32}\text{S}$  were made  
336 using a  $^{133}\text{Cs}^+$  primary ion beam with an intensity of  $\sim 30$  pA in session 3, which was focused to  
337 approximately  $2 \times 1$   $\mu\text{m}$  at the surface of the sample. The secondary  $^{32}\text{S}^-$ ,  $^{34}\text{S}^-$  and  $^{32}\text{S}^1\text{H}^-$  ions were  
338 simultaneously collected by detectors L'2, FC2, and C, respectively, using three Faraday cups. The  
339 secondary ion intensity of  $^{32}\text{S}^-$  was  $\sim 6 \times 10^7$  cps and  $\sim 2.2 \times 10^7$  cps for in session 1 and session 3,  
340 respectively.  $^{32}\text{S}^1\text{H}^-$  was analyzed to evaluate the effect of hydrogen that might be in the form of organic  
341 matter on the SIMS results. An electron flood gun in combination with a gold coat ( $\sim 40$  nm) was used for  
342 charge compensation. The total analytical time per spot was about 4 minutes including presputtering (60  
343 s), automatic centering of the secondary ion beam in the field aperture (90 s), and analysis (80 s). The  
344 baseline noise level of the Faraday cups was monitored during presputtering. The spot to spot precision of  
345  $\delta^{34}\text{S}_{\text{raw}}$  values based on all bracketing analyses of 2- $\mu\text{m}$  spots on standard UWPy-1 is  $\pm 0.91\%$  and  
346  $\pm 0.87\%$ , respectively, in session 1 and session 3 (2SD, [Appendix 7](#)).

347 **SIMS session 2 ( $^{32}\text{S}$ ,  $^{33}\text{S}$ ,  $^{34}\text{S}$  analysis; 10- $\mu\text{m}$  beam size).** During session 2, the secondary ion  
348 intensity was  $\sim 1.4 \times 10^9$  cps for  $^{32}\text{S}^-$  and  $\sim 1.7 \times 10^6$  cps for  $^{33}\text{S}^-$ . The ions  $^{32}\text{S}$ ,  $^{33}\text{S}$ ,  $^{34}\text{S}$  were simultaneously  
349 analyzed by detector L'2, C, FC2, respectively, using three Faraday cups. Mass resolving power ( $M/\Delta M$ ,  
350 measured at 10% peak height) was set to  $\sim 5000$ . Analysis time consisted of 30 s for presputtering, 80 s  
351 for centering of secondary ions in the field aperture, and 80 s for analysis.  $^{32}\text{S}^1\text{H}^-$  was analyzed by  
352 detector C at the end of each spot analysis. The ratio of the  $^{32}\text{S}^1\text{H}^-$  tail at the  $^{33}\text{S}^-$  peak position relative to  
353 the  $^{32}\text{S}^1\text{H}^-$  peak ( $^{32}\text{S}^1\text{H}_{\text{tail}}/^{32}\text{S}^1\text{H}_{\text{peak}}$ ) was determined ( $6.95\text{E}-6$ ) at the beginning of the session, which was  
354 used to correct the contribution of the  $^{32}\text{S}^1\text{H}^-$  tail signal to the  $^{33}\text{S}^-$  peak during each spot analysis.  $^{32}\text{S}^1\text{H}^-$   
355 was measured by using a deflector (DSP2X, which is located after the magnet) and detector C at end of  
356 each analysis. The contribution of  $^{32}\text{S}^1\text{H}^-$  to the  $^{33}\text{S}^-$  peak in all the spots ( $9.7 \times 10^{-4}\%$  at most,  $6.6 \times 10^{-$   
357  $4\%$  on average) is negligible. The  $\Delta^{33}\text{S}$  values were calculated as  $\Delta^{33}\text{S}_{\text{unknown}} = \delta^{33}\text{S}_{\text{unknown}} - 10^3 \times [(1 +$   
358  $\delta^{34}\text{S}_{\text{unknown}}/10^3)^{0.515} - 1]$ . The spot to spot precision of  $\delta^{34}\text{S}$  and  $\Delta^{33}\text{S}$  (values based on all bracketing  
359 analyses of 10- $\mu\text{m}$  spots on standard UWPy-1) is  $\pm 0.18\%$  and  $\pm 0.06\%$ , respectively (2SD, [Appendix 7](#)).

## 360 **Gold-coat removal and SEM imaging**

361 After SIMS analysis, gold coating was removed from samples by chemical dissolution of gold  
362 using a saturated solution of potassium iodide (Jones et al., 2012). The gold-removing solution is a 0.02  
363 mol/L solution of iodine in ethaline. Ethaline is prepared as a 1:2 molar mixture of choline chloride  
364 ( $C_5H_{14}ClNO$ ) and ethylene glycol ( $C_2H_6O_2$ ). The rinse solutions are potassium iodide solution and  
365 deionized water, respectively. The potassium iodide solution is prepared by adding potassium iodide (KI)  
366 to water until saturation. Samples were placed in the gold-removing solution on a hot plate at  $\sim 60$  °C for  
367 10 to 15 minutes, and then rinsed by potassium iodide saturated solution. The samples were rinsed again  
368 by deionized water before further analysis.

369 SEM imaging was performed in the Ray and Mary Wilcox Scanning Electron Microscopy  
370 Laboratory, Department of Geoscience, University of Wisconsin–Madison. BSE images of carbon-coated  
371 samples were acquired with a Hitachi S3400 VP SEM with EDS using a Thermo Fisher thin window  
372 detector. Each pit was investigated by SEM for possible irregularities. SEM images were acquired using  
373 an accelerating voltage of 15 keV or 20 keV at a working distance of 10 mm. All the SIMS pits were  
374 imaged by SEM and are shown with corresponding  $\delta^{34}S_{\text{pyrite}}$  values in the online appendices ([Appendices](#)  
375 [2–5](#)).

## 376 **EPMA analysis**

377 EPMA analysis was conducted in the Eugene Cameron Electron Microbeam Lab, Department of  
378 Geoscience, University of Wisconsin–Madison. EPMA was performed with the CAMECA SXFive field  
379 emission electron probe, operated at 20 kV and 50 nA, and either a focused beam or a 3-4 micron  
380 defocused beam, using wavelength dispersive crystal spectrometers ([Appendix 8](#)). Counting times were  
381 10 seconds on peak, and a total of 10 on backgrounds, for all elements except those noted in the following  
382 listing. Al Ka (20 sec) and Si Ka (20 sec) were acquired on a large TAP crystal; As Ka (20 sec) and Se Ka  
383 (20 sec) on LIF; S Ka and Ca Ka (27 sec) on large PET; Fe Ka, Mn Ka and Co Ka on LIF; and Ni Ka, Cu  
384 Ka and Zn Ka on large LIF. Standards used were Balmat pyrite (Fe, S), NBS glass K412 (Si, Al, Ca),  
385 arsenopyrite (As) and freshly polished metals for the balance. PHA modes used were integral, except for  
386 Al and Si which were differential mode. Software used was Probe for EPMA (Donovan et al., 2018). Off  
387 peak backgrounds were acquired, and matrix correction was conducted by using the Armstrong/Love  
388 Scott algorithm (Armstrong, 1988). Minimum detection levels are shown in [Appendix 8](#).

## 389 **RESULTS**

390 All the SIMS results in this study are shown with petrographic context in online [Appendices 2–5](#)  
391 and tabulated in online [Appendix 7](#). SIMS analyses of each spot that were off the correct target, with large  
392 internal error ( $2SE > 2\%$ ), or with yield values ( $^{32}S$  count rate divided by primary beam intensity,  
393 Mcps/pA) that are beyond the range from 90 to 110% of the mean yield values for UWPY-1 are  
394 considered unreliable. A total of 258 SIMS analyses (6 data points are unreliable) were made during  
395 session 1, including 182 analyses of unknown samples and 76 analyses of the UWPY-1 standard. A total  
396 of 18 SIMS analyses (0 data filtered) were made during session 2, including 10 analyses of unknown  
397 samples and 8 analyses of the UWPY-1 standard. A total of 138 analyses (10 data filtered) were made  
398 during session 3, including 87 analyses of the unknown samples and 41 analyses of the UWPY-1 standard.

399 Integrated SEM–SIMS results of the studied samples show distinct patterns in pyrite paragenesis,  
400 S isotope ratios and spatial distributions at  $\mu\text{m}$  scale ([Table 1](#); [Figs. 4–23](#); [Appendices 2–5](#)). These results  
401 are described below.

402 **Sample 1 (Hy59, glacial diamictite)**

403 **SEM petrography.** The pyrite phases in **Sample 1** typically show two types of texture: pyrite  
404 framboids (up to 30  $\mu\text{m}$  in diameter) (Figs. 4F, 4G, 5–7; Appendix 2) and pyrite nodules (Fig. 4H, 4I, 8;  
405 Appendix 2). (1) The pyrite framboids are mostly assemblages of smaller pyrite microcrystals (Figs. 4F,  
406 4G, 5–7). Sometimes, pyrite microcrystals may also occur outside the pyrite framboids as individual  
407 microcrystals surrounded by pyrite cement (Figs. 4G, 7A). BSE investigations at high magnification  
408 reveal that individual pyrite microcrystals are typically defined by a darker (lower average atomic number)  
409 rim (Fig. 5; Appendix 2). The shape and size of the pyrite microcrystals are similar within individual  
410 framboids, but may vary among different framboids. Octahedral, subhedral, and rounded pyrite  
411 microcrystals have all been observed within different pyrite framboids (Fig. 5; Appendix 2). (2) The  
412 pyrite nodules are mostly at mm scale, and consist of multiple zoned pyrite crystals at  $\mu\text{m}$  scales (Fig. 4H,  
413 4I, 8; Appendix 2).

414 **SIMS results.** A total of 90 spots were analyzed by SIMS in different textures, including  
415 framboidal pyrite ( $n = 76$ ), pyrite cements outside framboids ( $n = 4$ ), and pyrite nodules ( $n = 10$ )  
416 (Appendix 2). The  $\delta^{34}\text{S}$  values measured from pyrite nodules range from +9.8‰ to +52.2‰. The  $\delta^{34}\text{S}$   
417 values measured from pyrite framboids range from +11.2‰ to +28.3‰. Pyrite cements outside the  
418 framboids show  $\delta^{34}\text{S}$  ranging from +22.7‰ to +36.7‰ (Table 1; Figs. 22, 23). Generally, the pyrite  
419 cements outside the framboids (+30.9‰ in average) have much higher  $\delta^{34}\text{S}$  values than was measured  
420 within pyrite framboids (+16.4‰ on average) (Figs. 7A, 22, 23).

421 **Data evaluation.** SEM investigation of **Sample 1** shows that both the framboidal pyrite and the  
422 pyrite nodules are very heterogeneous at  $\mu\text{m}$  scale (Figs. 4F–I, 5–8; Appendix 2). The SIMS spots within  
423 the framboids may have covered both pyrite microcrystals that are smaller than the 2- $\mu\text{m}$  beam spot and  
424 pyrite cements between the microcrystals (Fig. 5). Similarly, closer views of the pyrite crystals within  
425 nodules show zoned pyrite overgrowths (Fig. 4I; 8C–J; Appendix 2). Therefore, the measured  $\delta^{34}\text{S}$  data  
426 from SIMS spots that include multiple phases should represent an averaged value of pyrite formed in  
427 different phases.

428 **Sample 2 (Hy55, Mn-rich carbonates)**

429 **SEM petrography.** **Sample 2** is mainly composed of laminated Mn-rich carbonate layers and  
430 siliciclastic-rich layers (Figs. 9–14). The Mn-rich carbonate layers are mostly granular rhodochrosite  
431 [ $\text{MnCO}_3$ ] (Fig. 10) and often show nodule- or sausage-shaped textures (Figs. 9, 12; Appendix 3). Trace  
432 amounts of euhedral kutnohorite [ $\text{CaMn}(\text{CO}_3)_2$ ] were also found. Lath-shaped illite crystals are abundant  
433 in **Sample 2** (Figs. 12, 13; Appendix 3). The pyrite in **Sample 2** shows intermittent sausage-shaped  
434 textures (Fig. 9A–F) that occur within the Mn-rich carbonate layers and preferentially replace the pre-  
435 existing carbonates (Figs. 9–13; Appendix 3). The nodule- or sausage-shaped texture of pyrite is largely  
436 inherited from that of the hosting Mn-rich carbonates (Appendix 3).

437 Under BSE (typically with decreased color brightness), pyrite in **Sample 2** shows at least two  
438 textures: individual pyrite framboids and lacy pyrite overgrowth/cements (Figs. 11, 13, 14). In contrast  
439 with the framboidal pyrite in **Sample 1** that shows a wide range in size (up to 30  $\mu\text{m}$  in diameter), all the  
440 pyrite framboids in **Sample 2** are smaller than 7  $\mu\text{m}$  in diameter (Appendix 3).

441 The pyrite framboids and the lacy pyrite “veins” within an overgrowth are typically brighter  
442 (higher average atomic number) than the pyrite overgrowth under BSE (Figs. 11A, 11I, 13H, 13G, 13L,  
443 14; Appendix 3). The detailed causes of this zoning are still unclear, but preliminary EPMA shows that  
444 the darker pyrite overgrowths yield lower analytical totals than the brighter pyrite framboids and lacy  
445 pyrite veins (Appendix 8), suggesting that porosity or C/N-rich inclusions may have played a role in  
446 causing this effect.

447 **Paragenesis.** Detailed SEM investigation allows reconstruction of the paragenesis of different  
448 minerals in Sample 2. Multiple lines of evidence suggest that pyrite in this sample postdates  
449 rhodochrosite and illite. Supporting evidence includes: (1) petrographic overviews showing that pyrite  
450 grains in this sample are nodule- or sausage-shaped and preserved exclusively within rhodochrosite  
451 lamina (Fig. 9); (2) rhodochrosite granules with ring-shaped pyrite cements (Fig. 10); (3) pyrite with  
452 abundant inclusions of granular rhodochrosite (Fig. 11); (4) magnified views showing that pyrite in  
453 Sample 2, either individual pyrite framboids (Fig. 13A–D) or framboidal pyrite with lacy pyrite  
454 overgrowths (Fig. 13E–L), are replacing both rhodochrosite and illite. More detailed petrographic  
455 evidence is available in the online Appendix 3. Taken together, these textures indicate that pyrite in this  
456 sample is relatively late, postdating the mineralization of rhodochrosite and illite.

457 **SIMS results.** Both disseminated pyrite framboids and lacy pyrite overgrowth have been  
458 analyzed for  $\delta^{34}\text{S}$  by SIMS. In total of 28 spots were analyzed in Sample 2 (Appendix 3). The range of  
459 SIMS  $\delta^{34}\text{S}$  values is from +56.3‰ to +60.4‰. These values are remarkably homogeneous regardless of  
460 heterogeneous textures under BSE (Figs. 14, 22, 23; Table 1).

### 461 Sample 3 (Hy31, black shale)

462 **SEM petrography.** In Sample 3, no framboidal pyrite was found. Instead, pyrite mostly shows  
463 disseminated subhedral grains ranging from 20 to 100  $\mu\text{m}$  in size (Figs. 15, 16; Appendix 4). It is notable  
464 that some pyrite grains are relatively large (up to 2 mm), composed of multiple  $\mu\text{m}$ -size pyrite sub-grains  
465 cemented by later-stage pyrite (Fig. 17; Appendix 4). The  $\mu\text{m}$ -size pyrite sub-grains mimic the  
466 disseminated pyrite in the shale matrix, suggesting that pyrite sub-grains were formed earlier, and were  
467 then cemented by pervasive pyrite cement.

468 **SIMS results.** A total of 108 spots were measured by SIMS from Sample 3 (Appendix 4),  
469 including both  $\mu\text{m}$ -size sub-grains ( $n = 85$ ; Fig. 16, 17) and mm-size pyrite cements ( $n = 23$ ; Fig. 17). The  
470 range of the SIMS  $\delta^{34}\text{S}$  values of individual pyrite sub-grains is from +60.3 to +71.2‰, with an average  
471 value of +66.3‰ (Figs. 16, 17, 22, 23). The pyrite cements show homogeneous  $\delta^{34}\text{S}$  values ranging from  
472 +60.2‰ to +64.8‰ (Figs. 17, 22, 23). Notably, the  $\mu\text{m}$ -scale SIMS  $\delta^{34}\text{S}$  analysis reveals a consistently  
473 decreasing  $\delta^{34}\text{S}$  trend from the core (ca. +70‰) to the edge (ca. +60‰) of individual pyrite grains (Figs.  
474 16, 17; Appendix 4).

### 475 Sample 4 (Hy1, shale)

476 **SEM petrography.** Two pyrite textures are found in Sample 4 (Fig. 18–21; Appendix 5). The  
477 first type of pyrite, named “pyrite flowers” here, is characterized by framboidal pyrite cores with a zoned  
478 pyrite overgrowth (Figs. 18C, 19). The second texture is characterized by “Fe-oxide coronas” with pyrite  
479 cores and thin pyrite rims (Figs. 18D, 20, 21). The pyrite cores inside the “Fe-oxide coronas” typically  
480 show framboidal textures in the center with fibrous textures in the outer surface (Figs. 18D, 20, 21),  
481 which was likely marcasite initially (e.g., Zhang et al., 2014; Lin et al., 2016a).

482 **SIMS results.** Both pyrite textures have been analyzed by SIMS in this study. A total of 25 spots  
483 were analyzed in the “pyrite flowers” and 21 spots were analyzed in the pyrite cores of the “Fe-oxide  
484 coronas” (Fig. 19; Appendix 5). For the first time, a bimodal distribution of  $\delta^{34}\text{S}$  values is found within a  
485 single sample at cm-scale (Figs. 22, 23). SIMS  $\delta^{34}\text{S}$  results of the “pyrite flowers” show remarkably  
486 homogeneous and high values ranging from +59.9‰ to +62.8‰, regardless of zoned textures under BSE  
487 (Figs. 18C, 19, 22, 23; Appendix 5). In contrast, the pyrite cores within the “Fe-oxide coronas” show a  
488 much wider range with much lower  $\delta^{34}\text{S}$  values, ranging from ca. +16.6‰ to ca. +32.7‰ with an average  
489 value of +22.2‰ (Figs. 18D, 20–23; Appendix 5).

## 490 **Pyrite $^{32}\text{S}^1\text{H}/^{32}\text{S}$ values**

491 During SIMS analysis, mass  $^{32}\text{S}^1\text{H}^-$  was also measured in order to check the irregularity of each  
492 spot. The mean value of  $^{32}\text{S}^1\text{H}/^{32}\text{S}$  in UWPy-1 is  $4.6\text{E}-4$  during the three sessions. Among the studied  
493 four samples, only pyrite analyses of Sample 3 show similar level (mean:  $7.4\text{E}-4$ ) of  $^{32}\text{S}^1\text{H}/^{32}\text{S}$ . Notably,  
494 pyrite analyses of Samples 1, 2 and 4 show  $^{32}\text{S}^1\text{H}/^{32}\text{S}$  values that are around two orders of magnitude  
495 higher than those of the UWPy-1 standard indicating the presence of a second hydrogen-bearing phase  
496 (Appendix 6).

497 Except for the  $\delta^{34}\text{S}$  values analyzed from a single pyrite nodule in Sample 1 that show a weak  
498 correlation with the  $^{32}\text{S}^1\text{H}/^{32}\text{S}$  values, most of the measured  $\delta^{34}\text{S}$  values in this study do not show apparent  
499 correlation with corresponding  $^{32}\text{S}^1\text{H}/^{32}\text{S}$  values (Appendix 6). For example,  $\delta^{34}\text{S}$  data measured from  
500 Sample 4 show a bimodal distribution (mean  $\delta^{34}\text{S}$  of superheavy pyrite flowers:  $+61.6\%$ ; mean  $\delta^{34}\text{S}$  of  
501 pyrite cores within Fe-oxide coronas:  $+22.2\%$ ), but all these data are coupled with  $^{32}\text{S}^1\text{H}/^{32}\text{S}$  values (mean  
502  $^{32}\text{S}^1\text{H}/^{32}\text{S}$  of superheavy pyrite flowers:  $9.7\text{E}-3$ ; mean  $^{32}\text{S}^1\text{H}/^{32}\text{S}$  of pyrite cores within Fe-oxide coronas:  
503  $1.3\text{E}-2$ ) that are around two orders of magnitude higher than the mean  $^{32}\text{S}^1\text{H}/^{32}\text{S}$  values of the UWPy-1  
504 standard. It is also notable that among superheavy pyrites,  $^{32}\text{S}^1\text{H}/^{32}\text{S}$  values can be very different. For  
505 example, superheavy pyrites in Samples 2 and 4 show  $^{32}\text{S}^1\text{H}/^{32}\text{S}$  values that are two orders of magnitude  
506 higher than the mean  $^{32}\text{S}^1\text{H}/^{32}\text{S}$  values of the UWPy-1 standard, while superheavy pyrite in Sample 3  
507 show  $^{32}\text{S}^1\text{H}/^{32}\text{S}$  values that are similar to those measured from UWPy-1.

508 Integrated SEM-SIMS results show that the  $^{32}\text{S}^1\text{H}/^{32}\text{S}$  values correlate with the pyrite textures  
509 under BSE. Pyrites in Sample 1, 2, and 4 show strong heterogeneity in brightness under BSE and have  
510 relatively high  $^{32}\text{S}^1\text{H}/^{32}\text{S}$  values, while pyrites in Sample 3 show relatively homogeneous in brightness  
511 under BSE and have relatively low  $^{32}\text{S}^1\text{H}/^{32}\text{S}$  values. It is possible that fluid inclusions or organic matter  
512 inclusions that are rich in hydrogen (leading to higher  $^{32}\text{S}^1\text{H}/^{32}\text{S}$  values) within pyrite in Samples 1, 2, and  
513 4 may have played a role in the BSE brightness and  $^{32}\text{S}^1\text{H}/^{32}\text{S}$  values.

514 In summary, the  $^{32}\text{S}^1\text{H}/^{32}\text{S}$  values measured during the SIMS sessions provide valuable  
515 information on the studied pyrite. No apparent correlation was found between  $^{32}\text{S}^1\text{H}/^{32}\text{S}$  and  $\delta^{34}\text{S}$  values.  
516  $^{32}\text{S}^1\text{H}/^{32}\text{S}$  values show an overall correlation with the pyrite brightness under BSE, which we regard can  
517 be explained by the contribution of fluid or organic inclusions mixed within pyrite.

## 518 **DISCUSSION**

519 A viable model for the genesis of the studied superheavy pyrite should be able to explain  
520 sedimentological and geochemical observations at both basin and micrometer scales. We will evaluate  
521 multiple models for the superheavy pyrite below.

### 522 **Superheavy pyrite formed via microbial sulfate reduction (MSR)?**

523 All the previously published biogeochemical models for the superheavy pyrite in South China  
524 assume a biogenic origin by microbial sulfate reduction (MSR) (Liu et al., 2006; Chen et al., 2008; Li et  
525 al., 2012; Lang et al., 2016; Wu et al., 2016; Wang et al., 2017). This assumption hypothesizes that  
526 superheavy pyrite formed in the marine water column or shallow sediments with different degrees of  
527 access to seawater sulfate. However, based on detailed SIMS-SEM study, the superheavy pyrite in the  
528 Datangpo Formation is found replacing preexisting rhodochrosite and illite (Figs. 9–13), and therefore  
529 formed after deep burial.

530 Supporting evidence for a non-MSR origin of the Datangpo superheavy pyrite also comes from  
531 its  $\mu\text{m}$ -scale  $\delta^{34}\text{S}$  patterns. Sample 2 shows remarkably homogenous  $\delta^{34}\text{S}$  values regardless of  
532 heterogeneous textures (Fig. 14); and Sample 3 shows a decreasing  $\delta^{34}\text{S}$  trend from the core to the edge of  
533 individual pyrite grains (Figs. 16, 17). These  $\mu\text{m}$ -scale  $\delta^{34}\text{S}$  patterns are inconsistent with a MSR origin

534 considering that progressive MSR in restricted pore waters would only increase, instead of decrease, the  
535 pyrite  $\delta^{34}\text{S}$  values. Therefore, previous models based on a MSR assumption cannot explain the textures or  
536  $\delta^{34}\text{S}$  values of studied superheavy pyrite either, and a non-MSR model is needed.

### 537 **Superheavy pyrite formed in a sulfide-rich fluid flow?**

538 It is possible that flow of a reducing hydrothermal fluid that is rich in sulfide, instead of sulfate,  
539 may have caused the mineralization of the studied superheavy pyrite. In this scenario, iron that may be  
540 available in the sediments reacts with external hydrogen sulfide and forms pyrite in the absence of  
541 simultaneous sulfate reduction. The flow of sulfide-rich fluid can be hypothesized to come from an  
542 underlying magmatic source. However, multiple lines of evidence suggest that this scenario is unlikely.

543 First, given the typically near-0  $\delta^{34}\text{S}_{\text{sulfide}}$  values ( $0 \pm 5\%$ ) of magmatic sulfur reservoirs (Marini  
544 et al., 2011), it would be extremely difficult for such a sulfur reservoir to generate  $\delta^{34}\text{S}_{\text{sulfide}}$  values as high  
545 as  $+70\%$  at a basinal scale in South China.

546 Second, a sulfide-rich source is inconsistent with the SIMS  $\delta^{34}\text{S}$  data shown in [Sample 3](#), where  
547 decreasing  $\delta^{34}\text{S}$  trends with a magnitude of ca.  $10\%$  are consistently registered from core to edge of each  
548 individual subhedral pyrite grain ([Figs. 16, 17](#)). Previous study shows that sulfur isotope fractionations  
549 between hydrogen sulfide and iron sulfide ( $\Delta^{34}\text{S}_{\text{FeS-H}_2\text{S}}$ ) are small ( $\sim 1\%$ ) (Böttcher et al., 1998), in strong  
550 contrast with MSR-induced fractionation ( $\Delta^{34}\text{S}_{\text{sulfate-sulfide}}$ ). Such small fractionation ( $\Delta^{34}\text{S}_{\text{FeS-H}_2\text{S}}$ ) cannot  
551 readily explain the  $\delta^{34}\text{S}_{\text{pyrite}}$  heterogeneity in [Sample 3](#) revealed by the SIMS data at a  $\mu\text{m}$  scale ([Figs. 16,](#)  
552 [17](#)).

553 Third, the discovery of barite and gypsum veins or infillings in the Datangpo Formation (Xu et al.,  
554 1990; Chen and Chen, 1992; He et al., 2013a; He et al., 2013b; Zhang et al., 2013; Pan et al., 2016)  
555 indicate the involvement of sulfate-rich, instead of sulfide-rich, fluids. Therefore, based on the above  
556 discussion, it is more likely that a non-MSR type sulfate reduction caused the mineralization of the  
557 studied superheavy pyrite. We will fully explore this scenario in the next section.

### 558 **Reinterpretation: superheavy pyrite formed by thermochemical sulfate reduction (TSR)**

559 In this study, we propose that the studied superheavy pyrite formed by thermochemical sulfate  
560 reduction (TSR) in hydrothermal fluids. This revised interpretation is supported by multiple lines of  
561 sedimentological and geochemical evidence listed below.

562 **Superheavy pyrite associated with ancient faults.** In South China, the superheavy pyrite in the  
563 Datangpo Formation is found closely associated with ancient faults (Wu et al., 2016). This distinct pattern  
564 suggests that the genesis of the Datangpo superheavy pyrite was controlled by external fluids that flowed  
565 along the faults. It is possible that an external sulfate-rich hydrothermal fluid intruded the Datangpo  
566 Formation along ancient faults, and caused the mineralization of the superheavy pyrite via TSR.

567 **Superheavy pyrite associated with Mn-rich carbonates.** In South China, most of the  
568 superheavy pyrites were found near or within the Mn-rich carbonate intervals in the basal Datangpo  
569 Formation. Detailed petrographic investigation in this study shows preferential replacement of carbonate  
570 by superheavy pyrite ([Figs. 9–13; Appendix 3](#)). Given that TSR is a process that produces hydrogen  
571 sulfide and increases pore-water acidity (Machel et al., 1995; Jiang et al., 2018), carbonate host rocks  
572 would be preferentially dissolved and then replaced by pyrite when TSR occurs (Kelley et al., 2004a).  
573 This process has also been reported in many other carbonate-dominated strata worldwide (e.g., Krouse et  
574 al., 1988; Worden and Smalley, 1996; Cai et al., 2001; Biehl et al., 2016; Jiang et al., 2018). Therefore,  
575 the reinterpretation of a TSR origin for the studied superheavy pyrite is consistent with the close coupling  
576 between superheavy pyrite and Mn-rich carbonates.

577 **Paragenesis.** In contrast with MSR that dominantly occurs in the water column or shallow  
578 marine sediments (Jørgensen and Kasten, 2006; Bowles et al., 2014), TSR usually occurs relatively late,  
579 typically in temperatures higher than 100 °C during deep burial diagenesis. Integrated SEM-SIMS results  
580 in Sample 2 show pervasive replacement of rhodochrosite and illite by superheavy pyrite (Figs. 9–13;  
581 Appendix 3), suggesting that superheavy pyrite is a late diagenetic product. The reinterpretation of a TSR  
582 origin for the studied superheavy pyrite is consistent with independent paragenesis revealed by SEM  
583 petrography.

584 **Barite and gypsum veins and infillings.** Field observations of the Datangpo Formation show  
585 abundant textures that suggest pervasive overprint by hydrothermal fluids, including host-rock breccia,  
586 quartz veins, calcite, gypsum, and barite infillings and veins (Xu et al., 1990; Chen and Chen, 1992; He et  
587 al., 2013a; He et al., 2013b; Zhang et al., 2013; Pan et al., 2016). The preservation of barite and gypsum  
588 veins indicates that the hydrothermal fluids were rich in sulfate, which would trigger TSR to occur given  
589 that organic matter is abundant in the Datangpo shale.

590 **Homogeneous  $\delta^{34}\text{S}$  in heterogeneous pyrite textures.** In this study, superheavy pyrite in some  
591 samples shows remarkably homogenous  $\delta^{34}\text{S}_{\text{pyrite}}$  values in zoned pyrite grains (Figs. 22, 23). In Sample 2,  
592 the  $\delta^{34}\text{S}_{\text{pyrite}}$  values of 28 SIMS spots in framboidal pyrite and lacy pyrite overgrowth range from +56.3‰  
593 to +60.4‰ (Fig. 14). In Sample 4, the  $\delta^{34}\text{S}_{\text{pyrite}}$  values of 25 SIMS spots in zoned “pyrite flowers” range  
594 from +59.9‰ to +62.8‰ (Fig. 19). Such homogeneous  $\delta^{34}\text{S}_{\text{pyrite}}$  patterns are difficult to explain by MSR.  
595 Typically, MSR-derived pyrite shows considerable  $\delta^{34}\text{S}$  zoning at  $\mu\text{m}$  scale due to a biogenic nature of  
596 MSR and the effect of Rayleigh fractionation in an increasingly restricted pore water environment (Kohn  
597 et al., 1998; Williford et al., 2011). Alternatively, it is likely that these relatively invariant  $\delta^{34}\text{S}_{\text{pyrite}}$  values  
598 result from TSR in hydrothermal fluids. The superheavy pyrite of different textures may have precipitated  
599 in response to a hydrothermal fluid flow when it intruded into the host rocks.

600 **Decreasing  $\delta^{34}\text{S}$  trend from core to edge of individual pyrite grains.** In this study,  $\mu\text{m}$ -scale  
601  $\delta^{34}\text{S}$  analysis reveals decreasing  $\delta^{34}\text{S}$  trends in core-to-edge traverses of individual pyrite grains from  
602 Sample 3 (Figs. 16, 17). This phenomenon is inconsistent with MSR, which typically leads to an  
603 increasing trend at  $\mu\text{m}$ -scales. Alternatively, the core-to-rim traverses in Sample 3 can be explained by  
604 TSR when the temperature of the hydrothermal fluid cools. Lab experiments on kinetic sulfur isotope  
605 fractionation during TSR have demonstrated that as temperature decreases,  $\Delta^{34}\text{S}_{\text{sulfate-sulfide}}$  would increase,  
606 and consequently  $\delta^{34}\text{S}_{\text{pyrite}}$  would decrease (Kiyosu and Krouse, 1990). As a result, a gradient with  
607 decreasing  $\delta^{34}\text{S}_{\text{pyrite}}$  values would be recorded in individual TSR-derived pyrite grains.

608 **Varying  $\delta^{34}\text{S}_{\text{pyrite}}$  at a basin scale.** Published chemostratigraphic  $\delta^{34}\text{S}_{\text{pyrite}}$  profiles of the  
609 Datangpo Formation at different sections in South China show remarkably different values (Fig. 1) (Li et  
610 al., 1999a; Li et al., 2012; Zhou et al., 2013; Zhu et al., 2013; Wu et al., 2015a; Lang, 2016; Wu et al.,  
611 2016). For example,  $\delta^{34}\text{S}_{\text{pyrite}}$  values in the lower Datangpo Formation at the Yangjiaping section range  
612 from +20‰ to +30‰, while  $\delta^{34}\text{S}_{\text{pyrite}}$  values of the correlative Minle section range from +40‰ to +65‰  
613 (Li et al., 2012). These different  $\delta^{34}\text{S}_{\text{pyrite}}$  values among different sections have been interpreted to result  
614 from a stratified ocean controlled by dynamic influx of sulfate and nutrient (Li et al., 2012). However,  
615 sedimentological observations show that most of the high- $\delta^{34}\text{S}_{\text{pyrite}}$  values are associated with Mn-rich  
616 carbonate intervals and ancient faults (e.g., Minle section in Li et al., 2012), while siliciclastic-dominated  
617 sections (e.g., Yangjiaping section in Li et al., 2012) lack superheavy pyrite. We interpret this isotope-  
618 lithology pattern as resulting from preferential replacement of carbonates by superheavy pyrite via TSR.  
619 The occurrence of TSR may have caused a strong bias of superheavy pyrite preservation in carbonate-  
620 dominated intervals, and as a result, overprinted the primary  $\delta^{34}\text{S}_{\text{pyrite}}$  signals.

621 **Negative correlation between Fe content and bulk  $\delta^{34}\text{S}_{\text{pyrite}}$  values.** Previous studies have  
622 reported an overall negative correlation (correlation coefficient/ $R = -0.83$ ,  $n = 8$ ) between bulk Fe content  
623 and bulk  $\delta^{34}\text{S}_{\text{pyrite}}$  values in the Datangpo Mn-rich carbonates (Fig. 15 of Wu et al., 2016). This

624 phenomenon has been interpreted as resulting from Rayleigh distillation in seawater. However,  
625 petrographic observations in this study suggest that the bulk Fe content in the Mn-rich carbonates is  
626 mainly post-depositional pyrite replacing pre-existing carbonates. Therefore, it is more likely that this  
627 overall negative correlation reflects Rayleigh distillation in restricted hydrothermal fluids within deeply  
628 buried sediments. If correct, then TSR would be the more likely pathway of sulfate reduction instead of  
629 MSR. As TSR progressively occurs with Rayleigh distillation,  $\delta^{34}\text{S}_{\text{pyrite}}$  would evolve to higher values.  
630 Therefore, the Rayleigh distillation process would be characterized by a relatively larger amount of pyrite  
631 (therefore high bulk Fe content) with relatively low  $\delta^{34}\text{S}_{\text{pyrite}}$  values at the early stage and a relatively  
632 smaller amount of pyrite (therefore low bulk Fe content) with high  $\delta^{34}\text{S}_{\text{pyrite}}$  values (i.e., superheavy pyrite)  
633 at the very late stage. This process can cause a broad spectrum of  $\delta^{34}\text{S}_{\text{pyrite}}$  values with an overall negative  
634 correlation between bulk Fe content and bulk  $\delta^{34}\text{S}_{\text{pyrite}}$  values.

635 **Negative correlation between total organic carbon and total sulfur.** An overall negative  
636 correlation (correlation coefficient,  $R = -0.48$ ,  $n = 29$ ) between total organic carbon (TOC) and total  
637 sulfur (TS) was reported in the Datangpo Mn-rich carbonates (Wang et al., 2017). This pattern is in strong  
638 contrast with normal marine environments where TOC and TS typically show positive correlations  
639 (Berner, 1984; Berner, 1989; Cao et al., 2016). The negative TOC–TS correlation observed in the  
640 Datangpo Formation was interpreted to result from anomalous sulfur cycling during deposition (Wang et  
641 al., 2017). Petrographically, the low-TOC samples are mostly carbonates that are rich in superheavy  
642 pyrites (therefore high in TS). On the other hand, the high-TOC samples are mostly shales that have less  
643 pyrite abundance (therefore lower in TS). The new results of this study show that this overall negative  
644 TOC–TS correlation actually results from preferential replacement of carbonates by TSR-derived pyrite,  
645 therefore cannot be used to infer marine sulfur cycles.

646 **Temperature data.** Studies on vitrinite reflectance of the Datangpo Formation suggest that the  
647 Mn-rich carbonate interval experienced a maximum burial temperature of ca. 195 °C (Chen and Chen,  
648 1992; Xie et al., 1999). Studies of fluid inclusions in authigenic quartz in the Datangpo Formation yield  
649 homogenization temperatures of 173–241 °C, with an average value of 194 °C (Wang et al., 1985). These  
650 temperatures are consistent with the scenario that the Datangpo Formation experienced a hydrothermal  
651 event.

652 Based on the current burial depth of the studied Datangpo drill core (Samples 1, 2, 3, 4 collected  
653 at depths of 1303.06 m, 1299.88 m and 1289.09 m, 1274.14 m, respectively) and the current geothermal  
654 gradient of 10–20 °C/km in the studied region (Yuan et al., 2006), assuming the surface temperature is ca.  
655 20 °C, the current burial temperature is likely to be ca. 33–46 °C at the sampled depths. This shows that  
656 the Datangpo Formation should have experienced a cooling event from a hydrothermal or maximum  
657 burial temperature to the current burial temperature, which is consistent with the  $\mu\text{m}$ -scale  $\delta^{34}\text{S}_{\text{sulfide}}$  spatial  
658 patterns shown in [Sample 3](#).

## 659 **Source and compositions of the TSR fluids**

660 To allow TSR to occur, sulfate-rich hydrothermal fluids and organic-rich host rocks are both  
661 required. Given the high abundance of organic matter in the Datangpo Formation, sulfate-rich  
662 hydrothermal fluid is more likely to be the controlling factor. Typically, the fluids for TSR are derived  
663 from late dissolution of preexisting sulfate minerals (e.g., gypsum, anhydrite). Therefore, the deposition  
664 of sulfate has to predate the TSR event.

665 In South China, the oldest gypsum-bearing sedimentary bedding with a basin-scale distribution is  
666 the late-Ediacaran Dengying Formation. Distinct textures that point to the deposition of marine evaporites  
667 have been widely reported in this formation (Xi, 1987; Siegmund and Erdtmann, 1994; Lu et al., 2013;  
668 Wang et al., 2013; Duda et al., 2015; Cui et al., 2016b). Due to high solubility, evaporites in this  
669 formation are mostly shown as calcite pseudomorphs with distinct crystal shapes that are diagnostic of

670 preexisting gypsum (Duda et al., 2015; Cui et al., 2016b). The  $\delta^{34}\text{S}_{\text{sulfate}}$  value of this gypsum-bearing  
671 interval has been constrained to be ca. +40‰ based on carbonate associated sulfate (CAS) analysis (Cui,  
672 2015; Cui et al., 2016b), which is consistent with the  $\delta^{34}\text{S}_{\text{sulfate}}$  constraints based on CAS analysis of  
673 coeval strata in Arctic Siberia (Cui et al., 2016a) and direct  $\delta^{34}\text{S}_{\text{sulfate}}$  analyses of bedded anhydrite strata in  
674 Oman (Fike and Grotzinger, 2008; Fike and Grotzinger, 2010; Bergmann, 2013). We propose that this  
675 could be the source of hydrothermal sulfate for the Datangpo TSR event.

## 676 **Rayleigh distillation model for superheavy pyrite**

677 To generate superheavy pyrite with  $\delta^{34}\text{S}_{\text{pyrite}}$  as high as +70‰, it is required that the  $\delta^{34}\text{S}_{\text{sulfate}}$   
678 values of an equilibrated TSR solution to be higher than +70‰. Figure 24 shows models of sulfide  
679 precipitation by batch precipitation in a closed system and by Rayleigh distillation. In these models, an  
680 initial  $\delta^{34}\text{S}_{\text{sulfate}}$  value of +40‰ was adopted assuming that the sulfate source of this TSR fluid is the  
681 Ediacaran Dengying Formation in South China and an equilibrium value of  $\Delta^{34}\text{S}_{\text{sulfate-sulfide}} = 40\text{‰}$ . These  
682 calculations show that  $\delta^{34}\text{S}_{\text{sulfide}}$  values above +70‰ can be generated after precipitation of 80% of sulfate  
683 in closed system fluids.

684 It needs to be noted that the above calculation represents a simplified scenario with a constant  
685  $\Delta^{34}\text{S}_{\text{sulfate-sulfide}}$  of 40‰. Published lab experiments suggest that the  $\Delta^{34}\text{S}_{\text{sulfate-sulfide}}$  value at equilibrium is ~  
686 40‰ (Friedman and O'Neil, 1977) or ~30‰ (Ohmoto and Lasaga, 1982; Ohmoto, 1986; Ohmoto and  
687 Goldhaber, 1997; Seal, 2006) at the temperature of ~200 °C. The  $\Delta^{34}\text{S}_{\text{sulfate-sulfide}}$  value would be  
688 significantly higher at lower temperature. It is possible that the hydrothermal fluid temperatures vary as  
689 TSR occurs. In geological conditions, the precipitation of superheavy pyrite can be a dynamic process  
690 with varying  $\delta^{34}\text{S}_{\text{sulfate}}$ , temperatures,  $\Delta^{34}\text{S}_{\text{sulfate-sulfide}}$  and  $\delta^{34}\text{S}_{\text{pyrite}}$  values. Regardless, our model  
691 demonstrates that  $\delta^{34}\text{S}_{\text{sulfate}}$  and  $\delta^{34}\text{S}_{\text{sulfide}}$  signals as high as +70‰ can be produced via TSR during the late  
692 stage of Rayleigh distillation. This process could occur when hydrothermal fluids flow along ancient  
693 faults, during which pyrite with a spectrum of  $\delta^{34}\text{S}_{\text{pyrite}}$  values may have been produced via TSR.

## 694 **IMPLICATIONS**

### 695 **Rethinking the Neoproterozoic sulfur cycle**

696 The occurrence of the Neoproterozoic superheavy pyrite has led to the speculation of  
697 anomalously low sulfate concentrations in the ocean (Hayes et al., 1992; Hurtgen et al., 2002; Canfield,  
698 2004; Li et al., 2012; Wu et al., 2016). However, in light of the petrographic and isotopic results in this  
699 study, we argue that the studied superheavy pyrite formed in deeply buried sediments by hydrothermal  
700 fluids and therefore cannot be used to infer the marine sulfur cycles during deposition. Similar SEM-  
701 SIMS studies have not yet been published for other localities. It is possible that the sulfate concentration  
702 in the Cryogenian ocean may not be as low as the previous studies suggested.

703 Cryogenian superheavy pyrite has been reported from five post-Sturtian successions worldwide:  
704 the Datangpo Formation in South China; the Tapley Hill and Aralka formations in Australia; the Court  
705 Formation in Namibia; and the Arena Formation in East Greenland (Fig. 1). In light of our study of the  
706 Datangpo Formation in South China, similar investigations are suggested in other localities to assess the  
707 nature of the high- $\delta^{34}\text{S}$  signals. It needs to be noted that the current time-series  $\delta^{34}\text{S}$  compilation (Canfield,  
708 2001a; Shen et al., 2001; Cui et al., 2016a; Cui et al., 2016b) is based on pyrite that has been regarded as  
709 early diagenetic in origin. TSR-derived superheavy pyrite can be much more abundant in geological  
710 record than the time-series  $\delta^{34}\text{S}$  compilation shows.

711 The new data from South China suggest that at least some Neoproterozoic superheavy pyrite  
712 formed by late diagenetic alteration. If this observation applies to other localities, then an emerging  
713 question is, why is superheavy pyrite particularly notable in the Neoproterozoic interval? Here, we

714 propose that three potential factors may have played a role in contributing to the occurrence of the  
715 Neoproterozoic superheavy pyrite.

716 **Increased diagenetic potential for TSR.** Considering that bedded sulfate evaporites are  
717 increasingly deposited during and after the Neoproterozoic (Kah et al., 2004; Halverson and Hurtgen,  
718 2007; Kah and Bartley, 2011; Cui et al., 2016b), it is likely that the considerable rise in seawater sulfate  
719 concentrations during the Neoproterozoic Oxygenation Event promoted evaporite deposition (Shields-  
720 Zhou and Och, 2011; Och and Shields-Zhou, 2012), which consequently enhanced the diagenetic  
721 potential for TSR during deep burial. When these evaporites are dissolved by hydrothermal fluids, TSR  
722 would occur if organic matter is also available in the host sedimentary strata.

723 **High  $\delta^{34}\text{S}_{\text{sulfate}}$  during the Neoproterozoic.** It is notable that time-series  $\delta^{34}\text{S}_{\text{sulfate}}$  values remain  
724 high during the Neoproterozoic and reach to the maximum (ca. +40‰) during the late Ediacaran Period  
725 (Fike and Grotzinger, 2008; Halverson et al., 2009; Halverson et al., 2010; Paytan and Gray, 2012; Cui et  
726 al., 2016a; Cui et al., 2016b). The high  $\delta^{34}\text{S}_{\text{sulfate}}$  signals of the Neoproterozoic seawater may have been  
727 recycled after deposition (e.g., post-depositional dissolution of gypsum), facilitating the genesis of  
728 superheavy pyrite in the host rocks during a post-depositional TSR event.

729 **Increased tectonic activity.** The breakup of the Rodinia supercontinent and progressive  
730 formation of the Gondwana supercontinent during the Neoproterozoic Era (Li, 2011; Li et al., 2013) may  
731 have also played an active role in facilitating TSR in sedimentary strata. The process of continental  
732 reconfiguration may have enhanced the activity of hydrothermal fluids, and thus promoted TSR to occur  
733 in the Neoproterozoic.

734 We propose that the above factors may have played a role in facilitating TSR in the  
735 Neoproterozoic record in South China and possibly beyond. The Neoproterozoic superheavy pyrites in  
736 other localities are suggested to be examined in a similar way in order to better test the above hypotheses.

### 737 **Diverse origins of framboidal pyrite**

738 Framboidal pyrite in sedimentary records has been widely regarded as either formed in seawater  
739 or during diagenesis via MSR in low temperature conditions. Framboids often start to grow in the water  
740 column, followed by early diagenetic overgrowth in shallow marine sediments (Raiswell, 1982;  
741 Schallreuter, 1984; Wilkin et al., 1996; Wilkin and Barnes, 1997; Popa et al., 2004; Schieber, 2011).  
742 Based on the pioneering work by Wilkin et al. (1996) and then followed by Bond and Wignall (2010), the  
743 size distribution of pyrite framboids has been widely used to infer the redox conditions of seawater during  
744 deposition. However, more complexities are revealed in the samples of this study showing that origin,  
745 texture, size, and isotopic values of framboidal pyrite can be diverse.

746 First, the size of pyrite framboids can be significantly affected by late-stage pyrite overgrowth.  
747 Pyrite framboids can be partially or completely masked by late-stage pyrite overgrowth (Figs. 6, 7, 11–  
748 14), which cannot be detected without SEM imaging. Similar phenomena have also been reported from  
749 the Ediacaran samples (Wacey et al., 2015; Liu, 2016) and pyrites in modern marine sediments (Lin et al.,  
750 2016b; Lin et al., 2017).

751 Second, both MSR- and TSR-derived framboidal pyrites have been found in the studied samples.  
752 These two types of framboid have distinct characteristics in petrography, paragenesis and  $\delta^{34}\text{S}_{\text{pyrite}}$  spatial  
753 patterns at  $\mu\text{m}$  scale. The framboidal pyrite in diamictite **Sample 1** shows heterogeneous  $\delta^{34}\text{S}_{\text{pyrite}}$  values  
754 (Figs. 7, 22, 23), and is interpreted to be syngenetic (in water column) or early diagenetic (in shallow  
755 marine sediments) in origin and formed by MSR. In contrast, the framboidal pyrite in **Sample 2 and**  
756 **Sample 4** records remarkably homogeneous and superheavy  $\delta^{34}\text{S}_{\text{pyrite}}$  values in spite of heterogeneous  
757 textures (Figs. 14, 19), which are interpreted to be formed via TSR by migrating hydrothermal fluids.

758 Supporting evidence for the existence of framboidal pyrite with a hydrothermal origin also comes  
759 from studies on both natural and synthetic pyrite framboids. Framboidal pyrites nucleated in hydrothermal  
760 veins or ores have been reported (Rust, 1935; Love and Amstutz, 1969; Ostwald and England, 1979; Scott  
761 et al., 2009). Additionally, lab experiments have demonstrated that framboidal pyrite can be synthesized  
762 at temperatures as high as 350 °C within a few hours (Sunagawa et al., 1971; Graham and Ohmoto, 1994;  
763 Ohfuji and Rickard, 2005). These studies suggest that framboidal pyrite of a high temperature origin is  
764 possible in both natural and lab environments.

765 Taken together, framboidal pyrite can be formed in both marine and hydrothermal (>100 °C)  
766 conditions. Observations by reflected light microscopy alone are insufficient to detect the origins of pyrite.  
767 Detailed SEM petrography and  $\mu\text{m}$ -scale  $\delta^{34}\text{S}_{\text{pyrite}}$  analysis by SIMS are a powerful approach to  
768 interrogate the genesis of framboids.

## 769 CONCLUSIONS

770 (1) To interrogate the origins of the Neoproterozoic superheavy pyrite (Fig. 1), detailed  
771 petrographic and in situ  $\delta^{34}\text{S}$  analyses (Figs. 3–21, Appendix 2–6) were conducted using scanning  
772 electron microscopy and secondary ion mass spectrometry (SEM-SIMS) for pyrite in the Cryogenian  
773 Tiesi'ao and Datangpo formations at unprecedented spatial resolution (2  $\mu\text{m}$  spot size). Distinct spatial  
774 patterns of  $\delta^{34}\text{S}_{\text{pyrite}}$  values at  $\mu\text{m}$  scale are found to be correlated with pyrite morphology and genesis  
775 (Table 1; Figs. 22, 23).

776 (2) Petrographic observations show that the Datangpo superheavy pyrite postdates the  
777 mineralization of rhodochrosite and illite (Figs. 9–13; Appendix 3) and thus is late diagenetic in origin.  
778 This refutes the long-held belief that these framboids are syngenetic (in water column) or early diagenetic  
779 (in shallow marine sediments).

780 (3) Framboidal pyrites of both marine and hydrothermal origins were found in this study.  
781 Framboidal pyrite in the Tiesi'ao diamictite (Sample 1) shows heterogeneous (+11.2‰ to +28.3‰),  
782 relatively low (+16.4‰ in average)  $\delta^{34}\text{S}_{\text{pyrite}}$  values and a relatively wide range of grain sizes (up to 30  $\mu\text{m}$   
783 in diameter) (Fig. 5–7; Appendix 2). In contrast, the framboidal pyrite in Mn-rich carbonates (Sample 2)  
784 from the basal Datangpo Formation shows homogeneous (+56.3‰ to +60.4‰) and superheavy (+57.6‰  
785 average)  $\delta^{34}\text{S}_{\text{pyrite}}$  values and relatively small grain sizes (<7  $\mu\text{m}$  diameter) (Figs. 11–14; Appendix 3).  
786 Sample 1 is interpreted to be syngenetic or early diagenetic in origin and formed by microbial sulfate  
787 reduction (MSR), while Sample 2 is interpreted to be hydrothermal in origin and formed by  
788 thermochemical sulfate reduction (TSR) (Table 1). The use of the size distribution of framboidal pyrite to  
789 infer paleo-redox conditions should be done with caution.

790 (4) Pyrite in one studied Datangpo shale sample from drill core (Sample 3) shows heterogeneous  
791 (+60.3‰ to +71.2‰) and superheavy (+66.3‰ average)  $\delta^{34}\text{S}_{\text{pyrite}}$  values at  $\mu\text{m}$  scales (Figs. 16, 17;  
792 Appendix 4). It is notable that a decreasing  $\delta^{34}\text{S}_{\text{pyrite}}$  trend is consistently recorded from the core to the  
793 edge of individual pyrite grains in Sample 3 (Figs. 16, 17; Appendix 4). This is in strong contrast with  
794 biogenic pyrite, which typically shows an increasing  $\delta^{34}\text{S}_{\text{pyrite}}$  trend from the core to the edge of individual  
795 pyrite grains. It is proposed that the decreasing  $\delta^{34}\text{S}_{\text{pyrite}}$  trend results from TSR with increasing sulfur  
796 isotope fractionations between sulfate and sulfide as hydrothermal fluids cool.

797 (5) Based on multiple lines of sedimentological and geochemical evidence at both basinal- and  
798  $\mu\text{m}$ -scales, we argue that the superheavy pyrite in the Cryogenian strata in South China formed via  
799 thermochemical sulfate reduction (TSR), instead of microbial sulfate reduction (MSR). This is the first  
800 time that a post-depositional, hydrothermal origin is proposed for the superheavy pyrite in South China.

801 (6) We propose that post-depositional TSR plays an influential role in generating high  $\delta^{34}\text{S}$  values.  
802 Consequently, interpretations of the high  $\delta^{34}\text{S}$  values from the ancient geological record should reconsider

803 the influence that similar post-depositional processes may have in generating superheavy pyrite associated  
804 with noteworthy biogeochemical events in the Earth's history. Our study demonstrates that the integrated  
805 SEM-SIMS approach to  $\delta^{34}\text{S}_{\text{pyrite}}$  analysis of individual pyrite grains is an effective tool to assess the  
806 veracity of sedimentary pyrite in chemostratigraphic studies.

## 807 **ACKNOWLEDGEMENT**

808 This paper is a contribution to the American Mineralogist Special Collection “Isotopes, Minerals,  
809 And Petrology: Honoring John Valley”. The authors thank William Peck, Aaron Cavosie, and Jade Star  
810 Lackey for organizing this special collection of papers. The first author HC is currently a Post-Doc  
811 working with JWV and expresses his gratitude to JWV for mentorship, scholarship, passion, and support.  
812 This study could not have been made without the cohesive, inclusive, and positive atmosphere in the  
813 WiscSIMS and SEM labs, Department of Geoscience, University of Wisconsin–Madison.

814 This study is supported by the NASA Astrobiology Institute (NNA13AA94A). The WiscSIMS  
815 Lab is supported by NSF (EAR–1355590, –1658823) and the University of Wisconsin–Madison. JWV is  
816 also supported by NSF (EAR-1524336) and DOE (DE-FG02-93ER14389). The authors thank Bil  
817 Schneider, Tina Hill and Phil Gopon for assistance in the SEM lab; Brian Hess, Noriko Kita, James Kern,  
818 Ian Orland, and Maciej Śliwiński for assistance in sample preparation and SIMS analysis; Huifang Xu for  
819 assistance in the microscope lab. We also thank Alan Jay Kaufman, Ganqing Jiang, Shuhai Xiao, Xianguo  
820 Lang, Kang-Jun Huang, and Maciej Śliwiński for helpful comments. This paper is improved by  
821 constructive reviews by David Fike and an anonymous reviewer. We thank Keith Putirka (editor) and  
822 Aaron Cavosie (associate editor) for handling this manuscript.

## 823 **CONTRIBUTIONS**

824 H.C. designed research; F.Z. provided samples; H.C. and K.K. performed SIMS analysis at  
825 J.W.V.'s WiscSIMS lab; H.C. and J.H.F. performed SEM and EPMA analyses; H.C. interpreted the data  
826 with contributions from all coauthors. H.C. wrote the manuscript with significant input from J.W.V. All  
827 authors contributed to discussion and manuscript revision.

828

## 829 **APPENDIX 1**

830 Compilation of the published  $\delta^{34}\text{S}$  data measured from the Cryogenian post-glacial strata in China, UK,  
831 Namibia, and Australia.

## 832 **APPENDIX 2**

833 Integrated SEM-SIMS results of the drill core Sample 1 (Hy59, Sturtian glacial diamictite). Sample  
834 collected from the Cryogenian Tiesi'ao Formation, Daotuo mine, Guizhou Province, South China.

## 835 **APPENDIX 3**

836 Integrated SEM-SIMS results of the drill core Sample 2 (Hy55, Mn-rich carbonates). Sample collected  
837 from the Member 1 of the Cryogenian Datangpo Formation, Daotuo mine, Guizhou Province, South  
838 China.

## 839 **APPENDIX 4**

840 Integrated SEM-SIMS results data of the drill core Sample 3 (Hy31, black shale). Sample collected from  
841 the Member 1 of the Cryogenian Datangpo Formation, Daotuo mine, Guizhou Province, South China.

842 **APPENDIX 5**

843 Integrated SEM-SIMS results SIMS data of the drill core Sample 4 (Hy1, shale). Sample collected from  
844 the Member 2 of the Cryogenian Datangpo Formation, Daotuo mine, Guizhou Province, South China.

845 **APPENDIX 6**

846 Time-series plots and cross-plots of all the SIMS results in this study.

847 **APPENDIX 7**

848 Tables of all the SIMS  $\delta^{34}\text{S}$  data in this study. The data were generated in three separate SIMS sessions:  
849 Session 1 (Oct. 18-19, 2016), Session 2 (May 22, 2017), and Session 3 (June 8, 2017). Sulfur two-  
850 isotopes ( $^{32}\text{S}$ ,  $^{34}\text{S}$ ) were measured with a 2- $\mu\text{m}$ -diameter beam size in Sessions 1 and 3. Sulfur three  
851 isotopes ( $^{32}\text{S}$ ,  $^{34}\text{S}$ ,  $^{33}\text{S}$ ) were measured with a 10- $\mu\text{m}$ -diameter beam size in Session 2.

852 **APPENDIX 8**

853 Table of all the elemental concentration data for pyrite by EPMA in this study.

854

855

856

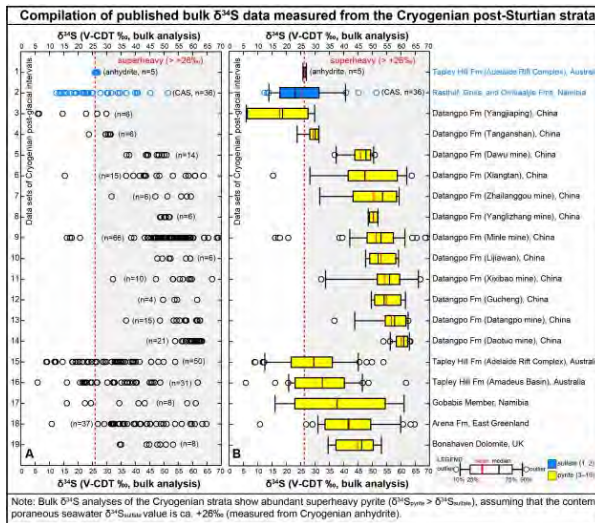
**TABLE 1**

857 **TABLE 1.** Summary of SEM-SIMS results in this study of Cryogenian pyrite from Daotuo, South China.  
 858 For the detailed petrographic context of all the geochemical data, the reader is referred to the online  
 859 appendices ([Appendices 2–5](#)).

SIMS samples	Sample 1 (Hy59)	Sample 2 (Hy55)	Sample 3 (Hy31)	Sample 4 (Hy1)
<b>Stratigraphic position</b>	Uppermost Tiesi'ao Fm	Basal Mb 1, Datangpo Fm	Mb 1, Datangpo Fm	Mb 2, Datangpo Fm
<b>Lithology</b>	Terminal-Sturtian glacial diamictite	Post-Sturtian Mn-rich carbonates	Post-Sturtian black shale	Post-Sturtian shale
<b>SEM-SIMS results</b>	<a href="#">Figs. 5–8;</a> <a href="#">Appendix 2</a>	<a href="#">Figs. 9–14;</a> <a href="#">Appendix 3</a>	<a href="#">Figs. 15–17;</a> <a href="#">Appendix 4</a>	<a href="#">Figs. 18–21;</a> <a href="#">Appendix 5</a>
<b>Pyrite morphology and grain size</b>	Framboidal pyrite: up to ~30 $\mu\text{m}$ ; Pyrite nodules: ~1 to ~2 mm	Framboidal pyrite: up to 7 $\mu\text{m}$ ; Lacy pyrite overgrowth: $\mu\text{m}$ to cm scale, showing lacy textures, metasomatic corrosion boundaries, and relatively darker color (compared with the framboids) under BSE	Subhedral pyrite: mostly 20 to 100 $\mu\text{m}$ ; Large pyrite with cemented individual pyrite grains: up to ~2 mm	Superheavy pyrite flowers (~15 $\mu\text{m}$ in diameter): framboidal pyrite cores (~5 $\mu\text{m}$ in diameter) with zoned pyrite overgrowth of ~5 $\mu\text{m}$ in thickness; Fe-oxide coronas with pyrite rim (~35 $\mu\text{m}$ in diameter) and pyrite cores (~10 $\mu\text{m}$ in diameter)
<b>Number of SIMS analyses (n)</b>	Framboidal pyrite: n=76; Pyrite cements outside framboids: n=4; Pyrite nodules: n=10	Framboidal pyrite: n=5; Lacy pyrite overgrowth: n=15; Mixture between framboids and overgrowth: n=8	Subhedral pyrite grains: n=85; Later-stage pyrite cement: n=23	Superheavy pyrite flowers: n=25; Pyrite within Fe-oxide coronas: n=21
<b>Range of SIMS <math>\delta^{34}\text{S}</math> values ‰ V-CDT</b>	Pyrite nodules: +9.8 to +52.2‰; Pyrite framboids: +11.2 to +28.3‰; Pyrite cements outside framboids: +22.7 to +36.7‰	Lacy pyrite overgrowth: +56.3 to +60.4‰; Mixture of framboids and overgrowth: +56.8 to +58.3‰; Pyrite framboids: +56.3 to +57.4‰	Individual pyrite grains: +60.3 to +71.2‰; Pyrite cements: +60.2 to +64.8‰	Superheavy pyrite flowers: +59.9 to +62.8‰; Pyrite cores within Fe-oxide coronas: +16.6 to +32.7‰
<b>Mean <math>\delta^{34}\text{S}</math> ‰ V-CDT</b>	Pyrite nodules: +26.5‰; Pyrite framboids: +16.4‰; Pyrite cements outside	Lacy pyrite overgrowth: +57.8‰; Mixture of framboids and overgrowth: +57.4‰; Pyrite framboids:	Individual pyrite grains: +66.3‰; Pyrite cements: +62.0‰	Superheavy pyrite flowers: +61.6‰; Pyrite cores within Fe-oxide coronas: +22.2‰

	framboids: +30.9‰	+56.9‰		
<b>Intra-grain <math>\delta^{34}\text{S}</math> pattern</b>	No systematic increasing or decreasing $\delta^{34}\text{S}$ trend	Not available	Systematic decreasing $\delta^{34}\text{S}$ trend from core to edge of each individual grain	Not available
<b><math>\delta^{34}\text{S}</math> patterns on <math>\mu\text{m}</math> scales</b>	Heterogeneous, mostly not superheavy	Homogeneous, superheavy	Individual pyrite grains: heterogeneous (in the range of $\sim 10\text{‰}$ ), superheavy; Pyrite cements: homogeneous, superheavy	Superheavy pyrite flowers: homogeneous, superheavy; Pyrite cores within Fe-oxide coronas: heterogeneous (in the range of $\sim 16\text{‰}$ ), not superheavy
<b>Mean <math>^{32}\text{S}^1\text{H}^3\text{S}</math></b>	Pyrite nodules: $8.7\text{E}-3$ Pyrite framboids: $1.2\text{E}-2$ Pyrite cements outside framboids: $1.0\text{E}-2$	Lacy pyrite overgrowth: $1.6\text{E}-2$ Mixture of framboids and overgrowth: $1.5\text{E}-2$ 2 Pyrite framboids: $1.3\text{E}-2$	Individual pyrite grains: $7.0\text{E}-4$ Pyrite cements: $8.5\text{E}-4$	Superheavy pyrite flowers: $9.7\text{E}-3$ Pyrite cores within Fe-oxide coronas: $1.3\text{E}-2$
<b>Paragenesis</b>	Framboidal pyrite: syngenetic (water column) to early diagenesis; Pyrite nodules: early to late diagenesis	Framboidal pyrite: late diagenesis (petrographically replacing rhodochrosite and illite); Lacy pyrite overgrowth: postdating framboids	Disseminated subhedral pyrite: interpreted to be formed during late diagenesis; Pyrite cements: postdating individual pyrite grains	Superheavy pyrite flowers: late diagenesis; Pyrite cores within Fe-oxide coronas: syngenetic (water column) to early diagenesis
<b>Interpretation in this study</b>	Biogenic, microbial sulfate reduction	Abiogenic, thermochemical sulfate reduction	Abiogenic, thermochemical sulfate reduction	Superheavy pyrite flowers: abiogenic, thermochemical sulfate reduction; Pyrite cores within Fe-oxide coronas: biogenic, microbial sulfate reduction

860 **FIGURE CAPTIONS**

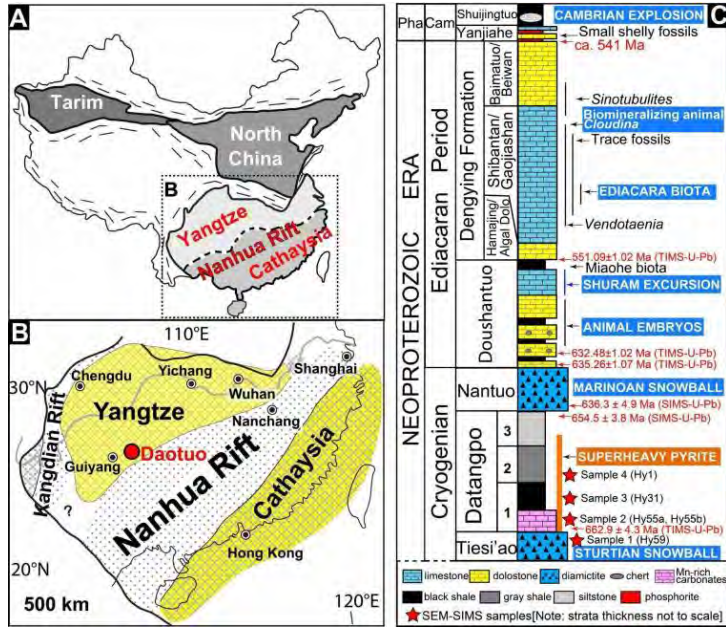


861

862 **Figure 1.** Compilation of published  $\delta^{34}\text{S}$  data measured from the Cryogenic post-glacial strata in China,  
863 UK, Namibia, and Australia. X axis represents  $\delta^{34}\text{S}$  values (V-CDT, ‰). Y axis represents different  
864 published data sets. (A) Individual data points of all the data sets. Numbers in parentheses representing  
865 the amount of data. (B) Box plots of corresponding data in A. Red line and black line within each box  
866 showing the mean value and the median value, respectively. Data sets 1 and 2 (blue) representing  
867  $\delta^{34}\text{S}_{\text{sulfate}}$  data measured from anhydrite and carbonate-associated sulfate (CAS), respectively. Data sets 3–  
868 19 (yellow in B) representing  $\delta^{34}\text{S}_{\text{pyrite}}$  data. Red dash line represents Cryogenic seawater  $\delta^{34}\text{S}_{\text{sulfate}}$  values  
869 based on data set 1. All plotted data were generated by conventional bulk analysis. Note that many  
870  $\delta^{34}\text{S}_{\text{pyrite}}$  data (up to +70‰) are much higher than the contemporaneous  $\delta^{34}\text{S}_{\text{sulfate}}$  value (ca. +26‰, red  
871 dash line), commonly known as superheavy pyrite signals (i.e.,  $\delta^{34}\text{S}_{\text{pyrite}} > \delta^{34}\text{S}_{\text{sulfate}}$ ). Data source: (1)  
872 Tapley Hill Formation (Adelaide Rift Fm), Australia (Gorjan et al., 2000); (2) Rasthof, Gruis, and  
873 Ombaatjie formations of the Otavi Group, Namibia (Hurtgen et al., 2002); (3–14) Datangpo Formation in  
874 South China, including localities at (3) Yangjiaping, Hunan Province (Li et al., 2012), (4) Tanganshan,  
875 Hunan Province (Liu et al., 2006), (5) Dawu mine, Songtao County, Guizhou Province (Zhou et al., 2007;  
876 Wu et al., 2016), (6) Xiangtan, Hunan Province (Li et al., 1999a; Liu et al., 2006), (7) Zhailanggou mine,  
877 Songtao County, Guizhou Province (Chen et al., 2008), (8) Yanglizhang mine, Songtao County, Guizhou  
878 Province (Zhou et al., 2007), (9) Minle mine, Huayuan County, Hunan Province (Tang, 1990; Li et al.,  
879 1999a; Tang and Liu, 1999; Feng et al., 2010; Li et al., 2012; Wu et al., 2016), (10) Lijiawan, Songtao  
880 County, Guizhou Province (Wang et al., 2016), (11) Xixibao mine, Songtao County, Guizhou Province  
881 (Zhang et al., 2013; Wang et al., 2016), (12) Gucheng, Hubei Province (Wu et al., 2016), (13) Datangpo  
882 mine, Songtao County, Guizhou Province (Li et al., 1999a; Zhou et al., 2007; Wu et al., 2016), (14)  
883 Daotuo mine, Songtao County, Guizhou Province (Zhu et al., 2013; Wang et al., 2016); (15) Tapley Hill  
884 Formation in the Adelaide Rift Complex, Australia (Gorjan et al., 2000); (16) Tapley Hill Formation in  
885 the Amadeus Basin, Australia (Gorjan et al., 2000); (17) Gobabis Member, Namibia (Gorjan et al., 2003);  
886 (18) Arena Formation, East Greenland (Scheller et al., 2018); (19) Bonahaven Dolomite Formation, UK  
887 (Parnell and Boyce, 2017). All the compiled data are available in the online [Appendix 1](#).

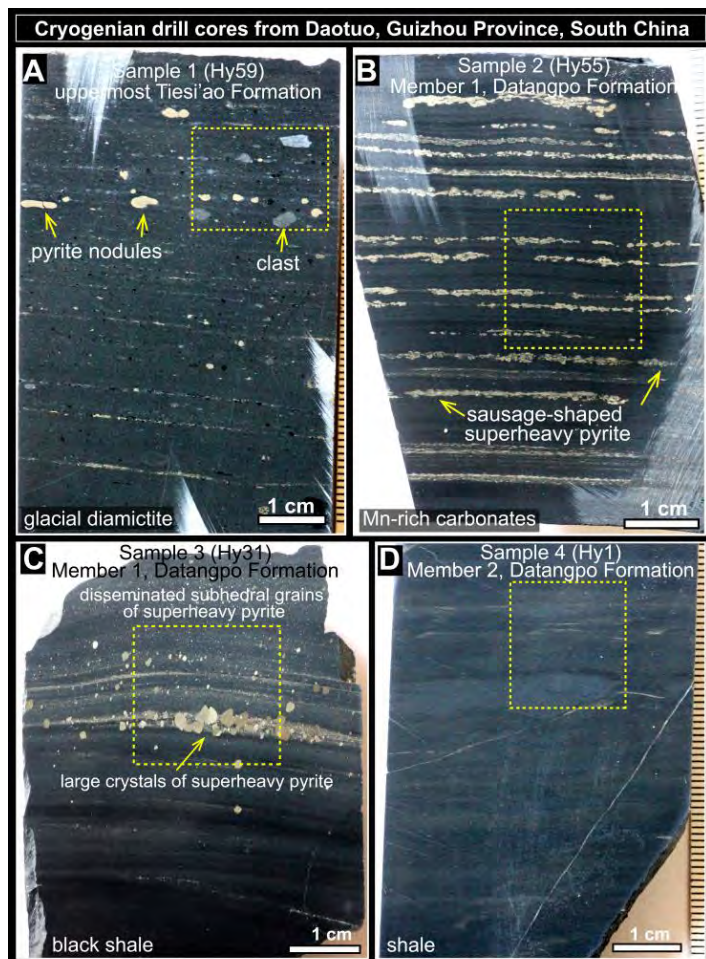
888

889



890

891 **Figure 2.** (A) Tectonic map of China. (B) Reconstructed Yangtze and Cathaysia blocks with the Nanhua  
 892 rift in between (Li et al., 1999b; Jiang et al., 2003; Wang and Li, 2003; Zhang et al., 2008). Red dot  
 893 indicates the location of the studied Daotuo mine at Songtao, eastern Guizhou Province. (C) Simplified  
 894 litho-, bio-, and chrono-stratigraphy of the Neoproterozoic strata in South China. Source of the lithology  
 895 and fossil record (Jiang et al., 2007; McFadden et al., 2008; Cai et al., 2010; Jiang et al., 2011; Chen et al.,  
 896 2013; Chen et al., 2014; Cui, 2015; Cui et al., 2016b; Cui et al., 2017). Source of the radiometric ages  
 897 (Zhou et al., 2004; Condon et al., 2005; Zhang et al., 2008; Schmitz, 2012; Chen et al., 2015). Superheavy  
 898 pyrite has been widely reported from the post-glacial Datangpo Formation (see text). Thickness is not to  
 899 scale. Cam = Cambrian; Pha = Phanerozoic.

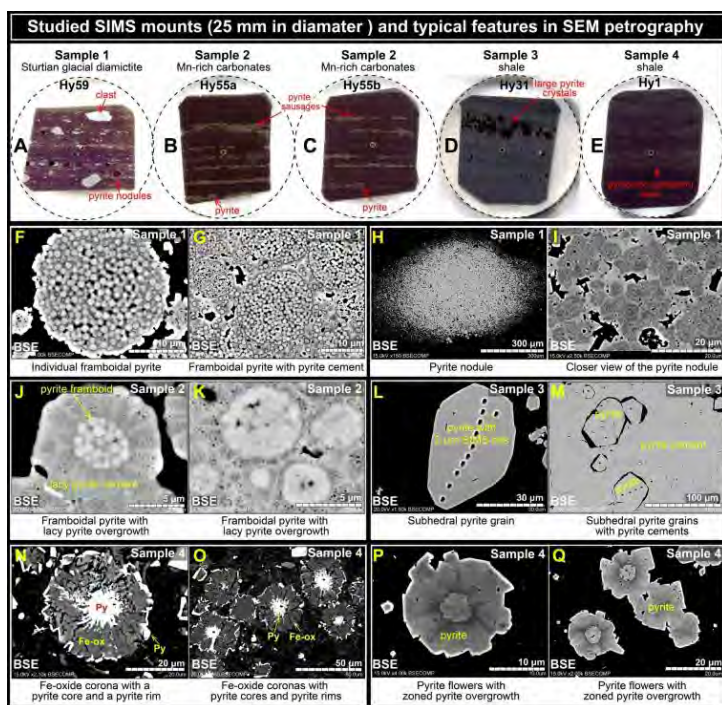


900

901 **Figure 3. (A–D)** Four drill core samples collected at Daotuo, Guizhou Province, South China. Marked  
902 zones of the surfaces were prepared as SIMS mounts for further studies. **A:** **Sample 1** (Hy59, glacial  
903 diamictite) from the uppermost Tiesi'ao Formation. **B:** **Sample 2** (Hy55, Mn-rich carbonates) from the  
904 Member 1 of the Datangpo Formation. **C:** **Sample 3** (Hy31, shale) from the Member 1 of the Datangpo  
905 Formation. **D:** **Sample 4** (Hy1, shale) from the Member 2 of the Datangpo Formation. All the drill cores  
906 are 4.5 cm in diameter.

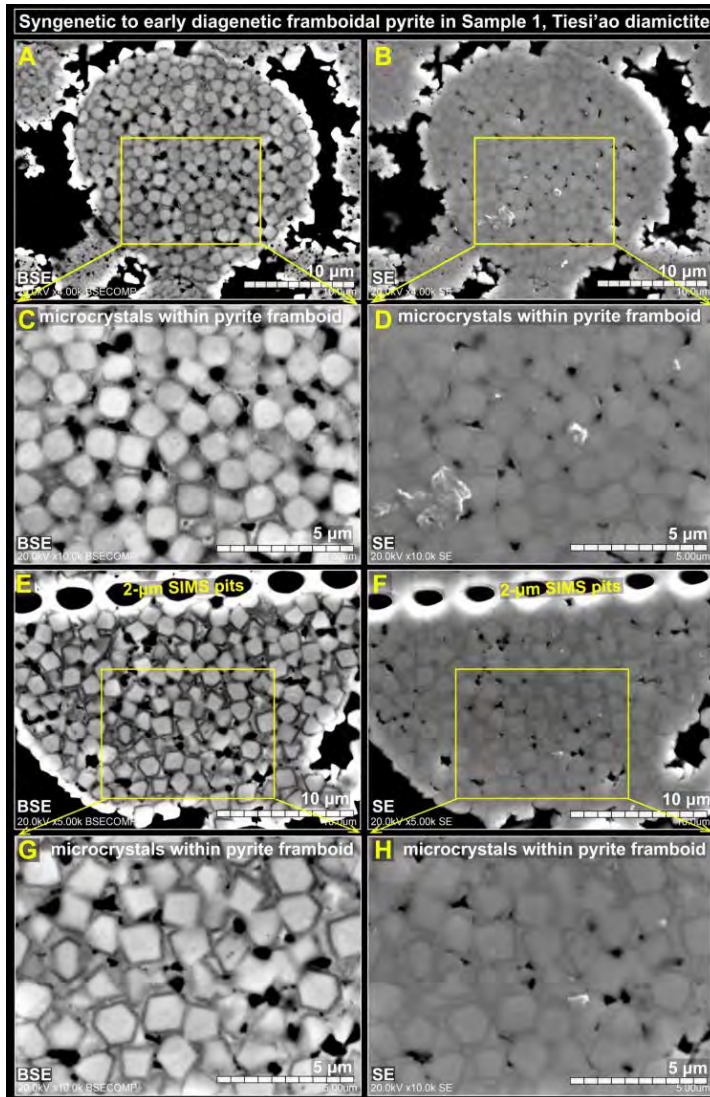
907

908



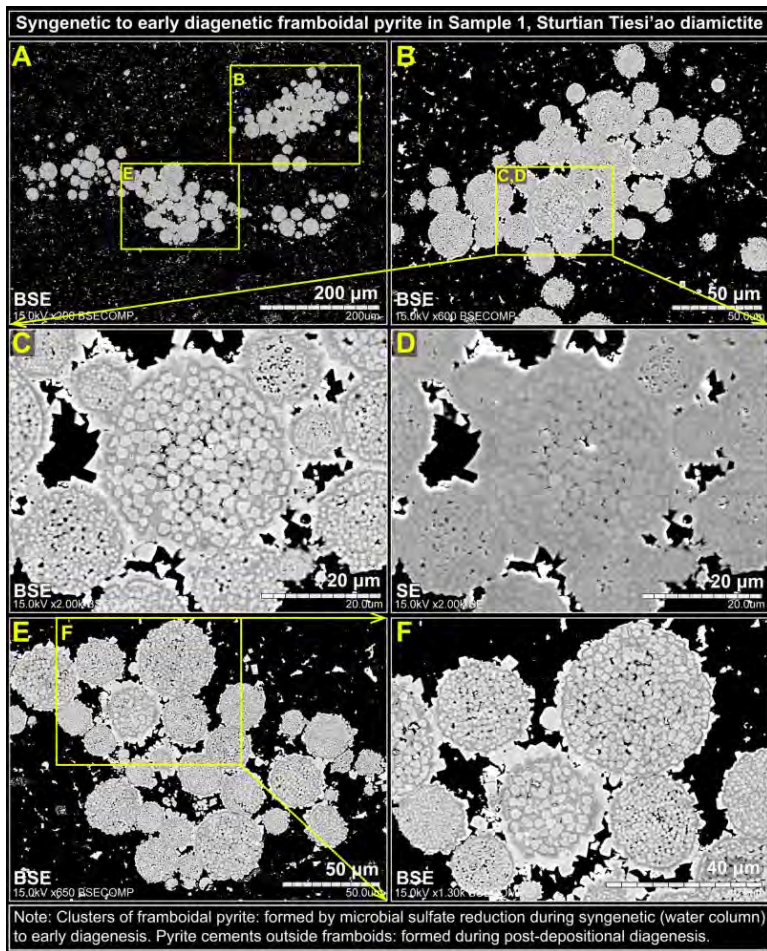
909

910 **Figure 4.** Studied SIMS mounts and typical petrographic features of each sample. (A–E) 25-mm-  
 911 diameter SIMS mounts with in-house pyrite standard UWPy-1 (marked as yellow circles) mounted in the  
 912 center of each mount. (F–Q) Typical features by SEM-BSE. F–I Sample 1 (Hy59); J–K Sample 2 (Hy55);  
 913 L–M Sample 3 (Hy31); N–Q Sample 4 (Hy1). (F) Individual pyrite framboid in **Sample 1**. (G)  
 914 Framboidal pyrite with pyrite cement in **Sample 1**. (H) A large pyrite nodule in **Sample 1**. (I) A magnified  
 915 view of the individual zoned pyrite crystals within the pyrite nodule in **Sample 1**. (J, K) Framboidal  
 916 pyrite with lacy pyrite overgrowth in **Sample 2**. (L) Subhedral pyrite grain in **Sample 3**. (M) Subhedral  
 917 pyrite grains with pyrite cements in **Sample 3**. (N, O) “Fe-oxide coronas” with pyrite cores and pyrite  
 918 rims. Py: pyrite; Fe-ox: Fe oxide. Small black spots in L, M and O showing SIMS pits. (P, Q) “Pyrite  
 919 flowers” in **Sample 4** showing framboidal pyrite cores and zoned pyrite overgrowth. Abbreviations: BSE  
 920 = backscattered electron; SE = secondary electron. For more detailed SEM images of the studied samples,  
 921 see online [Appendices 2–5](#).



922

923 **Figure 5.** SEM petrography of the pyrite framboids in [Sample 1](#). Images C–D and G–H showing  
924 magnified views of marked areas in A–B and E–F, respectively. Note that the pyrite microcrystals within  
925 the framboids are typically surrounded by darker rims (possibly rich in inclusion or porosity) and pyrite  
926 cements. Abbreviations: BSE = backscattered electron; SE = secondary electron. For more detailed SEM  
927 images of the studied samples, see online [Appendix 2](#).

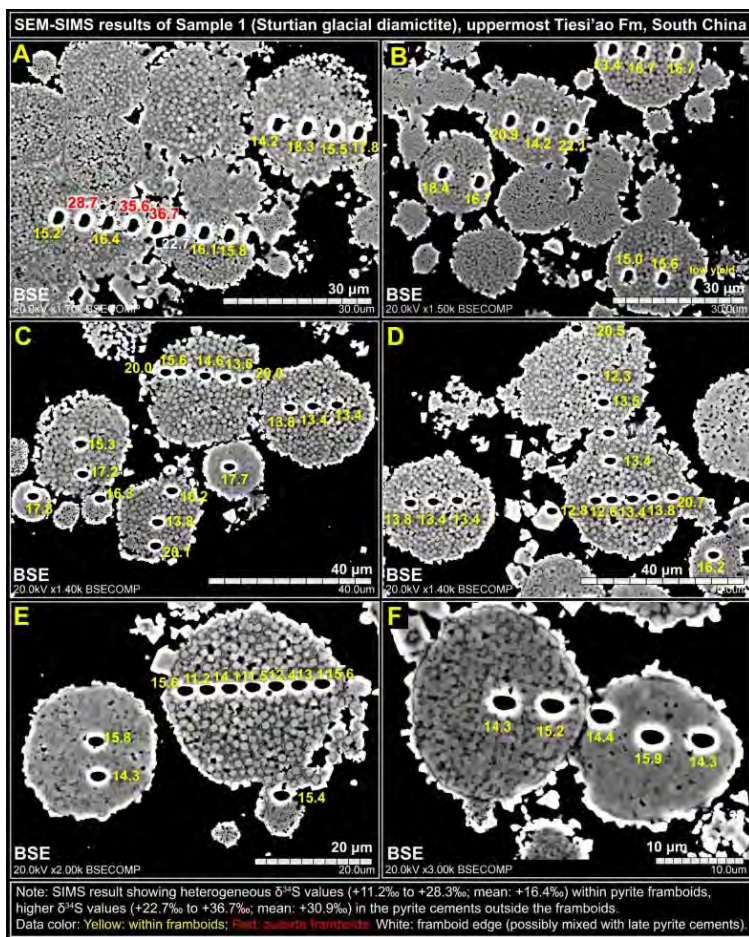


928

929 **Figure 6. (A–F)** SEM images showing clusters of framboidal pyrite in **Sample 1**. Magnified views are  
930 marked by yellow dash boxes. Note that many of the pyrite framboids are cemented by later-stage pyrite.  
931 Based on the petrography and  $\delta^{34}\text{S}$  evidence, the framboidal pyrite in Sample 1 is interpreted to be  
932 syngenetic to early diagenetic in origin. See the main text for further discussion. Abbreviations: BSE =  
933 backscattered electron; SE = secondary electron. For more detailed SEM images, see online [Appendix 2](#).

934

935

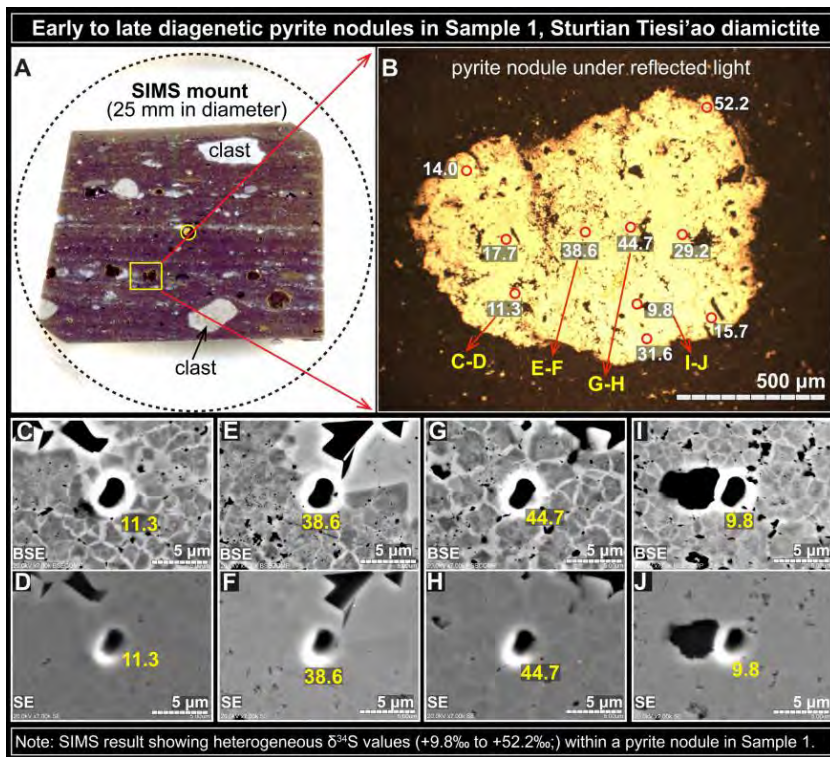


936

937 **Figure 7.** Backscattered electron (BSE) images and SIMS  $\delta^{34}\text{S}$  results of framboidal pyrite in **Sample 1**.  
938 SIMS  $\delta^{34}\text{S}$  data presented in different colors based on petrographic textures. Yellow: within framboids;  
939 Red, outside framboids; White: framboid edge. Detailed views of **image A** can be found in **Slides 25–32**  
940 of the online **Appendix 2**. Note that the  $\delta^{34}\text{S}$  data measured from the pyrite cements outside the framboids  
941 (red or white) are significantly higher than those measured within the pyrite framboids (yellow). For more  
942 detailed SEM-SIMS results of this sample, see online **Appendix 2**.

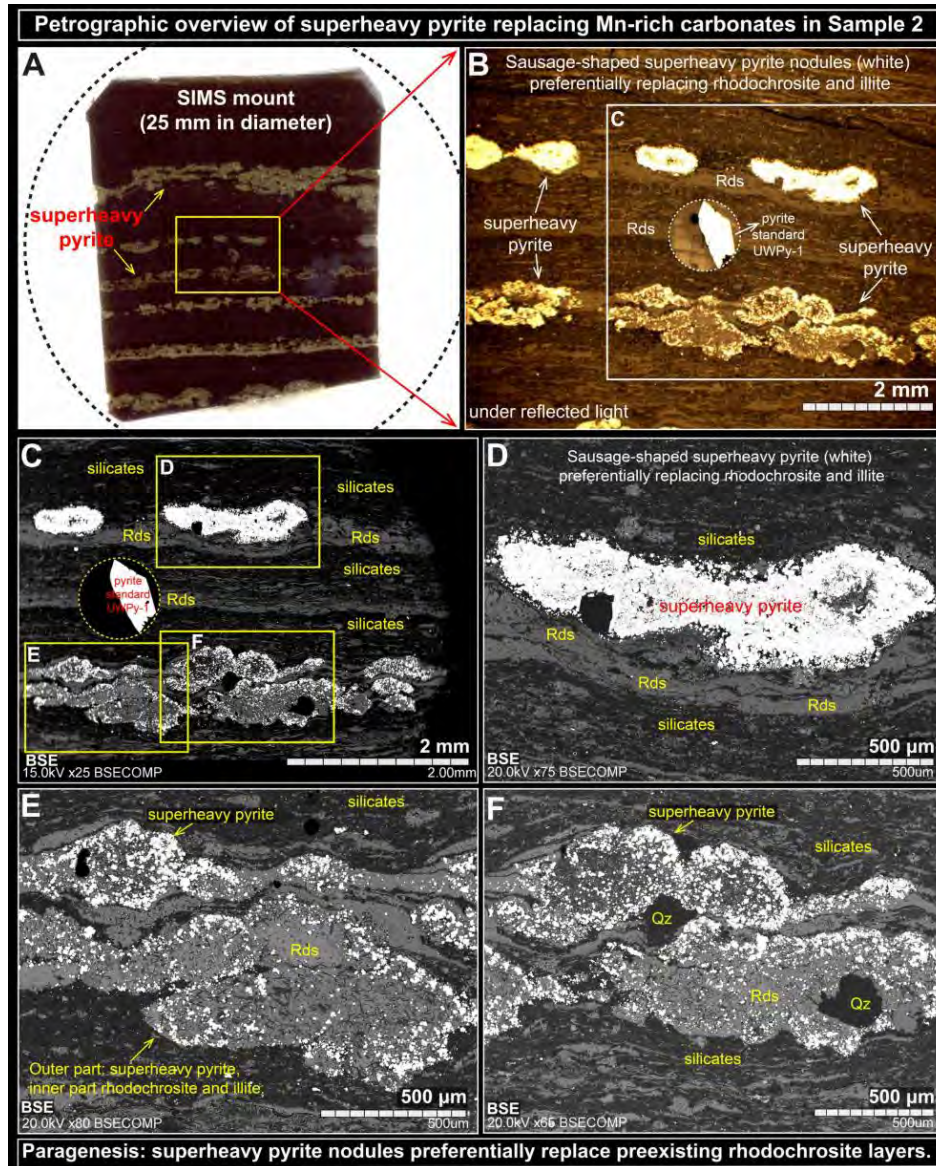
943

944



945

946 **Figure 8.** Pyrite nodules in [Sample 1](#). (A) 25-mm-diameter SIMS mount of Sample 1 with in-house pyrite  
947 standard UWPY-1 (marked as yellow circle) mounted in the center. (B) A studied pyrite nodule under  
948 reflected light. SIMS  $\delta^{34}\text{S}$  values showing heterogeneous values. Note that the symbols (red circles) are  
949 much larger than the actual SIMS spots (2  $\mu\text{m}$  in diameter). (C–D, E–F, G–H, I–J) Coupled BSE–SE  
950 images of the analyzed spots. The spots are all shown in the center. Note that the pyrite nodule is very  
951 heterogeneous under BSE, representing progressive pyrite mineralization during a spectrum of diagenesis.  
952 Abbreviations: BSE = backscattered electron; SE = secondary electron. For more detailed SEM-SIMS  
953 results of this sample, see online [Appendix 2](#).

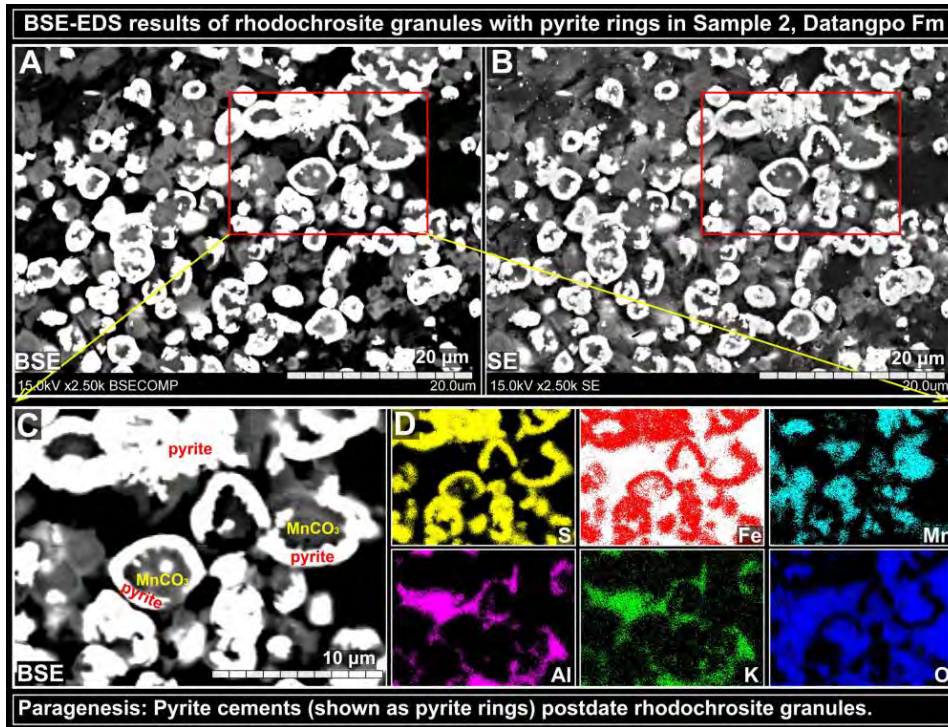


954

955 **Figure 9.** Petrographic observations of **Sample 2**. **(A)** SIMS mount of Sample 2 showing abundant  
956 sausage-shaped pyrite nodules within Mn-rich carbonates. **(B, C)** Sausage-shaped superheavy pyrite  
957 aggregates partially replacing rhodochrosite. Image **B** taken under reflected light; Image **C** taken with  
958 BSE. Note that some sausage-shaped textures have superheavy pyrite around margins and relict  
959 rhodochrosite in the center. **(D–F)** Magnified BSE views of the sausage-shaped textures. Note that  
960 superheavy pyrite in **E** and **F** is partially replacing the preexisting rhodochrosite (Rds) lamina, with  
961 superheavy pyrite concentrated at the margins and rhodochrosite in the core of the sausages. For more  
962 detailed petrographic images of this sample, see online [Appendix 3](#).

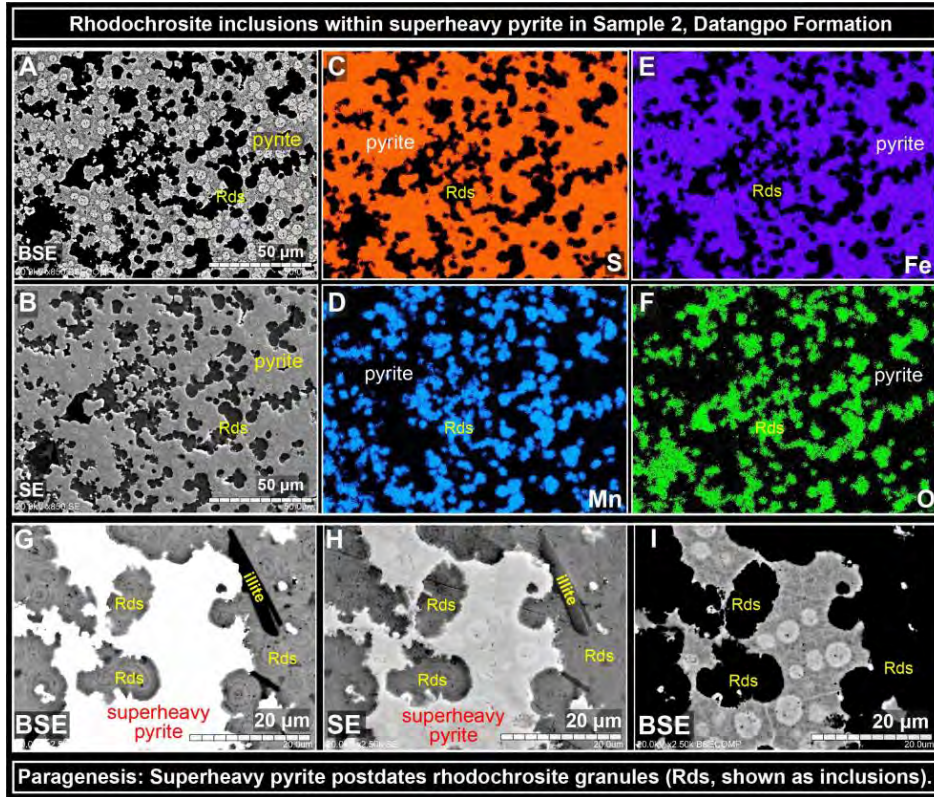
963

964



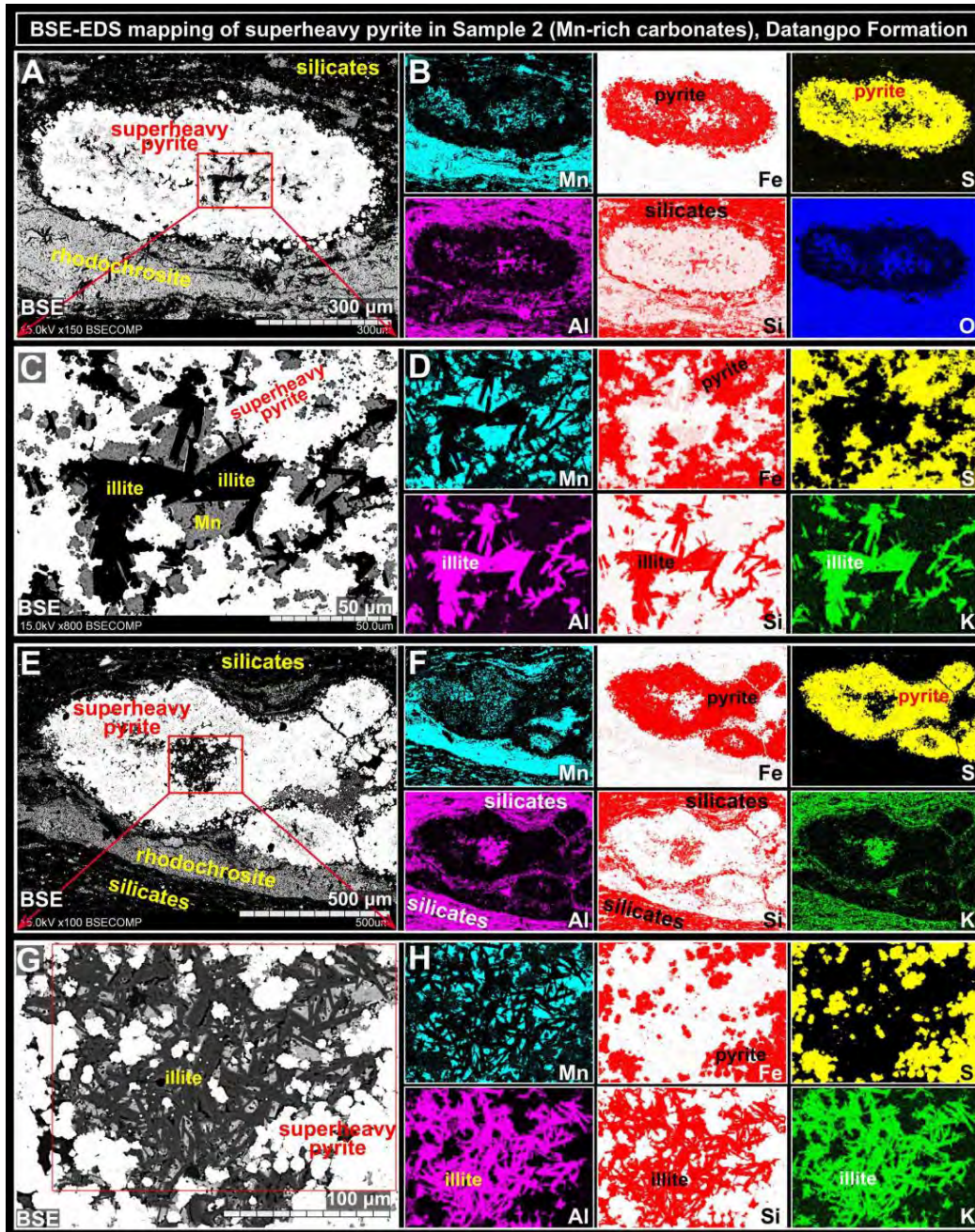
965

966 **Figure 10.** SEM-EDS results of rhodochrosite granules with pyrite rings in Sample 2. (A, B) Matched  
967 views under BSE and SE, respectively. (C) Magnified BSE view of marked zones in A and B. (D) ESD  
968 elemental mapping of the view in C. Black or white background colors in the EDS images represent zero  
969 detection. For more petrographic images of this sample, see online [Appendix 3](#). Abbreviations: BSE =  
970 backscattered electron; SE = secondary electron; EDS = Energy-Dispersive X-ray Spectrometry. For  
971 more petrographic images of this sample, see online [Appendix 3](#).

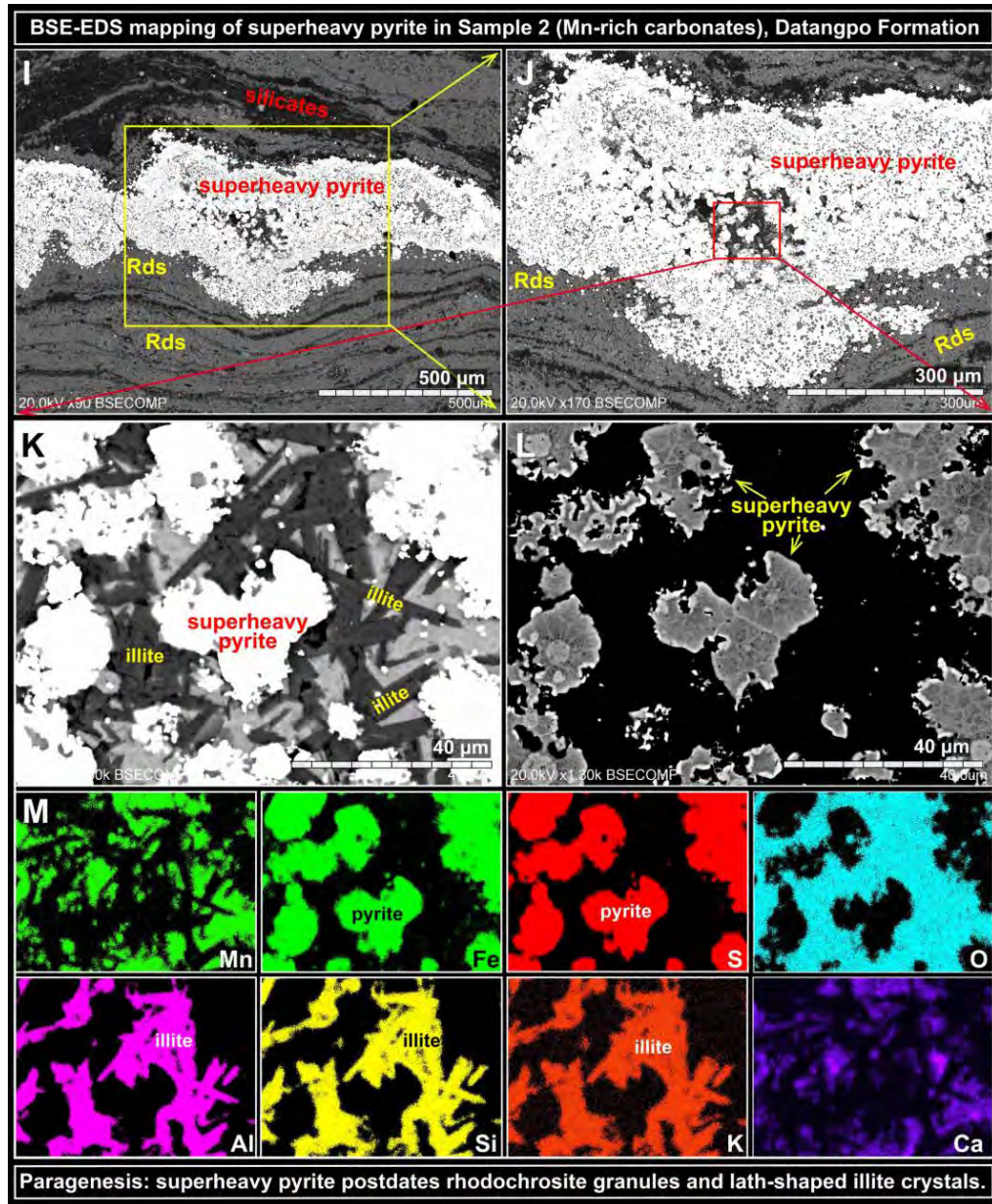


972

973 **Figure 11.** SEM-EDS views of rhodochrosite inclusions within the superheavy pyrite in [Sample 2](#). A–F  
974 and G–I showing matched views of SEM and elemental maps by EDS. Black background in EDS  
975 element maps represents zero detection. The BSE images of superheavy pyrite are made with decreased  
976 color contrast (A, I) to show heterogeneous textures with pyrite frambooids (brighter under BSE) and lacy  
977 pyrite overgrowths (darker under BSE). Note metasomatic corrosion textures and the massive  
978 rhodochrosite inclusions that are not yet replaced by superheavy pyrite, suggesting superheavy pyrite  
979 postdates rhodochrosite. Abbreviations: BSE = backscattered electron; SE = secondary electron. For more  
980 detailed SEM-EDS images of this sample, see online [Appendix 3](#).



981

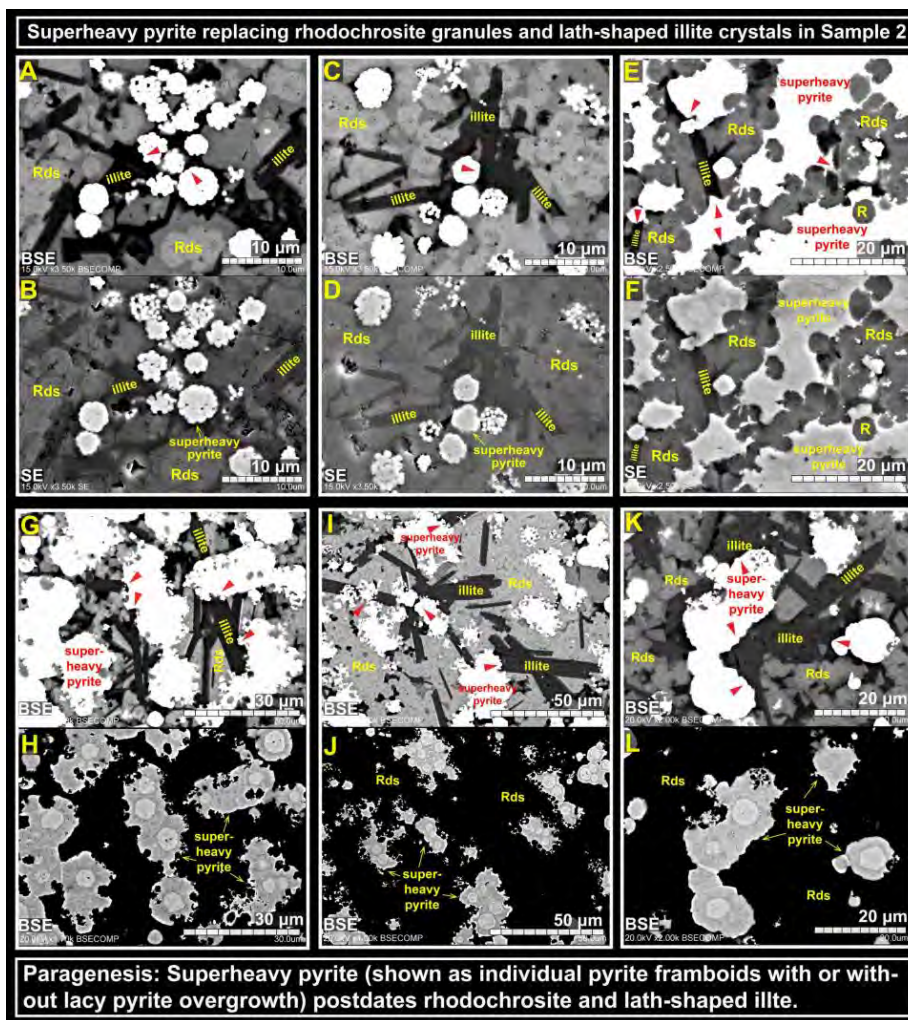


982

983 **Figure 12.** SEM-EDS results of superheavy pyrite in Sample 2. Images A–B, C–D, E–F, G–H, K/L–M  
984 showing pairs of matched views of BSE and EDS, respectively. Black or white background colors in EDS  
985 images represent zero detection. Abbreviations: BSE = backscattered electron; EDS = Energy-Dispersive  
986 X-ray Spectrometry. Note that superheavy pyrite in Sample 2 showing the replacement of preexisting  
987 rhodochrosite (Rds) and lath-shaped illite crystals. For more detailed SEM-EDS images of this sample,  
988 see online [Appendix 3](#).

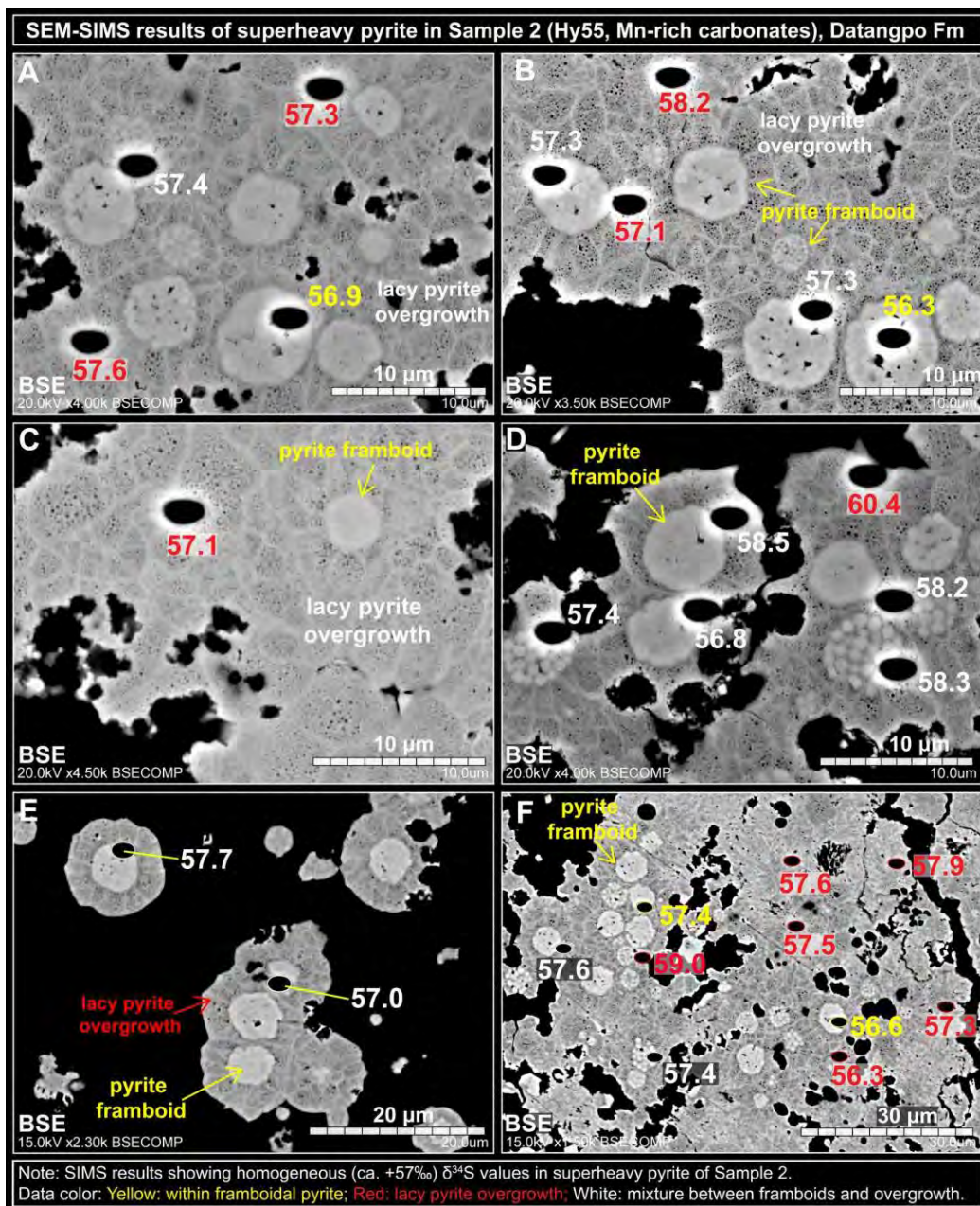
989

990



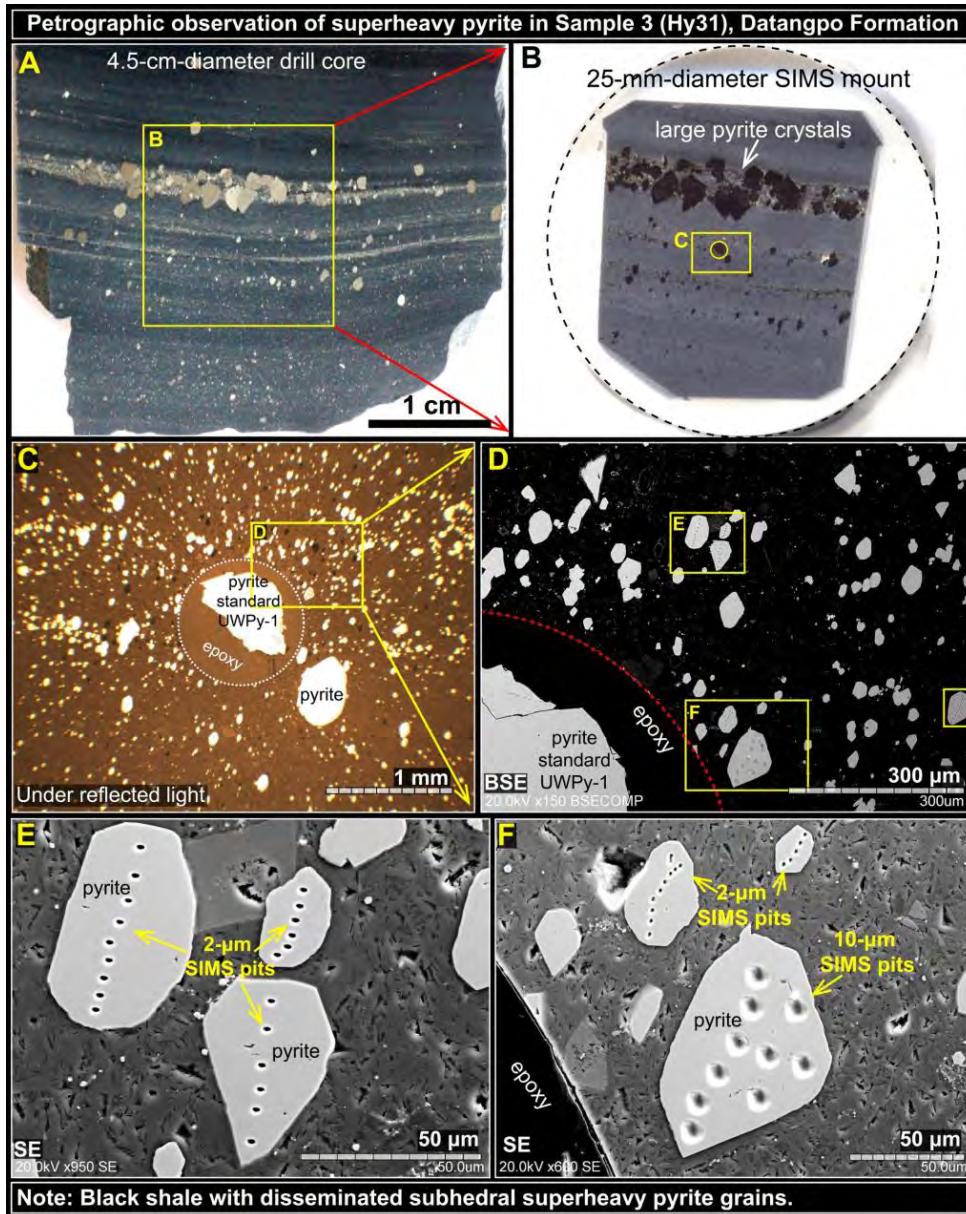
991

992 **Figure 13.** Backscattered electron (BSE) images of **Sample 2** showing the replacement (marked by red  
993 arrows) of preexisting rhodochrosite granules and lath-shaped illite crystals by superheavy pyrite. **A–B,**  
994 **C–D, E–F** showing individual pairs of BSE and SE images of the matched views, respectively. **G–H, I–J,**  
995 **K–L** showing BSE images of the same view but in different color contrast. (**A–D**) Individual pyrite  
996 framboids (without lacy pyrite overgrowth) replacing rhodochrosite and illite. (**E–L**) Pyrite framboids  
997 with lacy pyrite overgrowth replacing rhodochrosite and illite. Note the irregular pyrite boundary showing  
998 metasomatic corrosion textures. Rhodochrosite (Rds or R) inclusions in E and F also suggest that  
999 superheavy pyrite postdate rhodochrosite. Abbreviations used: BSE = backscattered electron; SE =  
1000 secondary electron. For more detailed SEM descriptions of this sample, see online [Appendix 3](#).



1001

1002 **Figure 14.** Backscattered electron (BSE) images with 2- $\mu\text{m}$  SIMS pits in superheavy pyrite in **Sample 2**.  
1003 SIMS  $\delta^{34}\text{S}$  data (‰ V-CDT) presented in different colors based on different textures. Yellow: within  
1004 framboids; Red, lacy pyrite overgrowth; White: mixture between pyrite framboids and pyrite overgrowth.  
1005 Superheavy pyrite in this sample shows heterogeneous textures with pyrite framboids (brighter under  
1006 BSE) and lacy pyrite overgrowth (darker under BSE) and metasomatic corrosion textures. Note the  
1007 remarkably homogeneous  $\delta^{34}\text{S}$  data regardless of heterogeneous petrographic textures. For more detailed  
1008 SEM-SIMS data of this sample, see online [Appendix 3](#).

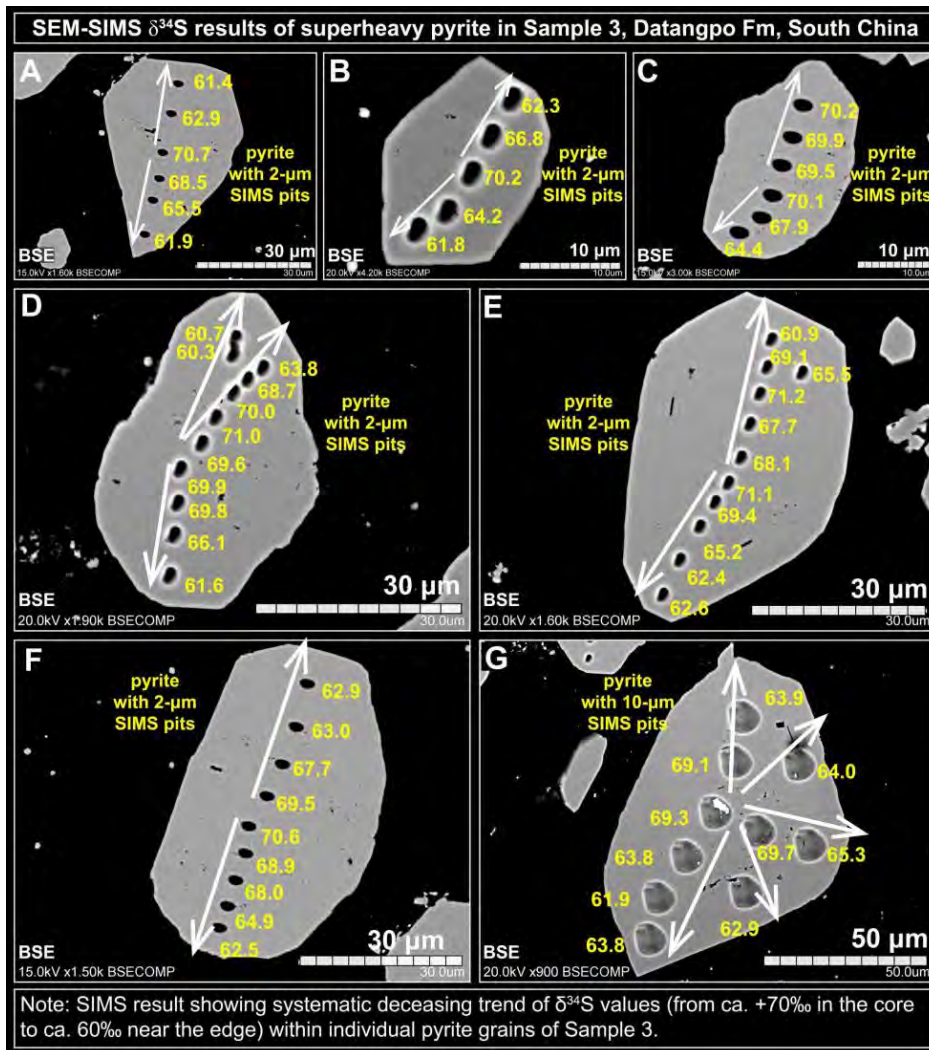


1009

1010 **Figure 15.** Petrographic observations of [Sample 3](#). (A) A drill core section of Sample 3 showing  
1011 abundant subhedral pyrite. (B) SIMS mount of Sample 3. (C) A magnified view of Sample 3 under  
1012 reflection light (RL) showing disseminated subhedral pyrite grains in shale. (D) BSE image of the marked  
1013 area in C. Analyzed pyrite grains in this study are marked by yellow dash boxes. Magnified views of  
1014 these marked pyrite grains can be found in [Figure 16](#) and the online [Appendix 4](#). (E, F) SE images of the  
1015 analyzed domains in D. SIMS pits of either 2 μm or 10 μm in diameter are shown on the analyzed pyrite  
1016 grains. Abbreviations: BSE = backscattered electron; SE = secondary electron. For more detailed SEM  
1017 descriptions of this sample, see online [Appendix 4](#).

1018

1019

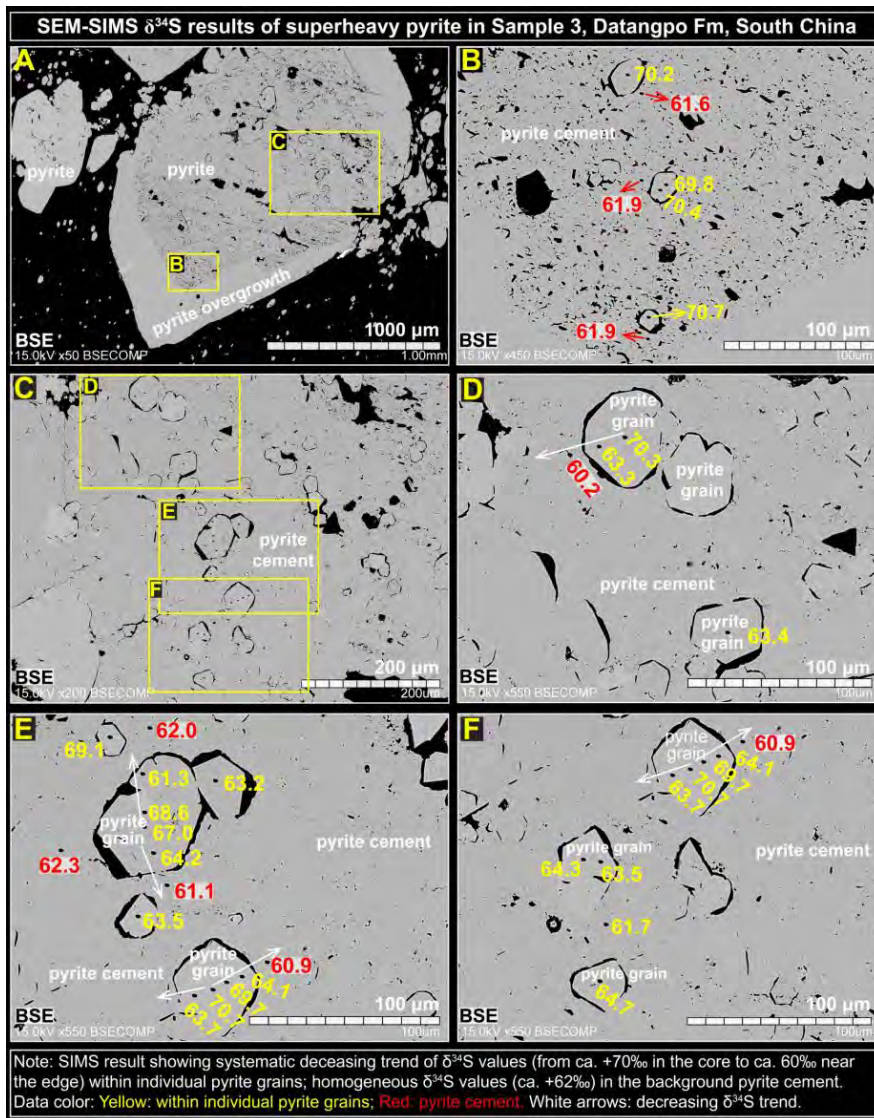


1020

1021 **Figure 16.** SEM-SIMS results of **Sample 3**. Note the consistent decreasing trend (white arrows) of  $\delta^{34}\text{S}$   
1022 values from the core (ca. +70‰) to the edge (ca. +61‰) of the individual pyrite grains. For more detailed  
1023 SEM-SIMS results of this sample, see online [Appendix 4](#).

1024

1025

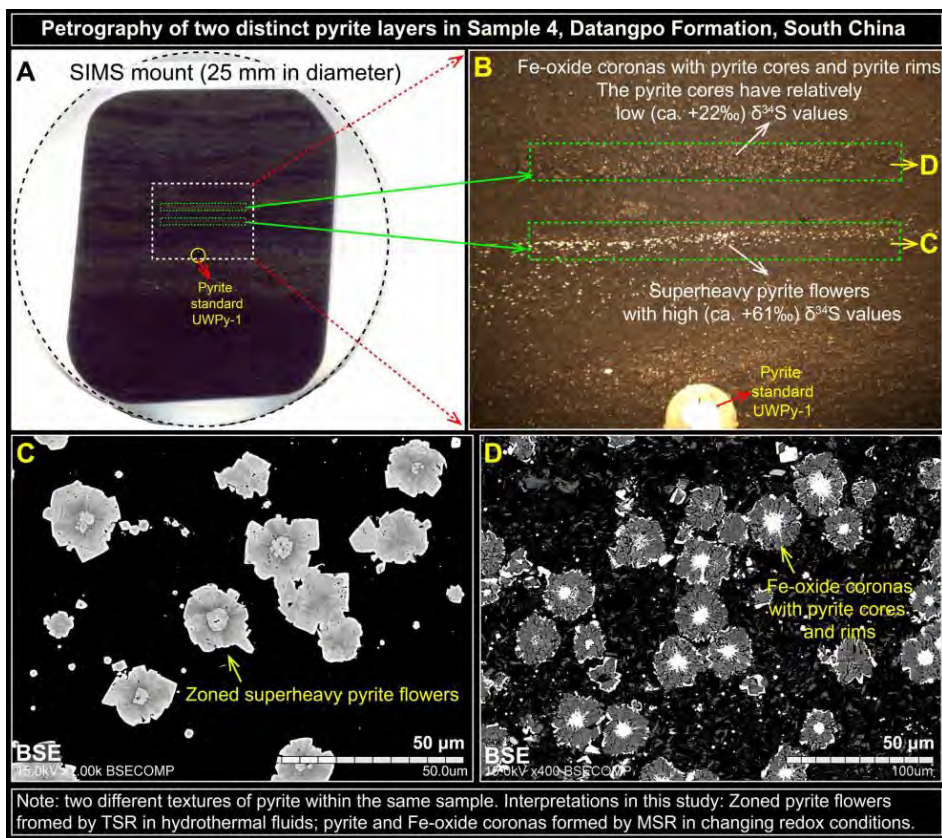


1026

1027 **Figure 17.** SEM-SIMS results of domains in **Sample 3**. (A) Large pyrite grains with multiple smaller  
1028 pyrite grains cemented inside. (B–F) Magnified views of marked areas in A and C showing individual  
1029 pyrite grains cemented by later-stage pyrite. SIMS  $\delta^{34}\text{S}$  data (‰ V-CDT) presented in different colors  
1030 based on different textures. Yellow: within individual pyrite grains; Red, later-stage pyrite cements.  
1031 White arrows showing consistent decreasing  $\delta^{34}\text{S}$  trends (ca. +70‰ to +60‰) from the core to the edge of  
1032 individual pyrite grains. For more detailed SEM-SIMS data of this sample, see online [Appendix 4](#).

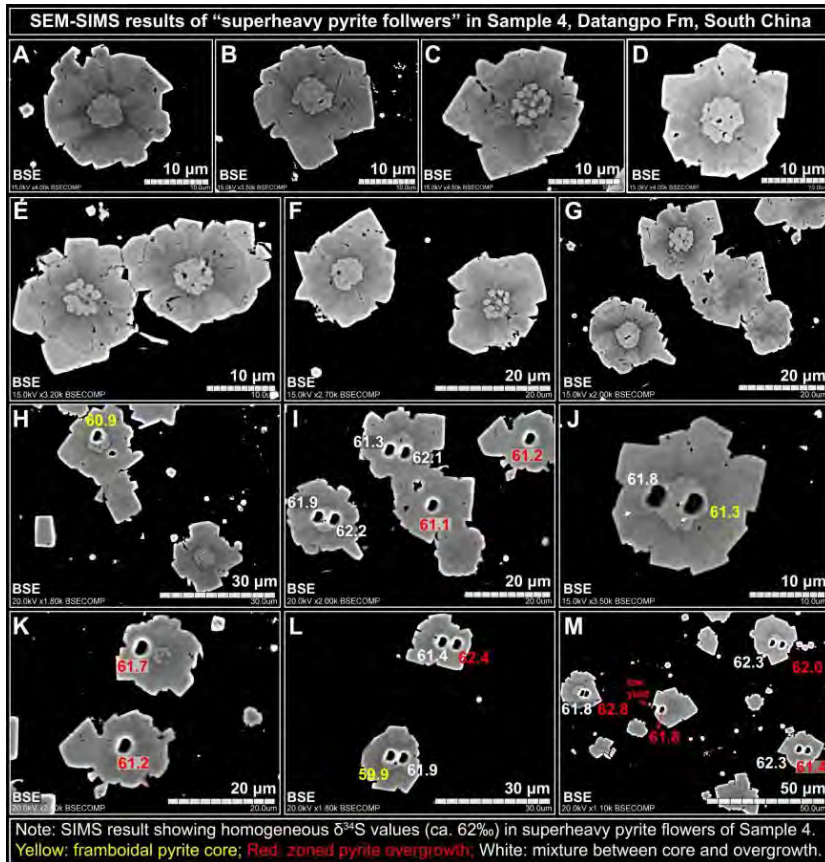
1033

1034



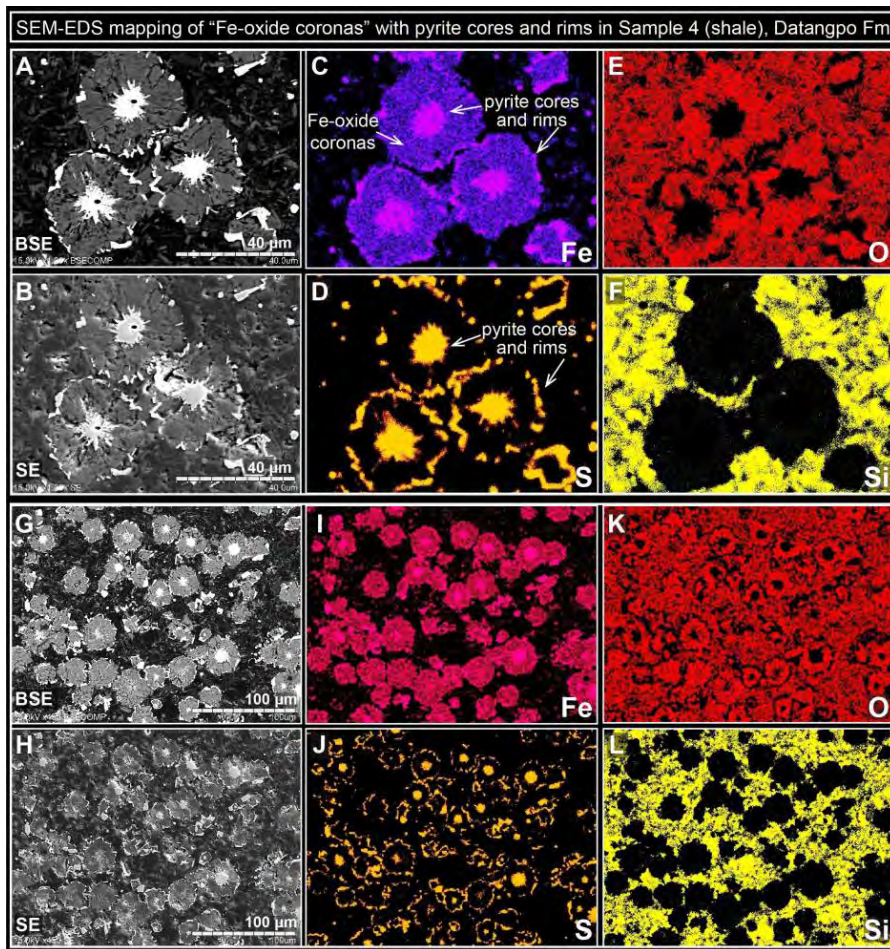
1035

1036 **Figure 18.** Petrographic observations of **Sample 4**. (A) SIMS mount of Sample 4. (B) A magnified view  
1037 of the marked area in A showing two distinct layers of pyrite. The SIMS  $\delta^{34}\text{S}$  data are also shown for  
1038 convenience. (C) A magnified view of pyrite in the lower layer. This layer is characterized by “zoned  
1039 pyrite flowers” with homogeneous and superheavy  $\delta^{34}\text{S}$  values. (D) A magnified view of pyrite in the  
1040 upper layer. This layer is characterized by “Fe-oxide coronas” with pyrite cores and pyrite rims. For more  
1041 detailed SEM-SIMS data from this sample, see online [Appendix 5](#).



1042

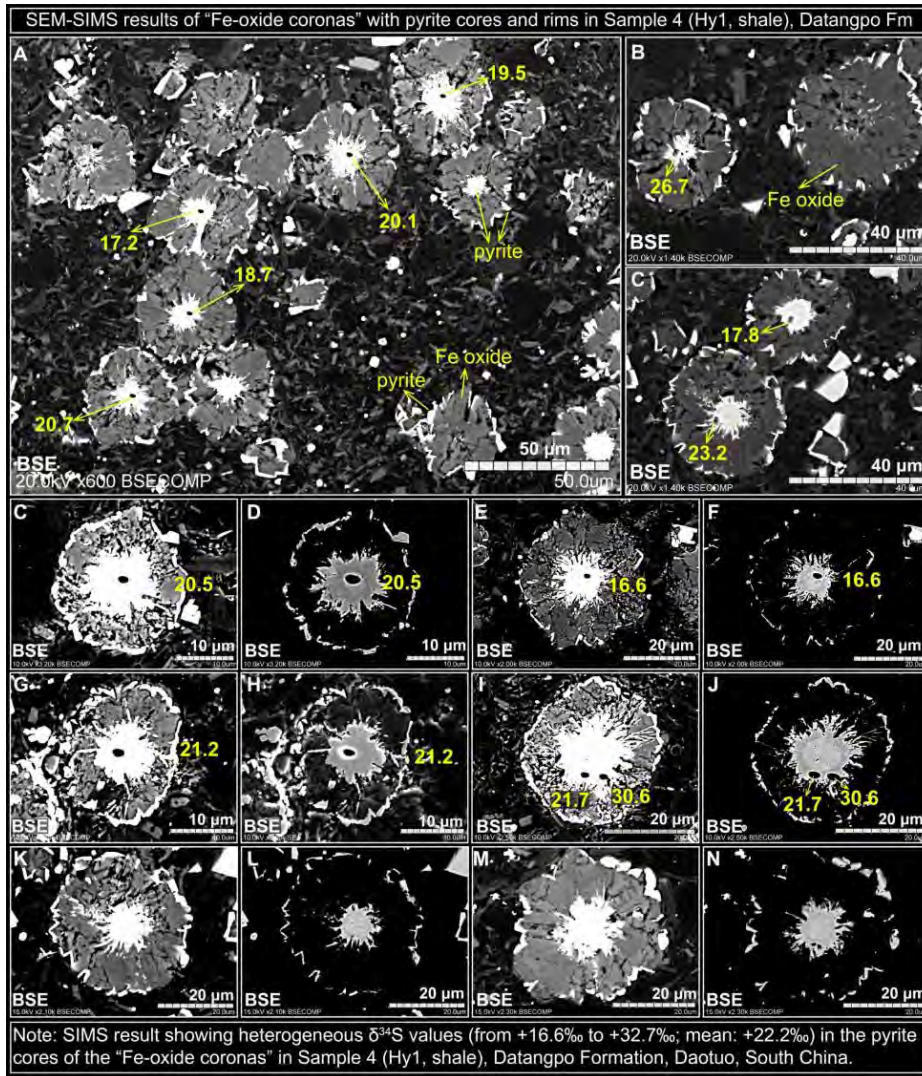
1043 **Figure 19.** Backscattered electron (BSE) images showing SIMS  $\delta^{34}\text{S}$  pits in "superheavy pyrite flowers"  
1044 in **Sample 4** (Hy1). The "superheavy pyrite flower" is characterized by a small framboidal pyrite core and  
1045 a zoned pyrite overgrowth. SIMS  $\delta^{34}\text{S}_{\text{pyrite}}$  values (‰ V-CDT) are presented in different colors based on  
1046 the textures. Yellow: within framboids; Red, zoned pyrite overgrowth; White: mixture between pyrite  
1047 framboids and pyrite overgrowth. Note that the  $\delta^{34}\text{S}$  data measured from zoned "superheavy pyrite  
1048 flowers" are remarkably homogeneous. For more detailed SEM-SIMS data from this sample, see online  
1049 [Appendix 5](#).



1050

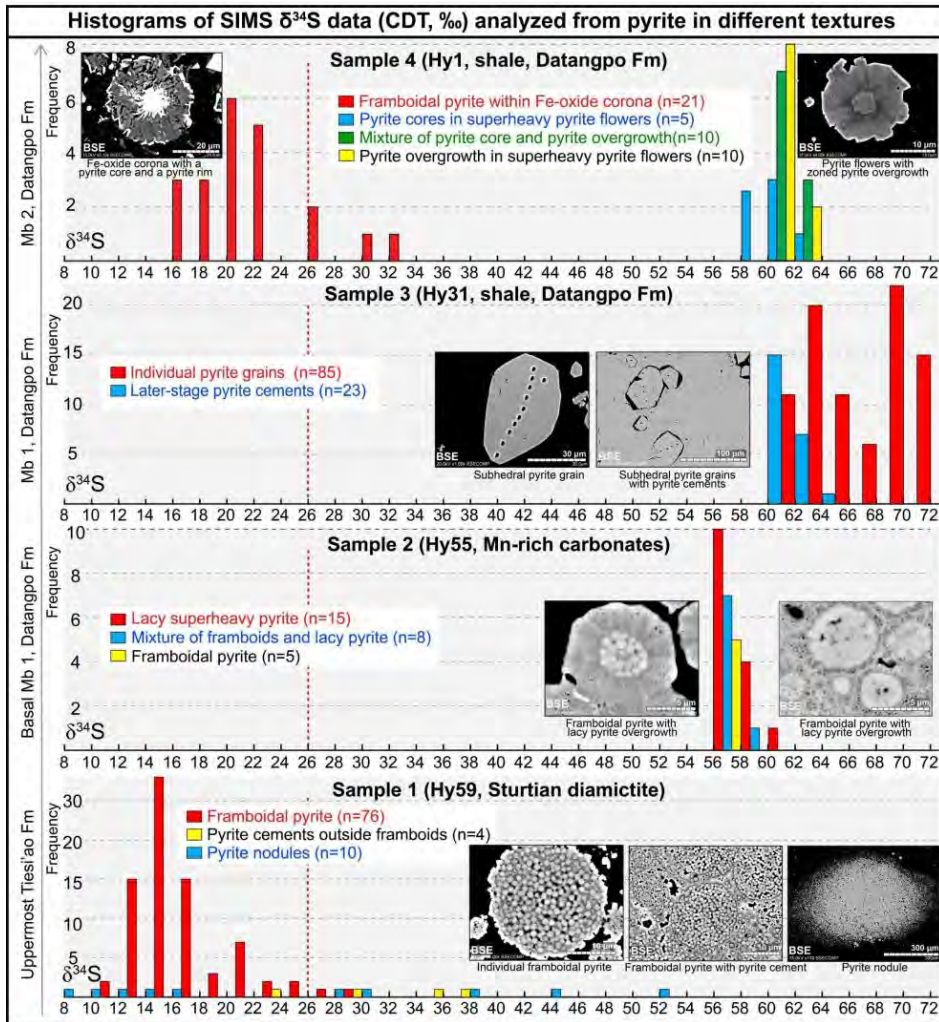
1051 **Figure 20.** A–F and G–L showing SEM-EDS images and chemical maps of Fe, O, S and Si of matched  
1052 views in Sample 4. Black background in EDS images represent zero detection. Abbreviations: BSE =  
1053 backscattered electron; EDS = Energy-Dispersive X-ray Spectrometry. For more detailed SEM-EDS  
1054 images from this sample, see online [Appendix 5](#).

1055



1056

1057 **Figure 21.** Backscattered electron (BSE) images showing SIMS  $\delta^{34}\text{S}$  pits in pyrite cores inside the Fe-  
 1058 oxide coronas in **Sample 4** (Hy1). The Fe-oxide corona surrounds a framboidal pyrite core with a fibrous  
 1059 surface (likely marcasite initially) and a thin pyrite rim. SIMS  $\delta^{34}\text{S}$  values measured from the pyrite cores  
 1060 range from ca. +16 to +33‰. For more detailed SEM-SIMS data of this sample, see online [Appendix 5](#).

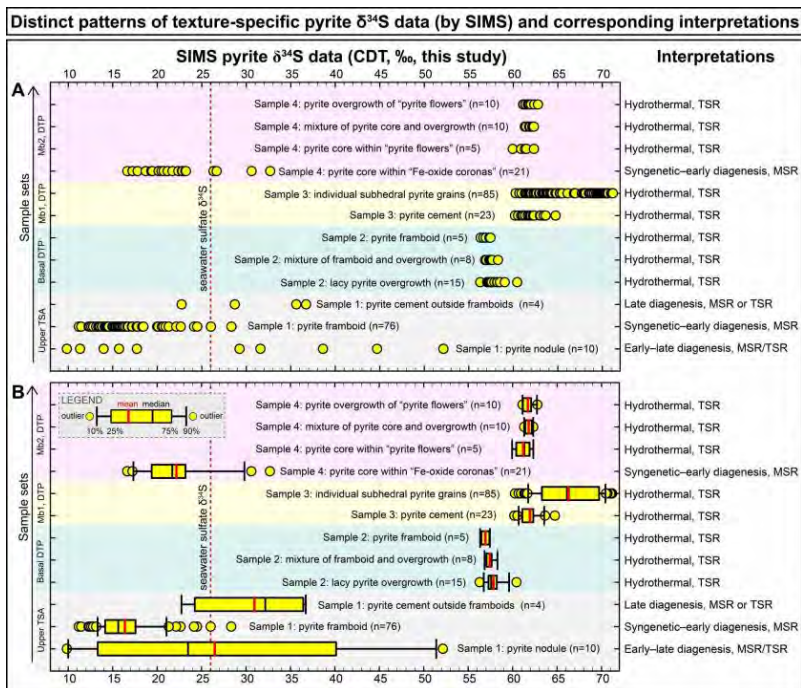


1061

1062 **Figure 22.** Histograms of the SIMS  $\delta^{34}\text{S}$  values measured in this study. Different pyrite textures showing  
1063 distinct ranges of  $\delta^{34}\text{S}$ . Red dash line representing the Cryogenian seawater  $\delta^{34}\text{S}_{\text{sulfate}}$  value based on  
1064 anhydrite analysis (Gorjan et al., 2000). Note the relatively large range of SIMS  $\delta^{34}\text{S}$  data measured from  
1065 **Sample 1**, homogeneous  $\delta^{34}\text{S}$  values measured from **Sample 2**, remarkably high  $\delta^{34}\text{S}$  values measured  
1066 from **Sample 3**, a notable bimodal distribution of the  $\delta^{34}\text{S}$  values measured from **Sample 4**. See the main  
1067 text for detailed discussion of these patterns and their interpreted origins. For corresponding petrographic  
1068 context of all the plotted data, see online [Appendices 2–5](#).

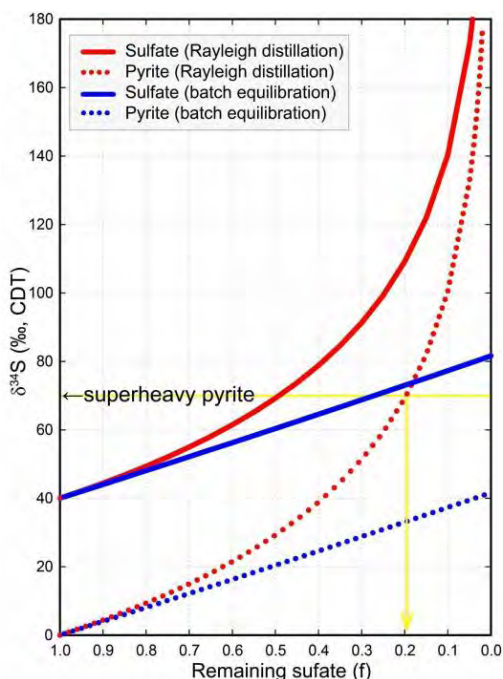
1069

1070



1071

1072 **Figure 23.** (A) Individual data points and (B) box plots of the SIMS  $\delta^{34}\text{S}$  values measured in this study.  
 1073 Numbers in parentheses representing the amount of data analyzed by SIMS in this study. Red dash line  
 1074 representing the Cryogenian seawater  $\delta^{34}\text{S}_{\text{sulfate}}$  value based on anhydrite analysis (Gorjan et al., 2000).  
 1075 Interpretations of the  $\delta^{34}\text{S}$  values of each data set listed on the right-hand side. Abbreviations: MSR:  
 1076 microbial sulfate reduction; TSR: thermochemical sulfate reduction. TSA: Tiesi'ao Formation; DTP:  
 1077 Datangpo Formation. For corresponding petrographic context of all the plotted data, see online  
 1078 [Appendices 2–6](#).



1079

1080 **Figure 24.** Models of  $\delta^{34}\text{S}_{\text{sulfate}}$  and  $\delta^{34}\text{S}_{\text{sulfide}}$  evolution during Rayleigh distillation (red) and batch  
1081 equilibration (blue) for precipitation of pyrite from sulfate (initial  $\delta^{34}\text{S} = 40\text{‰}$ ) in a system closed to  
1082 externally-derived fluids or other sources of sulfur. Equations used in calculation are from: (Canfield,  
1083 2001a; Canfield, 2001b). Yellow arrow shows the condition when  $\delta^{34}\text{S}_{\text{sulfide}}$  value achieves +70‰. See the  
1084 main text for detailed discussion.

1085

1086 **REFERENCES CITED**

- 1087 Alonso, A., Rodas, Bottrell, Raiswell, Velasco, and Mas. (1999) Pathways and distances of fluid flow  
1088 during low-grade metamorphism: evidence from pyrite deposits of the Cameros Basin, Spain.  
1089 *Journal of Metamorphic Geology*, 17, 339–348. <https://doi.org/10.1046/j.1525-1314.1999.00202.x>.
- 1090 Armstrong, J.T. (1988) Quantitative analysis of silicate and oxide minerals: comparison of Monte Carlo,  
1091 ZAF and phi-rho-z procedures. *Microbeam Analysis*, 23, 239–246.
- 1092 Basuki, N.I., Taylor, B.E., and Spooner, E.T.C. (2008) Sulfur isotope evidence for thermochemical  
1093 reduction of dissolved sulfate in Mississippi valley-type Zinc-Lead mineralization, Bongara area,  
1094 northern Peru. *Economic Geology*, 103, 783–799. <https://doi.org/10.2113/gsecongeo.103.4.783>.
- 1095 Bergmann, K.D., 2013, Constraints on the Carbon Cycle and Climate during the Early Evolution of  
1096 Animals: Ph.D. Dissertation, California Institute of Technology, Pasadena, California, 398 p.
- 1097 Berner, R.A. (1984) Sedimentary pyrite formation: An update. *Geochimica et Cosmochimica Acta*, 48,  
1098 605–615. [https://doi.org/10.1016/0016-7037\(84\)90089-9](https://doi.org/10.1016/0016-7037(84)90089-9).
- 1099 Berner, R.A. (1989) Biogeochemical cycles of carbon and sulfur and their effect on atmospheric oxygen  
1100 over phanerozoic time. *Palaeogeography, Palaeoclimatology, Palaeoecology*, 75, 97–122.  
1101 [https://doi.org/10.1016/0031-0182\(89\)90186-7](https://doi.org/10.1016/0031-0182(89)90186-7).
- 1102 Biehl, B.C., Reuning, L., Schoenherr, J., Lüders, V., and Kukla, P.A. (2016) Impacts of hydrothermal  
1103 dolomitization and thermochemical sulfate reduction on secondary porosity creation in deeply buried  
1104 carbonates: A case study from the Lower Saxony Basin, northwest Germany. *AAPG Bulletin*, 100,  
1105 597–621. <https://doi.org/10.1306/01141615055>.
- 1106 Bond, D.P.G., and Wignall, P.B. (2010) Pyrite framboid study of marine Permian–Triassic boundary  
1107 sections: A complex anoxic event and its relationship to contemporaneous mass extinction.  
1108 *Geological Society of America Bulletin*, 122, 1265–1279. <https://doi.org/10.1130/b30042.1>.
- 1109 Borowski, W.S., Hoehler, T.M., Alperin, M.J., Rodriguez, N.M., and Paull, C.K. (2000) Significance of  
1110 anaerobic methane oxidation in methane-rich sediments overlying the Blake Ridge gas hydrates. In  
1111 C.K. Paull, R. Matsumoto, P.J. Wallace, and W.P. Dillon, Eds. *Proceedings of the Ocean Drilling  
1112 Program, Scientific Results*, 164, p. 87–99.
- 1113 Böttcher, M.E. (2011) Sulfur Isotopes. In J. Reitner, and V. Thiel, Eds. *Encyclopedia of Geobiology*, p.  
1114 864–866. Springer Netherlands.
- 1115 Böttcher, M.E., Smock, A.M., and Cypionka, H. (1998) Sulfur isotope fractionation during experimental  
1116 precipitation of iron(II) and manganese(II) sulfide at room temperature. *Chemical Geology*, 146,  
1117 127–134. [https://doi.org/10.1016/S0009-2541\(98\)00004-7](https://doi.org/10.1016/S0009-2541(98)00004-7).
- 1118 Bowles, M.W., Mogollón, J.M., Kasten, S., Zabel, M., and Hinrichs, K.-U. (2014) Global rates of marine  
1119 sulfate reduction and implications for sub-sea-floor metabolic activities. *Science*, 344, 889–891.  
1120 <https://doi.org/10.1126/science.1249213>.
- 1121 Bradley, A.S., Leavitt, W.D., Schmidt, M., Knoll, A.H., Girguis, P.R., and Johnston, D.T. (2016) Patterns  
1122 of sulfur isotope fractionation during microbial sulfate reduction. *Geobiology*, 14, 91–101.  
1123 <https://doi.org/10.1111/gbi.12149>.
- 1124 Cai, C., Hu, G., Li, H., Jiang, L., He, W., Zhang, B., Jia, L., and Wang, T. (2015) Origins and fates of  $\text{H}_2\text{S}$   
1125 in the Cambrian and Ordovician in Tazhong area: Evidence from sulfur isotopes, fluid inclusions and  
1126 production data. *Marine and Petroleum Geology*, 67, 408–418.  
1127 <https://doi.org/10.1016/j.marpetgeo.2015.05.007>.

- 1128 Cai, C., Hu, W., and Worden, R.H. (2001) Thermochemical sulphate reduction in Cambro–Ordovician  
1129 carbonates in Central Tarim. *Marine and Petroleum Geology*, 18, 729–741.  
1130 [https://doi.org/10.1016/S0264-8172\(01\)00028-9](https://doi.org/10.1016/S0264-8172(01)00028-9).
- 1131 Cai, C., Worden, R.H., Bottrell, S.H., Wang, L., and Yang, C. (2003) Thermochemical sulphate reduction  
1132 and the generation of hydrogen sulphide and thiols (mercaptans) in Triassic carbonate reservoirs  
1133 from the Sichuan Basin, China. *Chemical Geology*, 202, 39–57. [https://doi.org/10.1016/S0009-  
1134 2541\(03\)00209-2](https://doi.org/10.1016/S0009-2541(03)00209-2).
- 1135 Cai, C., Xie, Z., Worden, R.H., Hu, G., Wang, L., and He, H. (2004) Methane-dominated thermochemical  
1136 sulphate reduction in the Triassic Feixianguan Formation East Sichuan Basin, China: towards  
1137 prediction of fatal H<sub>2</sub>S concentrations. *Marine and Petroleum Geology*, 21, 1265–1279.  
1138 <https://doi.org/10.1016/j.marpetgeo.2004.09.003>.
- 1139 Cai, Y., Hua, H., Xiao, S., Schiffbauer, J.D., and Li, P. (2010) Biostratigraphy of the late Ediacaran  
1140 pyritized Gaojiashan Lagerstätte from southern Shaanxi, South China: Importance of event deposits.  
1141 *PALAIOS*, 25, 487–506. <https://doi.org/10.2110/palo.2009.p09-133r>.
- 1142 Calver, C.R., Crowley, J.L., Wingate, M.T.D., Evans, D.A.D., Raub, T.D., and Schmitz, M.D. (2013)  
1143 Globally synchronous Marinoan deglaciation indicated by U–Pb geochronology of the Cottons  
1144 Breccia, Tasmania, Australia. *Geology*, 41, 1127–1130. <https://doi.org/10.1130/g34568.1>.
- 1145 Canfield, D.E. (2001a) Biogeochemistry of Sulfur Isotopes. In J.W. Valley, and D. Cole, Eds. *Stable  
1146 Isotope Geochemistry, Reviews in Mineralogy and Geochemistry*, 43, p. 607–636. Mineralogical  
1147 Society of America.
- 1148 Canfield, D.E. (2001b) Isotope fractionation by natural populations of sulfate-reducing bacteria.  
1149 *Geochimica et Cosmochimica Acta*, 65, 1117–1124. [https://doi.org/10.1016/S0016-7037\(00\)00584-6](https://doi.org/10.1016/S0016-7037(00)00584-6).
- 1150 Canfield, D.E. (2004) The evolution of the Earth surface sulfur reservoir. *American Journal of Science*,  
1151 304, 839–861. <https://doi.org/10.2475/ajs.304.10.839>.
- 1152 Canfield, D.E., and Farquhar, J. (2012) The Global Sulfur Cycle. In A.H. Knoll, D.E. Canfield, and K.O.  
1153 Konhauser, Eds. *Fundamentals of Geobiology*, p. 49–64. John Wiley & Sons, Ltd, Oxford, UK.
- 1154 Canfield, D.E., Farquhar, J., and Zerkle, A.L. (2010) High isotope fractionations during sulfate reduction  
1155 in a low-sulfate euxinic ocean analog. *Geology*, 38, 415–418. <https://doi.org/10.1130/g30723.1>.
- 1156 Canfield, D.E., and Teske, A. (1996) Late Proterozoic rise in atmospheric oxygen concentration inferred  
1157 from phylogenetic and sulphur-isotope studies. *Nature*, 382, 127–132.  
1158 <https://doi.org/10.1038/382127a0>.
- 1159 Canfield, D.E., and Thamdrup, B. (1994) The production of <sup>34</sup>S-depleted sulfide during bacterial  
1160 disproportionation of elemental sulfur. *Science*, 266, 1973–1975.  
1161 <https://doi.org/10.1126/science.11540246>.
- 1162 Cao, H., Kaufman, A.J., Shan, X., Cui, H., and Zhang, G. (2016) Sulfur isotope constraints on marine  
1163 transgression in the lacustrine Upper Cretaceous Songliao Basin, northeastern China.  
1164 *Palaeogeography, Palaeoclimatology, Palaeoecology*, 451, 152–163.  
1165 <https://doi.org/10.1016/j.palaeo.2016.02.041>.
- 1166 Chambers, L.A., Trudinger, P.A., Smith, J.W., and Burns, M.S. (1975) Fractionation of sulfur isotopes by  
1167 continuous cultures of *Desulfovibrio desulfuricans*. *Canadian Journal of Microbiology*, 21, 1602–  
1168 1607. <https://doi.org/10.1139/m75-234>.
- 1169 Chen, D., and Chen, X. (1992) Geological and geochemical characteristics of Songtan hydrothermal  
1170 sedimentary manganese deposits, Guizhou. *Acta Sedimentologica Sinica*, 10, 35–43 (in Chinese with  
1171 English abstract).
- 1172 Chen, D., Zhou, X., Fu, Y., Wang, J., and Yan, D. (2015) New U–Pb zircon ages of the Ediacaran–  
1173 Cambrian boundary strata in South China. *Terra Nova*, 27, 62–68. <https://doi.org/10.1111/ter.12134>.
- 1174 Chen, X., Li, D., Ling, H.-F., and Jiang, S.-Y. (2008) Carbon and sulfur isotopic compositions of basal  
1175 Datangpo Formation, northeastern Guizhou, South China: Implications for depositional environment.  
1176 *Progress in Natural Science*, 18, 421–429. <https://doi.org/10.1016/j.pnsc.2007.10.008>.

- 1177 Chen, Z., Zhou, C., Meyer, M., Xiang, K., Schiffbauer, J.D., Yuan, X., and Xiao, S. (2013) Trace fossil  
1178 evidence for Ediacaran bilaterian animals with complex behaviors. *Precambrian Research*, 224, 690–  
1179 701. <https://doi.org/10.1016/j.precamres.2012.11.004>.
- 1180 Chen, Z., Zhou, C., Xiao, S., Wang, W., Guan, C., Hua, H., and Yuan, X. (2014) New Ediacara fossils  
1181 preserved in marine limestone and their ecological implications. *Scientific Reports*, 4, 4180.  
1182 <https://doi.org/10.1038/srep04180>.
- 1183 Chu, X., Li, R., and Ohmoto, H. (1998) Sulfur isotope geochemistry of the late Proterozoic in Southern  
1184 China. *Chinese Science Bulletin*, 43, Supplement 1, 27–27. <https://doi.org/10.1007/bf02891401>.
- 1185 Chu, X., Li, R., Zhang, T., and Zhang, Q. (2001) Implication of ultra-high  $\delta^{34}\text{S}$  values of pyrite in  
1186 manganese mineralization beds of Datangpo stage. *Bulletin of Mineralogy, Petrology and*  
1187 *Geochemistry*, 20, 320–322 (in Chinese with English abstract).
- 1188 Chu, X., Zhang, Q., Zhang, T., and Feng, L. (2003) Sulfur and carbon isotopic variations in  
1189 Neoproterozoic sedimentary rocks from southern China. *Progress in Natural Science*, 13, 875–880.  
1190 <https://doi.org/10.1080/10020070312331344580>.
- 1191 Claypool, G.E. (2004) Ventilation of marine sediments indicated by depth profiles of pore water sulfate  
1192 and  $\delta^{34}\text{S}$ . In R.J. Hill, J. Leventhal, Z. Aizenshtat, M.J. Baedeker, G. Claypool, R. Eganhouse, M.  
1193 Goldhaber, and K. Peters, Eds. *The Geochemical Society Special Publications*, 9, p. 59–65. Elsevier.
- 1194 Condon, D., Zhu, M., Bowring, S., Wang, W., Yang, A., and Jin, Y. (2005) U–Pb ages from the  
1195 Neoproterozoic Doushantuo Formation, China. *Science*, 308, 95–98.  
1196 <https://doi.org/10.1126/science.1107765>.
- 1197 Cooke, D.R., Bull, S.W., Large, R.R., and McGoldrick, P.J. (2000) The importance of oxidized brines for  
1198 the formation of Australian Proterozoic stratiform sediment-hosted Pb-Zn (Sedex) deposits.  
1199 *Economic Geology*, 95, 1–18. <https://doi.org/10.2113/gsecongeo.95.1.1>.
- 1200 Crowe, S.A., Paris, G., Katsev, S., Jones, C., Kim, S.-T., Zerkle, A.L., Nomosatryo, S., Fowle, D.A.,  
1201 Adkins, J.F., and Sessions, A.L. (2014) Sulfate was a trace constituent of Archean seawater. *Science*,  
1202 346, 735–739. <https://doi.org/10.1126/science.1258966>.
- 1203 Cui, H., 2015, Authigenesis, Biomineralization, and Carbon–Sulfur Cycling in the Ediacaran Ocean Ph.D.  
1204 Dissertation, University of Maryland, College Park, Maryland, USA, 181 p.
- 1205 Cui, H., Grazhdankin, D.V., Xiao, S., Peek, S., Rogov, V.I., Bykova, N.V., Sievers, N.E., Liu, X.-M., and  
1206 Kaufman, A.J. (2016a) Redox-dependent distribution of early macro-organisms: Evidence from the  
1207 terminal Ediacaran Khatyspyt Formation in Arctic Siberia. *Palaeogeography, Palaeoclimatology,*  
1208 *Palaeoecology*, 461, 122–139. <https://doi.org/10.1016/j.palaeo.2016.08.015>.
- 1209 Cui, H., Kaufman, A.J., Xiao, S., Peek, S., Cao, H., Min, X., Cai, Y., Siegel, Z., Liu, X.M., Peng, Y.,  
1210 Schiffbauer, J.D., and Martin, A.J. (2016b) Environmental context for the terminal Ediacaran  
1211 biomineralization of animals. *Geobiology*, 14, 344–363. <https://doi.org/10.1111/gbi.12178>.
- 1212 Cui, H., Kaufman, A.J., Xiao, S., Zhou, C., and Liu, X.-M. (2017) Was the Ediacaran Shuram Excursion  
1213 a globally synchronized early diagenetic event? Insights from methane-derived authigenic carbonates  
1214 in the uppermost Doushantuo Formation, South China. *Chemical Geology*, 450, 59–80.  
1215 <https://doi.org/10.1016/j.chemgeo.2016.12.010>.
- 1216 Cui, H., Kitajima, K., Spicuzza, M.J., Fournelle, J.H., Ishida, A., Brown, P.E., and Valley, J.W. (2018)  
1217 Searching for the Great Oxidation Event in North America: A reappraisal of the Huronian  
1218 Supergroup by SIMS sulfur four-isotope analysis. *Astrobiology*, In press.
- 1219 Ding, T., Valkiers, S., Kipphardt, H., De Bièvre, P., Taylor, P.D.P., Gonfiantini, R., and Krouse, R. (2001)  
1220 Calibrated sulfur isotope abundance ratios of three IAEA sulfur isotope reference materials and V-  
1221 CDT with a reassessment of the atomic weight of sulfur. *Geochimica et Cosmochimica Acta*, 65,  
1222 2433–2437. [https://doi.org/10.1016/S0016-7037\(01\)00611-1](https://doi.org/10.1016/S0016-7037(01)00611-1).
- 1223 Donovan, J.J., Kremser, D., Fournelle, J., and Goemann, K. (2018) Probe for Windows User's Guide and  
1224 Reference, Enterprise Edition. Probe Software, Inc., Eugene, OR
- 1225 Drake, H., Astrom, M.E., Heim, C., Broman, C., Astrom, J., Whitehouse, M., Ivarsson, M., Siljestrom, S.,  
1226 and Sjoval, P. (2015) Extreme  $^{13}\text{C}$  depletion of carbonates formed during oxidation of biogenic  
1227 methane in fractured granite. *Nature Communications*, 6, 7020. <https://doi.org/10.1038/ncomms8020>.

- 1228 Drake, H., Heim, C., Roberts, N.M.W., Zack, T., Tillberg, M., Broman, C., Ivarsson, M., Whitehouse,  
1229 M.J., and Åström, M.E. (2017) Isotopic evidence for microbial production and consumption of  
1230 methane in the upper continental crust throughout the Phanerozoic eon. *Earth and Planetary Science*  
1231 *Letters*, 470, 108–118. <https://doi.org/10.1016/j.epsl.2017.04.034>.
- 1232 Duda, J.-P., Zhu, M., and Reitner, J. (2015) Depositional dynamics of a bituminous carbonate facies in a  
1233 tectonically induced intra-platform basin: the Shibantan Member (Dengying Formation, Ediacaran  
1234 Period). *Carbonates and Evaporites*, 31, 87–99. <https://doi.org/10.1007/s13146-015-0243-8>.
- 1235 Eldridge, C.S., Walshe, J.L., Compston, W., Williams, I.S., Both, R.A., and Ohmoto, H. (1989) Sulfur  
1236 isotope variability in sediment-hosted massive sulfide deposits as determined using the ion  
1237 microprobe SHRIMP: I. An example from the Rammelsberg orebody—A reply. *Economic Geology*,  
1238 84, 453–457. <https://doi.org/10.2113/gsecongeo.84.2.453>.
- 1239 Feng, L., Chu, X., Huang, J., Zhang, Q., and Chang, H. (2010) Reconstruction of paleo-redox conditions  
1240 and early sulfur cycling during deposition of the Cryogenian Datangpo Formation in South China.  
1241 *Gondwana Research*, 18, 632–637. <https://doi.org/10.1016/j.gr.2010.02.011>.
- 1242 Ferrini, V., Fayek, M., De Vito, C., Mignardi, S., and Pignatti, J. (2010) Extreme sulphur isotope  
1243 fractionation in the deep Cretaceous biosphere. *Journal of the Geological Society*, 167, 1009–1018.  
1244 <https://doi.org/10.1144/0016-76492009-161>.
- 1245 Fike, D.A., Bradley, A.S., and Rose, C.V. (2015) Rethinking the ancient sulfur cycle. *Annual Review of*  
1246 *Earth and Planetary Sciences*, 43, 593–622. <https://doi.org/10.1146/annurev-earth-060313-054802>.
- 1247 Fike, D.A., and Grotzinger, J.P. (2008) A paired sulfate–pyrite  $\delta^{34}\text{S}$  approach to understanding the  
1248 evolution of the Ediacaran–Cambrian sulfur cycle. *Geochimica et Cosmochimica Acta*, 72, 2636–  
1249 2648. <https://doi.org/10.1016/j.gca.2008.03.021>.
- 1250 Fike, D.A., and Grotzinger, J.P. (2010) A  $\delta^{34}\text{S}_{\text{SO}_4}$  approach to reconstructing biogenic pyrite burial in  
1251 carbonate–evaporite basins: An example from the Ara Group, Sultanate of Oman. *Geology*, 38, 371–  
1252 374. <https://doi.org/10.1130/g30230.1>.
- 1253 Fike, D.A., Grotzinger, J.P., Pratt, L.M., and Summons, R.E. (2006) Oxidation of the Ediacaran ocean.  
1254 *Nature*, 444, 744–747. <https://doi.org/10.1038/nature05345>.
- 1255 Fischer, W.W., Fike, D.A., Johnson, J.E., Raub, T.D., Guan, Y., Kirschvink, J.L., and Eiler, J.M. (2014)  
1256 SQUID–SIMS is a useful approach to uncover primary signals in the Archean sulfur cycle.  
1257 *Proceedings of the National Academy of Sciences*, 111, 5468–5473.  
1258 <https://doi.org/10.1073/pnas.1322577111>.
- 1259 Friedman, I., and O'Neil, J.R. (1977) Data of Geochemistry: Compilation of Stable Isotope Fractionation  
1260 Factors of Geochemical Interest. Geological Survey Professional Paper 440, Chapter KK, United  
1261 States Government Printing Office, Washington, D.C., pp. KK1–KK12.
- 1262 Fu, Y., van Berk, W., and Schulz, H.-M. (2016) Hydrogen sulfide formation, fate, and behavior in  
1263 anhydrite-sealed carbonate gas reservoirs: A three-dimensional reactive mass transport modeling  
1264 approach. *AAPG Bulletin*, 100, 843–865. <https://doi.org/10.1306/12111514206>.
- 1265 Gadd, M.G., Layton-Matthews, D., Peter, J.M., Paradis, S., and Jonasson, I.R. (2017) The world-class  
1266 Howard's Pass SEDEX Zn–Pb district, Selwyn Basin, Yukon. Part II: the roles of thermochemical  
1267 and bacterial sulfate reduction in metal fixation. *Mineralium Deposita*, 52, 405–419.  
1268 <https://doi.org/10.1007/s00126-016-0672-x>.
- 1269 Ghazban, F., Schwarcz, H.P., and Ford, D.C. (1990) Carbon and sulfur isotope evidence for in situ  
1270 reduction of sulfate, Nanisivik lead–zinc deposits, Northwest Territories, Baffin Island, Canada.  
1271 *Economic Geology*, 85, 360–375. <https://doi.org/10.2113/gsecongeo.85.2.360>.
- 1272 Goldhaber, M., and Kaplan, I. (1975) Controls and consequences of sulfate reduction rates in recent  
1273 marine sediments. *Soil Science*, 119, 42–55.
- 1274 Goldhaber, M., and Kaplan, I. (1980) Mechanisms of sulfur incorporation and isotope fractionation  
1275 during early diagenesis in sediments of the Gulf of California. *Marine Chemistry*, 9, 95–143.  
1276 [https://doi.org/10.1016/0304-4203\(80\)90063-8](https://doi.org/10.1016/0304-4203(80)90063-8).
- 1277 Goldstein, T.P., and Aizenshtat, Z. (1994) Thermochemical sulfate reduction: A review. *Journal of*  
1278 *Thermal Analysis*, 42, 241–290. <https://doi.org/10.1007/bf02547004>.

- 1279 Gomes, M.L., Fike, D.A., Bergmann, K.D., Jones, C., and Knoll, A.H. (2018) Environmental insights  
1280 from high-resolution (SIMS) sulfur isotope analyses of sulfides in Proterozoic microbialites with  
1281 diverse mat textures. *Geobiology*, 16, 17–34. <https://doi.org/10.1111/gbi.12265>.
- 1282 Gomes, M.L., and Hurtgen, M.T. (2015) Sulfur isotope fractionation in modern euxinic systems:  
1283 Implications for paleoenvironmental reconstructions of paired sulfate–sulfide isotope records.  
1284 *Geochimica et Cosmochimica Acta*, 157, 39–55. <https://doi.org/10.1016/j.gca.2015.02.031>.
- 1285 Gorjan, P., Veevers, J.J., and Walter, M.R. (2000) Neoproterozoic sulfur-isotope variation in Australia  
1286 and global implications. *Precambrian Research*, 100, 151–179. [https://doi.org/10.1016/s0301-9268\(99\)00073-x](https://doi.org/10.1016/s0301-9268(99)00073-x).
- 1287  
1288 Gorjan, P., Walter, M.R., and Swart, R. (2003) Global Neoproterozoic (Sturtian) post-glacial sulfide-  
1289 sulfur isotope anomaly recognised in Namibia. *Journal of African Earth Sciences*, 36, 89–98.  
1290 [https://doi.org/10.1016/S0899-5362\(03\)00002-2](https://doi.org/10.1016/S0899-5362(03)00002-2).
- 1291 Graham, U., and Ohmoto, H. (1994) Experimental study of formation mechanisms of hydrothermal pyrite.  
1292 *Geochimica et Cosmochimica Acta*, 58, 2187–2202. [https://doi.org/10.1016/0016-7037\(94\)90004-3](https://doi.org/10.1016/0016-7037(94)90004-3).
- 1293 Habicht, K.S., Gade, M., Thamdrup, B., Berg, P., and Canfield, D.E. (2002) Calibration of sulfate levels  
1294 in the Archean ocean. *Science*, 298, 2372–2374. <https://doi.org/10.1126/science.1078265>.
- 1295 Halverson, G.P., and Hurtgen, M.T. (2007) Ediacaran growth of the marine sulfate reservoir. *Earth and*  
1296 *Planetary Science Letters*, 263, 32–44. <https://doi.org/10.1016/j.epsl.2007.08.022>.
- 1297 Halverson, G.P., Hurtgen, M.T., Porter, S.M., and Collins, A.S. (2009) Neoproterozoic–Cambrian  
1298 biogeochemical evolution. *Neoproterozoic-Cambrian Tectonics, Global Change and Evolution: A*  
1299 *Focus on Southwestern Gondwana. Developments in Precambrian Geology*, 16, 351–365.  
1300 [https://doi.org/10.1016/s0166-2635\(09\)01625-9](https://doi.org/10.1016/s0166-2635(09)01625-9).
- 1301 Halverson, G.P., and Shields-Zhou, G. (2011) Chemostratigraphy and the Neoproterozoic glaciations. In  
1302 E. Arnaud, G.P. Halverson, and G. Shields-Zhou, Eds. *The Geological Record of Neoproterozoic*  
1303 *Glaciations*. Geological Society, London, Memoirs, 36, p. 51–66.
- 1304 Halverson, G.P., Wade, B.P., Hurtgen, M.T., and Barovich, K.M. (2010) Neoproterozoic  
1305 chemostratigraphy. *Precambrian Research*, 182, 337–350.  
1306 <https://doi.org/10.1016/j.precamres.2010.04.007>.
- 1307 Hao, F., Guo, T., Zhu, Y., Cai, X., Zou, H., and Li, P. (2008) Evidence for multiple stages of oil cracking  
1308 and thermochemical sulfate reduction in the Puguang gas field, Sichuan Basin, China. *AAPG*  
1309 *Bulletin*, 92, 611–637.
- 1310 Harrison, A., and Thode, H. (1958) Mechanism of the bacterial reduction of sulfate from isotope  
1311 fractionation studies. *Transactions of the Royal Faraday Society*, 54, 84–92.  
1312 <https://doi.org/10.1039/tf9585400084>.
- 1313 Hayes, J.M., Lambert, I.B., and Strauss, H. (1992) The Sulfur-Isotopic Record. In J.W. Schopf, and C.  
1314 Klein, Eds. *The Proterozoic Biosphere: A Multidisciplinary Study*, p. 129–132. Cambridge  
1315 University Press, Cambridge.
- 1316 He, Z., Yang, R., Gao, J., Cheng, W., and Wen, G. (2013a) The structure character of manganese ore  
1317 deposit of Datangpo-period of Neoproterozoic in Songtao of Guizhou. *China's Manganese Industry*,  
1318 31, 5–16 (in Chinese with English abstract).
- 1319 He, Z., Yang, R., Gao, J., Cheng, W., Zhang, R., and Zhang, P. (2013b) Sedimentary geochemical  
1320 characteristics of manganese deposits in Xixibao, Songtao County, Guizhou Province. *Geochimica*,  
1321 42, 576–588 (in Chinese with English abstract).
- 1322 Heydari, E., and Moore, C.H. (1989) Burial diagenesis and thermochemical sulfate reduction, Smackover  
1323 Formation, southeastern Mississippi salt basin. *Geology*, 17, 1080–1084.  
1324 [https://doi.org/10.1130/0091-7613\(1989\)017<1080:bdatsr>2.3.co;2](https://doi.org/10.1130/0091-7613(1989)017<1080:bdatsr>2.3.co;2).
- 1325 Hoffman, P.F., Abbot, D.S., Ashkenazy, Y., Benn, D.I., Brocks, J.J., Cohen, P.A., Cox, G.M., Creveling,  
1326 J.R., Donnadieu, Y., Erwin, D.H., Fairchild, I.J., Ferreira, D., Goodman, J.C., Halverson, G.P.,  
1327 Jansen, M.F., Le Hir, G., Love, G.D., Macdonald, F.A., Maloof, A.C., Partin, C.A., Ramstein, G.,  
1328 Rose, B.E.J., Rose, C.V., Sadler, P.M., Tziperman, E., Voigt, A., and Warren, S.G. (2017) Snowball

- 1329 Earth climate dynamics and Cryogenian geology–geobiology. *Science Advances*, 3, e1600983.  
1330 <https://doi.org/10.1126/sciadv.1600983>.
- 1331 Hoffman, P.F., Kaufman, A.J., Halverson, G.P., and Schrag, D.P. (1998) A Neoproterozoic Snowball  
1332 Earth. *Science*, 281, 1342–1346. <https://doi.org/10.1126/science.281.5381.1342>.
- 1333 Hoffman, P.F., and Li, Z.-X. (2009) A palaeogeographic context for Neoproterozoic glaciation.  
1334 *Palaeogeography, Palaeoclimatology, Palaeoecology*, 277, 158–172.  
1335 <https://doi.org/10.1016/j.palaeo.2009.03.013>.
- 1336 Hoffman, P.F., and Schrag, D.P. (2002) The snowball Earth hypothesis: testing the limits of global  
1337 change. *Terra Nova*, 14, 129–155. <https://doi.org/10.1046/j.1365-3121.2002.00408.x>.
- 1338 Hurtgen, M.T., Arthur, M.A., and Halverson, G.P. (2005) Neoproterozoic sulfur isotopes, the evolution of  
1339 microbial sulfur species, and the burial efficiency of sulfide as sedimentary pyrite. *Geology*, 33, 41–  
1340 44. <https://doi.org/10.1130/g20923.1>.
- 1341 Hurtgen, M.T., Arthur, M.A., Suits, N.S., and Kaufman, A.J. (2002) The sulfur isotopic composition of  
1342 Neoproterozoic seawater sulfate: implications for a snowball Earth? *Earth and Planetary Science*  
1343 *Letters*, 203, 413–429. [https://doi.org/10.1016/s0012-821x\(02\)00804-x](https://doi.org/10.1016/s0012-821x(02)00804-x).
- 1344 Jia, L., Cai, C., Yang, H., Li, H., Wang, T., Zhang, B., Jiang, L., and Tao, X. (2015) Thermochemical and  
1345 bacterial sulfate reduction in the Cambrian and Lower Ordovician carbonates in the Tazhong Area,  
1346 Tarim Basin, NW China: evidence from fluid inclusions, C, S, and Sr isotopic data. *Geofluids*, 15,  
1347 421–437. <https://doi.org/10.1111/gfl.12105>.
- 1348 Jiang, G., Kaufman, A.J., Christie-Blick, N., Zhang, S., and Wu, H. (2007) Carbon isotope variability  
1349 across the Ediacaran Yangtze platform in South China: Implications for a large surface-to-deep  
1350 ocean  $\delta^{13}\text{C}$  gradient. *Earth and Planetary Science Letters*, 261, 303–320.  
1351 <https://doi.org/10.1016/j.epsl.2007.07.009>.
- 1352 Jiang, G., Shi, X., Zhang, S., Wang, Y., and Xiao, S. (2011) Stratigraphy and paleogeography of the  
1353 Ediacaran Doushantuo Formation (ca. 635–551Ma) in South China. *Gondwana Research*, 19, 831–  
1354 849. <https://doi.org/10.1016/j.gr.2011.01.006>.
- 1355 Jiang, G., Sohl, L.E., and Christie-Blick, N. (2003) Neoproterozoic stratigraphic comparison of the Lesser  
1356 Himalaya (India) and Yangtze block (south China): Paleogeographic implications. *Geology*, 31,  
1357 917–920. <https://doi.org/10.1130/g19790.1>.
- 1358 Jiang, L., Worden, R.H., and Cai, C. (2015) Generation of isotopically and compositionally distinct water  
1359 during thermochemical sulfate reduction (TSR) in carbonate reservoirs: Triassic Feixianguan  
1360 Formation, Sichuan Basin, China. *Geochimica et Cosmochimica Acta*, 165, 249–262.  
1361 <https://doi.org/10.1016/j.gca.2015.05.033>.
- 1362 Jiang, L., Worden, R.H., and Cai, C.F. (2014) Thermochemical sulfate reduction and fluid evolution of  
1363 the Lower Triassic Feixianguan Formation sour gas reservoirs, northeast Sichuan Basin, China.  
1364 *AAPG bulletin*, 98, 947–973. <https://doi.org/10.1306/10171312220>.
- 1365 Jiang, L., Worden, R.H., and Yang, C. (2018) Thermochemical sulphate reduction can improve carbonate  
1366 petroleum reservoir quality. *Geochimica et Cosmochimica Acta*, 223, 127–140.  
1367 <https://doi.org/10.1016/j.gca.2017.11.032>.
- 1368 Johnson, J.E., Webb, S.M., Thomas, K., Ono, S., Kirschvink, J.L., and Fischer, W.W. (2013) Manganese-  
1369 oxidizing photosynthesis before the rise of cyanobacteria. *Proceedings of the National Academy of*  
1370 *Sciences*, 110, 11238–11243. <https://doi.org/10.1073/pnas.1305530110>.
- 1371 Johnston, D.T., Wing, B.A., Farquhar, J., Kaufman, A.J., Strauss, H., Lyons, T.W., Kah, L.C., and  
1372 Canfield, D.E. (2005) Active microbial sulfur disproportionation in the Mesoproterozoic. *Science*,  
1373 310, 1477–1479. <https://doi.org/10.1126/science.1117824>.
- 1374 Jones, D., Hartley, J., Frisch, G., Purnell, M., and Darras, L. (2012) Non-destructive, safe removal of  
1375 conductive metal coatings from fossils: a new solution. *Palaeontologia Electronica*, 15, 4T.
- 1376 Jørgensen, B.B., Böttcher, M.E., Lüschen, H., Neretin, L.N., and Volkov, I.I. (2004) Anaerobic methane  
1377 oxidation and a deep  $\text{H}_2\text{S}$  sink generate isotopically heavy sulfides in Black Sea sediments 1.  
1378 *Geochimica et Cosmochimica Acta*, 68, 2095–2118. <https://doi.org/10.1016/j.gca.2003.07.017>.

- 1379 Jørgensen, B.B., Isaksen, M.F., and Jannasch, H.W. (1992) Bacterial sulfate reduction above 100 °C in  
1380 deep-sea hydrothermal vent sediments. *Science*, 258, 1756–1757.  
1381 <https://doi.org/10.1126/science.258.5089.1756>.
- 1382 Jørgensen, B.B., and Kasten, S. (2006) Sulfur cycling and methane oxidation. In H.D. Schulz, and M.  
1383 Zabel, Eds. *Marine Geochemistry*, p. 271–309. Springer-Verlag Berlin Heidelberg, Berlin.
- 1384 Kah, L.C., and Bartley, J.K. (2011) Protracted oxygenation of the Proterozoic biosphere. *International*  
1385 *Geology Review*, 53, 1424–1442. <https://doi.org/10.1080/00206814.2010.527651>.
- 1386 Kah, L.C., Lyons, T.W., and Frank, T.D. (2004) Low marine sulphate and protracted oxygenation of the  
1387 Proterozoic biosphere. *Nature*, 431, 834–838. <https://doi.org/10.1038/nature02974>.
- 1388 Kaplan, I.R., and Rafter, T.A. (1958) Fractionation of stable isotopes of sulfur by Thiobacilli. *Science*,  
1389 127, 517–518. <https://doi.org/10.1126/science.127.3297.517>.
- 1390 Kaplan, I.R., and Rittenberg, S.C. (1964) Microbiological fractionation of sulphur isotopes. *Microbiology*,  
1391 34, 195–212. <https://doi.org/10.1099/00221287-34-2-195>.
- 1392 Kelley, K.D., Dumoulin, J.A., and Jennings, S. (2004a) The Anarraaq Zn-Pb-Ag and Barite Deposit,  
1393 Northern Alaska: Evidence for Replacement of Carbonate by Barite and Sulfides. *Economic Geology*,  
1394 99, 1577–1591. <https://doi.org/10.2113/gsecongeo.99.7.1577>.
- 1395 Kelley, K.D., Leach, D.L., Johnson, C.A., Clark, J.L., Fayek, M., Slack, J.F., Anderson, V.M., Ayuso,  
1396 R.A., and Ridley, W.I. (2004b) Textural, compositional, and sulfur isotope variations of sulfide  
1397 minerals in the Red Dog Zn-Pb-Ag deposits, Brooks Range, Alaska: Implications for ore formation.  
1398 *Economic Geology*, 99, 1509–1532. <https://doi.org/10.2113/gsecongeo.99.7.1509>.
- 1399 King, H.E., Walters, C.C., Horn, W.C., Zimmer, M., Heines, M.M., Lamberti, W.A., Kliever, C., Pottorf,  
1400 R.J., and Macleod, G. (2014) Sulfur isotope analysis of bitumen and pyrite associated with thermal  
1401 sulfate reduction in reservoir carbonates at the Big Piney–La Barge production complex. *Geochimica*  
1402 *et Cosmochimica Acta*, 134, 210–220. <https://doi.org/10.1016/j.gca.2013.11.005>.
- 1403 Kirschvink, J.L. (1992) Late Proterozoic Low-Latitude Global Glaciation: the Snowball Earth. In J.W.  
1404 Schopf, C. Klein, and D. Des Maris, Eds. *The Proterozoic Biosphere: A Multidisciplinary Study*, p.  
1405 51–52. Cambridge University Press, New York, USA.
- 1406 Kiyosu, Y. (1980) Chemical reduction and sulfur-isotope effects of sulfate by organic matter under  
1407 hydrothermal conditions. *Chemical Geology*, 30, 47–56. [https://doi.org/10.1016/0009-2541\(80\)90115-1](https://doi.org/10.1016/0009-2541(80)90115-1).
- 1409 Kiyosu, Y., and Krouse, H.R. (1990) The role of organic acid in the abiogenic reduction of sulfate and the  
1410 sulfur isotope effect. *Geochemical Journal*, 24, 21–27. <https://doi.org/10.2343/geochemj.24.21>.
- 1411 Kohn, M.J., Riciputi, L.R., Stakes, D., and Orange, D.L. (1998) Sulfur isotope variability in biogenic  
1412 pyrite: Reflections of heterogeneous bacterial colonization? *American Mineralogist*, 83, 1454–1468.  
1413 <https://doi.org/10.2138/am-1997-11-1234>.
- 1414 Krouse, H.R., Viau, C.A., Eliuk, L.S., Ueda, A., and Halas, S. (1988) Chemical and isotopic evidence of  
1415 thermochemical sulphate reduction by light hydrocarbon gases in deep carbonate reservoirs. *Nature*,  
1416 333, 415–419. <https://doi.org/10.1038/333415a0>.
- 1417 Kunzmann, M., Bui, T.H., Crockford, P.W., Halverson, G.P., Scott, C., Lyons, T.W., and Wing, B.A.  
1418 (2017) Bacterial sulfur disproportionation constrains timing of Neoproterozoic oxygenation. *Geology*,  
1419 45, 207–210. <https://doi.org/10.1130/g38602.1>.
- 1420 Lan, Z., Li, X.-H., Zhang, Q., and Li, Q.-L. (2015a) Global synchronous initiation of the 2nd episode of  
1421 Sturtian glaciation: SIMS zircon U–Pb and O isotope evidence from the Jiangkou Group, South  
1422 China. *Precambrian Research*, 267, 28–38. <https://doi.org/10.1016/j.precamres.2015.06.002>.
- 1423 Lan, Z., Li, X.-H., Zhu, M., Zhang, Q., and Li, Q.-L. (2015b) Revisiting the Liantuo Formation in  
1424 Yangtze Block, South China: SIMS U–Pb zircon age constraints and regional and global significance.  
1425 *Precambrian Research*, 263, 123–141. <https://doi.org/10.1016/j.precamres.2015.03.012>.
- 1426 Lang, X., 2016, *The Process of Nanhua Glaciation and the Synglacial Evolution of Marine Geochemistry*  
1427 *in the South China Block, China: Ph.D. Dissertation (in Chinese with English abstract)*, Peking  
1428 University, Beijing, China, 108 p.

- 1429 Lang, X., Shen, B., Peng, Y., Zhou, C., and Huang, K. (2016) A New Pathway of Sulfur Cycling in the  
1430 Cryogenian Ocean. Geological Society of America Abstracts with Programs. Vol. 48, No. 7, 48,  
1431 Denver, Colorado, USA.
- 1432 Leavitt, W.D., 2014, On the Mechanisms of Sulfur Isotope Fractionation During Microbial Sulfate  
1433 Reduction: Ph.D. Dissertation, Harvard University, Cambridge, Massachusetts, USA, 242 p.
- 1434 Leavitt, W.D., Bradley, A.S., Halevy, I., and Johnston, D.T. (2013) Influence of sulfate reduction rates on  
1435 the Phanerozoic sulfur isotope record. Proceedings of the National Academy of Sciences, 110,  
1436 11244–11249. <https://doi.org/10.1073/pnas.1218874110>.
- 1437 Li, C., Love, G.D., Lyons, T.W., Scott, C.T., Feng, L., Huang, J., Chang, H., Zhang, Q., and Chu, X.  
1438 (2012) Evidence for a redox stratified Cryogenian marine basin, Datangpo Formation, South China.  
1439 Earth and Planetary Science Letters, 331–332, 246–256. <https://doi.org/10.1016/j.epsl.2012.03.018>.
- 1440 Li, R., Chen, J., Zhang, S., Lei, J., Shen, Y., and Chen, X. (1999a) Spatial and temporal variations in  
1441 carbon and sulfur isotopic compositions of Sinian sedimentary rocks in the Yangtze platform, South  
1442 China. Precambrian Research, 97, 59–75. [https://doi.org/10.1016/s0301-9268\(99\)00022-4](https://doi.org/10.1016/s0301-9268(99)00022-4).
- 1443 Li, R., Zhang, S., Lei, J., Shen, Y., Chen, J., and Chu, X. (1996) Temporal and spacial variation in  $\delta^{34}\text{S}$   
1444 values of pyrite from Sinian strata discussion on relationship between Yangtze Block and the late  
1445 Proterozoic supercontinent. Scientia Geologica Sinica, 31, 209–217 (in Chinese with English  
1446 abstract).
- 1447 Li, Z.-X. (2011) Breakup of Rodinia. In J. Reitner, and V. Thiel, Eds. Encyclopedia of Geobiology, p.  
1448 206–210. Springer Netherlands.
- 1449 Li, Z.-X., Evans, D.A.D., and Halverson, G.P. (2013) Neoproterozoic glaciations in a revised global  
1450 palaeogeography from the breakup of Rodinia to the assembly of Gondwanaland. Sedimentary  
1451 Geology, 294, 219–232. <https://doi.org/10.1016/j.sedgeo.2013.05.016>.
- 1452 Li, Z., Li, X., Kinny, P., and Wang, J. (1999b) The breakup of Rodinia: did it start with a mantle plume  
1453 beneath South China? Earth and Planetary Science Letters, 173, 171–181.  
1454 [https://doi.org/10.1016/S0012-821X\(99\)00240-X](https://doi.org/10.1016/S0012-821X(99)00240-X).
- 1455 Lin, Q., Wang, J., Algeo, T.J., Sun, F., and Lin, R. (2016a) Enhanced framboidal pyrite formation related  
1456 to anaerobic oxidation of methane in the sulfate-methane transition zone of the northern South China  
1457 Sea. Marine Geology, 379, 100–108. <https://doi.org/10.1016/j.margeo.2016.05.016>.
- 1458 Lin, Z., Sun, X., Lu, Y., Strauss, H., Xu, L., Gong, J., Teichert, B.M.A., Lu, R., Lu, H., Sun, W., and  
1459 Peckmann, J. (2017) The enrichment of heavy iron isotopes in authigenic pyrite as a possible  
1460 indicator of sulfate-driven anaerobic oxidation of methane: Insights from the South China Sea.  
1461 Chemical Geology, 449, 15–29. <https://doi.org/10.1016/j.chemgeo.2016.11.032>.
- 1462 Lin, Z., Sun, X., Peckmann, J., Lu, Y., Xu, L., Strauss, H., Zhou, H., Gong, J., Lu, H., and Teichert,  
1463 B.M.A. (2016b) How sulfate-driven anaerobic oxidation of methane affects the sulfur isotopic  
1464 composition of pyrite: A SIMS study from the South China Sea. Chemical Geology, 440, 26–41.  
1465 <https://doi.org/10.1016/j.chemgeo.2016.07.007>.
- 1466 Liu, A.G. (2016) Framboidal pyrite shroud confirms the ‘death mask’ model for moldic preservation of  
1467 Ediacaran soft-bodied organisms. Palaios, 31, 259–274. <https://doi.org/10.2110/palo.2015.095>.
- 1468 Liu, Q., Zhu, D., Jin, Z., Liu, C., Zhang, D., and He, Z. (2016) Coupled alteration of hydrothermal fluids  
1469 and thermal sulfate reduction (TSR) in ancient dolomite reservoirs – An example from Sinian  
1470 Dengying Formation in Sichuan Basin, southern China. Precambrian Research, 285, 39–57.  
1471 <https://doi.org/10.1016/j.precamres.2016.09.006>.
- 1472 Liu, T.-B., Maynard, J.B., and Alten, J. (2006) Superheavy S isotopes from glacier-associated sediments  
1473 of the Neoproterozoic of south China: Oceanic anoxia or sulfate limitation? Geological Society of  
1474 America Memoirs, 198, 205–222. [https://doi.org/10.1130/2006.1198\(12\)](https://doi.org/10.1130/2006.1198(12)).
- 1475 Logan, G.A., Hayes, J., Hieshima, G.B., and Summons, R.E. (1995) Terminal Proterozoic reorganization  
1476 of biogeochemical cycles. Nature, 376, 53–56. <https://doi.org/10.1038/376053a0>.
- 1477 Love, L., and Amstutz, G. (1969) Framboidal pyrite in two andesites. Neues Jahrbuch fur Mineralogie.  
1478 Monatshefte, 3, 97–108.

- 1479 Lu, M., Zhu, M., Zhang, J., Shields-Zhou, G., Li, G., Zhao, F., Zhao, X., and Zhao, M. (2013) The  
1480 DOUNCE event at the top of the Ediacaran Doushantuo Formation, South China: Broad stratigraphic  
1481 occurrence and non-diagenetic origin. *Precambrian Research*, 225, 86–109.  
1482 <https://doi.org/10.1016/j.precamres.2011.10.018>.
- 1483 Machel, H.-G. (1987) Saddle dolomite as a by-product of chemical compaction and thermochemical  
1484 sulfate reduction. *Geology*, 15, 936–940. [https://doi.org/10.1130/0091-  
1485 7613\(1987\)15<936:sdaabo>2.0.co;2](https://doi.org/10.1130/0091-7613(1987)15<936:sdaabo>2.0.co;2).
- 1486 Machel, H.G. (2001) Bacterial and thermochemical sulfate reduction in diagenetic settings — old and  
1487 new insights. *Sedimentary Geology*, 140, 143–175. [https://doi.org/10.1016/s0037-0738\(00\)00176-7](https://doi.org/10.1016/s0037-0738(00)00176-7).
- 1488 Machel, H.G., and Buschkuhle, B.E. (2008) Diagenesis of the Devonian Southesk-Cairn Carbonate  
1489 Complex, Alberta, Canada: marine cementation, burial dolomitization, thermochemical sulfate  
1490 reduction, anhydritization, and squeegee fluid flow. *Journal of Sedimentary Research*, 78, 366–389.  
1491 <https://doi.org/10.2110/jsr.2008.037>.
- 1492 Machel, H.G., Krouse, H.R., and Sassen, R. (1995) Products and distinguishing criteria of bacterial and  
1493 thermochemical sulfate reduction. *Applied Geochemistry*, 10, 373–389.  
1494 [https://doi.org/10.1016/0883-2927\(95\)00008-8](https://doi.org/10.1016/0883-2927(95)00008-8).
- 1495 Machel, H.G., Riciputi, L.R., and Cole, D.R. (1997) Ion microprobe investigation of diagenetic  
1496 carbonates and sulfides in the Devonian Nisku Formation, Alberta, Canada. In I.P. Montañez, J.M.  
1497 Gregg, and K.L. Shelton, Eds. *Basin-Wide Diagenetic Patterns: Integrated petrologic, Geochemical  
1498 and Hydrologic Considerations*, SEPM Special Publication 57. Society for Sedimentary Geology  
1499 (SEPM).
- 1500 Marin-Carbone, J., Remusat, L., Sforza, M.C., Thomazo, C., Cartigny, P., and Philippot, P. (2018)  
1501 Sulfur isotope's signal of nanopyrates enclosed in 2.7 Ga stromatolitic organic remains reveal  
1502 microbial sulfate reduction. *Geobiology*, n/a-n/a. <https://doi.org/10.1111/gbi.12275>.
- 1503 Marini, L., Moretti, R., and Accornero, M. (2011) Sulfur Isotopes in Magmatic-Hydrothermal Systems,  
1504 Melts, and Magmas. In H. Behrens, and J.D. Webster, Eds. *Reviews in Mineralogy and  
1505 Geochemistry Volume 73: Sulfur in Magmas and Melts: Its Importance for Natural and Technical  
1506 Processes*, 73, p. 423–492. Mineralogical Society of America, USA.
- 1507 McFadden, K.A., Huang, J., Chu, X., Jiang, G., Kaufman, A.J., Zhou, C., Yuan, X., and Xiao, S. (2008)  
1508 Pulsed oxidation and biological evolution in the Ediacaran Doushantuo Formation. *Proceedings of  
1509 the National Academy of Sciences*, 105, 3197–3202. <https://doi.org/10.1073/pnas.0708336105>.
- 1510 McKibben, M.A., and Riciputi, L.R. (1998) Sulfur Isotopes by Ion Microprobe. In M.A. McKibben, W.C.  
1511 Shanks III, and W.I. Ridley, Eds. *Applications of Microanalytical Techniques to Understanding  
1512 Mineralizing Processes. Reviews in Economic Geology, Volume 7*, 7, p. 121–139. Society of  
1513 Economic Geologist, Littleton, Colorado, USA.
- 1514 McLoughlin, N., Grosch, E.G., Kilburn, M.R., and Wacey, D. (2012) Sulfur isotope evidence for a  
1515 Paleoproterozoic subseafloor biosphere, Barberton, South Africa. *Geology*, 40, 1031–1034.  
1516 <https://doi.org/10.1130/g33313.1>.
- 1517 Meyer, N.R., Zerkle, A.L., and Fike, D.A. (2017) Sulphur cycling in a Neoproterozoic microbial mat.  
1518 *Geobiology*, 15, 353–365. <https://doi.org/10.1111/gbi.12227>.
- 1519 Narbonne, G.M., Xiao, S., Shields, G.A., and Gehling, J.G. (2012) The Ediacaran Period. In F.M.  
1520 Gradstein, J.G. Ogg, M.D. Schmitz, and G.M. Ogg, Eds. *The Geologic Time Scale*, p. 413–435.  
1521 Elsevier, Boston, USA.
- 1522 Och, L.M., and Shields-Zhou, G.A. (2012) The Neoproterozoic oxygenation event: Environmental  
1523 perturbations and biogeochemical cycling. *Earth-Science Reviews*, 110, 26–57.  
1524 <https://doi.org/10.1016/j.earscirev.2011.09.004>.
- 1525 Oduro, H., Harms, B., Sintim, H.O., Kaufman, A.J., Cody, G., and Farquhar, J. (2011) Evidence of  
1526 magnetic isotope effects during thermochemical sulfate reduction. *Proceedings of the National  
1527 Academy of Sciences*, 108, 17635–17638. <https://doi.org/10.1073/pnas.1108112108>.
- 1528 Ohfuji, H., and Rickard, D. (2005) Experimental syntheses of frambooids—a review. *Earth-Science  
1529 Reviews*, 71, 147–170. <https://doi.org/10.1016/j.earscirev.2005.02.001>.

- 1530 Ohmoto, H. (1986) Stable isotope geochemistry of ore deposits. In J.W. Valley, J. Taylor, H.P. , and J.R.  
1531 O'Neil, Eds. Stable Isotopes in High Temperature Geological Processes, Reviews in Mineralogy  
1532 Volume 16, p. 491–559. Mineralogical Society of America.
- 1533 Ohmoto, H., and Goldhaber, M.B. (1997) Sulfur and carbon isotopes. In H.L. Barnes, Ed. Geochemistry  
1534 of Hydrothermal Ore Deposits, 3rd Edition, p. 517–611. John Wiley & Sons, New York.
- 1535 Ohmoto, H., and Lasaga, A.C. (1982) Kinetics of reactions between aqueous sulfates and sulfides in  
1536 hydrothermal systems. *Geochimica et Cosmochimica Acta*, 46, 1727–1745.  
1537 [https://doi.org/10.1016/0016-7037\(82\)90113-2](https://doi.org/10.1016/0016-7037(82)90113-2).
- 1538 Ohmoto, H., Watanabe, Y., Lasaga, A.C., Naraoka, H., Johnson, I., Brainard, J., and Chorney, A. (2014)  
1539 Oxygen, iron, and sulfur geochemical cycles on early Earth: Paradigms and contradictions.  
1540 Geological Society of America Special Papers, 504, 55-95.
- 1541 Olanipekun, B.J., and Azmy, K. (2018) In situ geochemical characterization of pyrite crystals in burial  
1542 dolomites of St. George Group carbonates. *Canadian Journal of Earth Sciences*, in press.  
1543 <https://doi.org/10.1139/cjes-2016-0152>.
- 1544 Orr, W.L. (1974) Changes in sulfur content and isotopic ratios of sulfur during petroleum maturation —  
1545 Study of Big Horn Basin Paleozoic oils. *AAPG Bulletin*, 58, 2295–2318.
- 1546 Orr, W.L. (1977) Geologic and geochemical controls on the distribution of hydrogen sulfide in natural gas.  
1547 In R. Campos, and J. Goni, Eds. *Advances in Organic Geochemistry 1975*, 50, p. 571–597.  
1548 Pergamon, Oxford, UK.
- 1549 Ostwald, J., and England, B.M. (1979) The relationship between euhedral and framboidal pyrite in base-  
1550 metal sulphide ores. *Mineralogical Magazine*, 43, 297–300.
- 1551 Pan, W., Zhuo, X., Chen, X., Yang, S., and Zhao, S. (2016) Geochemical characteristics of manganese  
1552 bearing rock series in black shale basins of Northeast Guizhou, China. *Acta Sedimentologica Sinica*,  
1553 34, 868–880 (in Chinese with English abstract). <https://doi.org/10.14027/j.cnki.cjxb.2016.05.006>.
- 1554 Parnell, J., and Boyce, A.J. (2017) Microbial sulphate reduction during Neoproterozoic glaciation, Port  
1555 Askaig Formation, UK. *Journal of the Geological Society*, 174, 850–854.  
1556 <https://doi.org/10.1144/jgs2016-147>.
- 1557 Pasquier, V., Sansjofre, P., Rabineau, M., Revillon, S., Houghton, J., and Fike, D.A. (2017) Pyrite sulfur  
1558 isotopes reveal glacial–interglacial environmental changes. *Proceedings of the National Academy of*  
1559 *Sciences*, 114, 5941–5945. <https://doi.org/10.1073/pnas.1618245114>.
- 1560 Paytan, A., and Gray, E.T. (2012) Chapter 9 - Sulfur Isotope Stratigraphy. In F.M. Gradstein, J.G. Ogg,  
1561 M.D. Schmitz, and G.M. Ogg, Eds. *The Geologic Time Scale*, p. 167–180. Elsevier, Boston.
- 1562 Peevler, J., Fayek, M., Misra, K.C., and Riciputi, L.R. (2003) Sulfur isotope microanalysis of sphalerite  
1563 by SIMS: constraints on the genesis of Mississippi valley-type mineralization, from the Mascot-  
1564 Jefferson City district, East Tennessee. *Journal of Geochemical Exploration*, 80, 277–296.  
1565 [https://doi.org/10.1016/s0375-6742\(03\)00195-x](https://doi.org/10.1016/s0375-6742(03)00195-x).
- 1566 Peng, X., Guo, Z., Chen, S., Sun, Z., Xu, H., Ta, K., Zhang, J., Zhang, L., Li, J., and Du, M. (2017)  
1567 Formation of carbonate pipes in the northern Okinawa Trough linked to strong sulfate exhaustion  
1568 and iron supply. *Geochimica et Cosmochimica Acta*, 205, 1–13.  
1569 <https://doi.org/10.1016/j.gca.2017.02.010>.
- 1570 Peterson, K.J., Lyons, J.B., Nowak, K.S., Takacs, C.M., Wargo, M.J., and McPeck, M.A. (2004)  
1571 Estimating metazoan divergence times with a molecular clock. *Proceedings of the National Academy*  
1572 *of Sciences of the United States of America*, 101, 6536–6541.  
1573 <https://doi.org/10.1073/pnas.0401670101>.
- 1574 Popa, R., Kinkle, B.K., and Badescu, A. (2004) Pyrite framboids as biomarkers for iron-sulfur systems.  
1575 *Geomicrobiology Journal*, 21, 193–206. <https://doi.org/10.1080/01490450490275497>.
- 1576 Powell, T.G., and Macqueen, R.W. (1984) Precipitation of sulfide ores and organic matter: sulfate  
1577 reactions at Pine Point, Canada. *Science*, 224, 63–67. <https://doi.org/10.1126/science.224.4644.63>.
- 1578 Qin, Y., An, Z., Wang, J., and Li, D. (2013) The discovery and geological characteristics of the super-  
1579 large sized Daotuo manganese deposit in Songtao, Guizhou. *Mineral Exploration*, 345–355 (in  
1580 Chinese with English abstract).

- 1581 Raiswell, R. (1982) Pyrite texture, isotopic composition and the availability of iron. *American Journal of*  
1582 *Science*, 282, 1244–1263. <https://doi.org/10.2475/ajs.282.8.1244>.
- 1583 Randell, R.N., and Anderson, G.M. (1996) Geology of the Polaris Zn-Pb deposit and surrounding area,  
1584 Canadian Arctic Archipelago. In D.F. Sangster, Ed. *Carbonate-Hosted Lead-Zinc Deposits*, 75th  
1585 Anniversary Volume, 4, p. 307–319, Society of Economic Geology, Special Publication.
- 1586 Riciputi, L.R., Cole, D.R., and Machel, H.G. (1996) Sulfide formation in reservoir carbonates of the  
1587 Devonian Nisku Formation, Alberta, Canada: An ion microprobe study. *Geochimica et*  
1588 *Cosmochimica Acta*, 60, 325–336. [https://doi.org/10.1016/0016-7037\(96\)83133-4](https://doi.org/10.1016/0016-7037(96)83133-4).
- 1589 Ries, J.B., Fike, D.A., Pratt, L.M., Lyons, T.W., and Grotzinger, J.P. (2009) Superheavy pyrite ( $\delta^{34}\text{S}_{\text{pyr}} >$   
1590  $\delta^{34}\text{S}_{\text{CAS}}$ ) in the terminal Proterozoic Nama Group, southern Namibia: A consequence of low seawater  
1591 sulfate at the dawn of animal life. *Geology*, 37, 743–746. <https://doi.org/10.1130/g25775a.1>.
- 1592 Rooney, A.D., Strauss, J.V., Brandon, A.D., and Macdonald, F.A. (2015) A Cryogenian chronology: Two  
1593 long-lasting synchronous Neoproterozoic glaciations. *Geology*, 43, 459–462.  
1594 <https://doi.org/10.1130/g36511.1>.
- 1595 Runnegar, B. (1982) A molecular - clock date for the origin of the animal phyla. *Lethaia*, 15, 199 – 205.  
1596 <https://doi.org/10.1111/j.1502-3931.1982.tb00645.x>.
- 1597 Rust, G.W. (1935) Colloidal primary copper ores at Cornwall mines, southeastern Missouri. *The Journal*  
1598 *of Geology*, 43, 398–426. <https://doi.org/10.1086/624318>.
- 1599 Rye, R.O., and Ohmoto, H. (1974) Sulfur and carbon isotopes and ore genesis: A review. *Economic*  
1600 *Geology*, 69, 826–842. <https://doi.org/10.2113/gsecongeo.69.6.826>.
- 1601 Schallreuter, R. (1984) Framboidal pyrite in deep-sea sediments. In W.W. Hay, and J.-C. Sibuet, Eds.  
1602 *Initial Reports of the Deep Sea Drilling Project*, 75, p. 875–891, Washington (U.S. Govt. Printing  
1603 Office).
- 1604 Scheller, E.L., Dickson, A.J., Canfield, D.E., Korte, C., Kristiansen, K.K., and Dahl, T.W. (2018) Ocean  
1605 redox conditions between the Snowballs – geochemical constraints from Arena Formation, East  
1606 Greenland. *Precambrian Research*, In press. <https://doi.org/10.1016/j.precamres.2017.12.009>.
- 1607 Schieber, J. (2011) Iron Sulfide Formation. In J. Reitner, and V. Thiel, Eds. *Encyclopedia of Geobiology*,  
1608 p. 486–502. Springer Netherlands.
- 1609 Schmitz, M.D. (2012) Radiometric ages used in GTS2012. In F.M. Gradstein, J.G. Ogg, M.D. Schmitz,  
1610 and G.M. Ogg, Eds. *The Geologic Time Scale*, p. 1045–1082. Elsevier, Boston.
- 1611 Scott, R.J., Meffre, S., Woodhead, J., Gilbert, S.E., Berry, R.F., and Emsbo, P. (2009) Development of  
1612 framboidal pyrite during diagenesis, low-grade regional metamorphism, and hydrothermal alteration.  
1613 *Economic Geology*, 104, 1143–1168. <https://doi.org/10.2113/gsecongeo.104.8.1143>.
- 1614 Seal, R.R. (2006) Sulfur isotope geochemistry of sulfide minerals. In D.J. Vaughan, Ed. *Reviews in*  
1615 *Mineralogy and Geochemistry Vol. 61: Sulfide Mineralogy and Geochemistry*, 61, p. 633–677.  
1616 Mineralogical Society of America.
- 1617 Shen, Y., Buick, R., and Canfield, D.E. (2001) Isotopic evidence for microbial sulphate reduction in the  
1618 early Archaean era. *Nature*, 410, 77–81. <https://doi.org/10.1038/35065071>.
- 1619 Shields-Zhou, G., and Och, L. (2011) The case for a Neoproterozoic Oxygenation Event: Geochemical  
1620 evidence and biological consequences. *GSA Today*, 21, 4–11. <https://doi.org/10.1130/gsatg102a.1>.
- 1621 Shields-Zhou, G.A., Hill, A.C., and Macgabhann, B.A. (2012) The Cryogenian Period. In F.M. Gradstein,  
1622 J.G. Ogg, M.D. Schmitz, and G.M. Ogg, Eds. *The Geologic Time Scale*, p. 393–411. Elsevier,  
1623 Boston, USA.
- 1624 Siegmund, H., and Erdtmann, B.-D. (1994) Facies and diagenesis of some Upper Proterozoic dolomites  
1625 of South China. *Facies*, 31, 255–263. <https://doi.org/10.1007/bf02536942>.
- 1626 Sim, M.S., Bosak, T., and Ono, S. (2011a) Large sulfur isotope fractionation does not require  
1627 disproportionation. *Science*, 333, 74–77. <https://doi.org/10.1126/science.1205103>.
- 1628 Sim, M.S., Ono, S., and Bosak, T. (2012) Effects of iron and nitrogen limitation on sulfur isotope  
1629 fractionation during microbial sulfate reduction. *Applied and environmental microbiology*, 78, 8368-  
1630 8376. <https://doi.org/10.1128/AEM.01842-12>.

- 1631 Sim, M.S., Ono, S., Donovan, K., Templer, S.P., and Bosak, T. (2011b) Effect of electron donors on the  
1632 fractionation of sulfur isotopes by a marine *Desulfovibrio* sp. *Geochimica et Cosmochimica Acta*, 75,  
1633 4244–4259. <https://doi.org/10.1016/j.gca.2011.05.021>.
- 1634 Song, G., Wang, X., Shi, X., and Jiang, G. (2017) New U-Pb age constraints on the upper Banxi Group  
1635 and synchrony of the Sturtian glaciation in South China. *Geoscience Frontiers*, 8, 1161–1173.  
1636 <https://doi.org/10.1016/j.gsf.2016.11.012>.
- 1637 Sośnicka, M., and Lüders, V. (2018) Super-deep, TSR-controlled Phanerozoic MVT type Zn-Pb deposits  
1638 hosted by Zechstein reservoir carbonate, Lower Saxony Basin, Germany. *Chemical Geology*, in  
1639 press. <https://doi.org/10.1016/j.chemgeo.2018.04.025>.
- 1640 Sunagawa, I., Endo, Y., and Nakai, N. (1971) Hydrothermal Synthesis of Framboidal Pyrite. Society of  
1641 Mining Geologists of Japan, Special Issue, Proceedings of the IMA-IAGOD meetings '70, Joint  
1642 Symposium, 1, p. 10–14.
- 1643 Tang, S. (1990) Isotope geological study of manganese deposit in Minle area, Hunan Province. *Acta*  
1644 *Sedimentologica Sinica*, 8, 77–84 (in Chinese with English abstract).
- 1645 Tang, S., and Liu, T. (1999) Origin of the early Sinian Minle manganese deposit, Hunan Province, China.  
1646 *Ore Geology Reviews*, 15, 71–78. [https://doi.org/10.1016/S0169-1368\(99\)00015-3](https://doi.org/10.1016/S0169-1368(99)00015-3).
- 1647 Tompkins, L.A., Rayner, M.J., Groves, D.I., and Roche, M.T. (1994) Evaporites: In situ sulfur source for  
1648 rhythmically banded ore in the Cadjebut Mississippi Valley-type Zn-Pb deposit, Western Australia.  
1649 *Economic Geology*, 89, 467–492. <https://doi.org/10.2113/gsecongeo.89.3.467>.
- 1650 Ushikubo, T., Williford, K.H., Farquhar, J., Johnston, D.T., Van Kranendonk, M.J., and Valley, J.W.  
1651 (2014) Development of in situ sulfur four-isotope analysis with multiple Faraday cup detectors by  
1652 SIMS and application to pyrite grains in a Paleoproterozoic glaciogenic sandstone. *Chemical*  
1653 *Geology*, 383, 86–99. <https://doi.org/10.1016/j.chemgeo.2014.06.006>.
- 1654 Valley, J.W., and Kita, N.T. (2009) In situ oxygen isotope geochemistry by ion microprobe. In M. Fayek,  
1655 Ed. *Secondary Ion Mass Spectrometry in the Earth Sciences – Gleaning the Big Picture from a Small*  
1656 *Spot*, 41, p. 19–63. Mineralogical Association of Canada Short Course 41, Toronto.
- 1657 Wacey, D., Kilburn, M.R., Saunders, M., Cliff, J.B., Kong, C., Liu, A.G., Matthews, J.J., and Brasier,  
1658 M.D. (2015) Uncovering framboidal pyrite biogenicity using nano-scale CN<sub>org</sub> mapping. *Geology*, 43,  
1659 27–30. <https://doi.org/10.1130/g36048.1>.
- 1660 Wacey, D., McLoughlin, N., Whitehouse, M.J., and Kilburn, M.R. (2010) Two coexisting sulfur  
1661 metabolisms in a ca. 3400 Ma sandstone. *Geology*, 38, 1115–1118. <https://doi.org/10.1130/g31329.1>.
- 1662 Walter, M.R., Veevers, J.J., Calver, C.R., Gorjan, P., and Hill, A.C. (2000) Dating the 840–544 Ma  
1663 Neoproterozoic interval by isotopes of strontium, carbon, and sulfur in seawater, and some  
1664 interpretative models. *Precambrian Research*, 100, 371–433. [https://doi.org/10.1016/S0301-9268\(99\)00082-0](https://doi.org/10.1016/S0301-9268(99)00082-0).
- 1665
- 1666 Wang, J., and Li, Z.-X. (2003) History of Neoproterozoic rift basins in South China: implications for  
1667 Rodinia break-up. *Precambrian Research*, 122, 141–158. [https://doi.org/10.1016/S0301-9268\(02\)00209-7](https://doi.org/10.1016/S0301-9268(02)00209-7).
- 1668
- 1669 Wang, L., Liu, C., and Zhang, H. (2013) Tectonic and sedimentary settings of evaporites in the Dengying  
1670 Formation, South China Block: Implications for the potential of potash formation. *Acta Geoscientica*  
1671 *Sinica*, 34, 585–593 (in Chinese with English abstract).
- 1672 Wang, P., Du, Y., Algeo, T.J., Yu, W., Zhou, Q., Xu, Y., and Yuan, L. (2017) Post-Sturtian Sulfur  
1673 Isotope Anomalies in the Nanhua Basin, South China Related to Upward H<sub>2</sub>S Migration. *Geological*  
1674 *Society of America Abstracts with Programs*. Vol. 49, No. 6, Seattle, Washington, USA, 2017.
- 1675 Wang, P., Zhou, Q., Du, Y., Yu, W., Xu, Y., Qi, L., and Yuan, L. (2016) Characteristics of pyrite sulfur  
1676 isotope of Mn deposit from datangpo formation in Songtao area, East Guizhou Province and its  
1677 geological significance. *Earth Science - Journal of China University of Geosciences*, 41, 2031–2040  
1678 (in Chinese with English abstract). <https://doi.org/10.3799/dqkx.2016.142>.
- 1679 Wang, Y., Wang, L., and Zhu, S. (1985) *The Stratigraphy, Sedimentary Environment and Manganese-*  
1680 *Forming Process of the Datangpo Formation in Eastern Guizhou*. 92 p. People's Publishing House of  
1681 Guizhou, Guiyang (in Chinese)

- 1682 Watanabe, Y., Farquhar, J., and Ohmoto, H. (2009) Anomalous fractionations of sulfur isotopes during  
1683 thermochemical sulfate reduction. *Science*, 324, 370–373. <https://doi.org/10.1126/science.1169289>.
- 1684 Wilkin, R., and Barnes, H. (1997) Formation processes of framboidal pyrite. *Geochimica et*  
1685 *Cosmochimica Acta*, 61, 323–339. [https://doi.org/10.1016/s0016-7037\(96\)00320-1](https://doi.org/10.1016/s0016-7037(96)00320-1).
- 1686 Wilkin, R.T., Barnes, H.L., and Brantley, S.L. (1996) The size distribution of framboidal pyrite in modern  
1687 sediments: An indicator of redox conditions. *Geochimica et Cosmochimica Acta*, 60, 3897–3912.  
1688 [https://doi.org/10.1016/0016-7037\(96\)00209-8](https://doi.org/10.1016/0016-7037(96)00209-8).
- 1689 Williford, K.H., Ushikubo, T., Lepot, K., Kitajima, K., Hallmann, C., Spicuzza, M.J., Kozdon, R.,  
1690 Eigenbrode, J.L., Summons, R.E., and Valley, J.W. (2016) Carbon and sulfur isotopic signatures of  
1691 ancient life and environment at the microbial scale: Neoproterozoic shales and carbonates. *Geobiology*,  
1692 14, 105–128. <https://doi.org/10.1111/gbi.12163>.
- 1693 Williford, K.H., Van Kranendonk, M.J., Ushikubo, T., Kozdon, R., and Valley, J.W. (2011) Constraining  
1694 atmospheric oxygen and seawater sulfate concentrations during Paleoproterozoic glaciation: In situ  
1695 sulfur three-isotope microanalysis of pyrite from the Turee Creek Group, Western Australia.  
1696 *Geochimica et Cosmochimica Acta*, 75, 5686–5705. <https://doi.org/10.1016/j.gca.2011.07.010>.
- 1697 Wing, B.A., and Halevy, I. (2014) Intracellular metabolite levels shape sulfur isotope fractionation during  
1698 microbial sulfate respiration. *Proceedings of the National Academy of Sciences*, 111, 18116–18125.  
1699 <https://doi.org/10.1073/pnas.1407502111>.
- 1700 Worden, R.H., and Smalley, P.C. (1996) H<sub>2</sub>S-producing reactions in deep carbonate gas reservoirs: Khuff  
1701 Formation, Abu Dhabi. *Chemical Geology*, 133, 157–171. [https://doi.org/10.1016/S0009-2541\(96\)00074-5](https://doi.org/10.1016/S0009-2541(96)00074-5).
- 1702 Worden, R.H., Smalley, P.C., and Cross, M.M. (2000) The Influence of Rock Fabric and Mineralogy on  
1703 Thermochemical Sulfate Reduction: Khuff Formation, Abu Dhabi. *Journal of Sedimentary Research*,  
1704 70, 1210–1221. <https://doi.org/10.1306/110499701210>.
- 1705 Worden, R.H., Smalley, P.C., and Oxtoby, N.H. (1995) Gas souring by thermochemical sulfate reduction  
1706 at 140 °C. *AAPG Bulletin*, 79, 854–863.
- 1707 Wortmann, U.G., Bernasconi, S.M., and Böttcher, M.E. (2001) Hypersulfidic deep biosphere indicates  
1708 extreme sulfur isotope fractionation during single-step microbial sulfate reduction. *Geology*, 29, 647-  
1709 650. [https://doi.org/10.1130/0091-7613\(2001\)029<0647:HDBIES>2.0.CO;2](https://doi.org/10.1130/0091-7613(2001)029<0647:HDBIES>2.0.CO;2).
- 1710 Wu, C., Cheng, Y., Zhang, Z., Xiao, J., Fu, Y., Shao, S., Zheng, C., and Yao, J. (2015a) Geological  
1711 implications of ultra-high  $\delta^{34}\text{S}$  values of pyrite in manganese deposits of Nanhua Period in eastern  
1712 Guizhou and adjacent areas, China. *Geochimica*, 44, 213–224 (in Chinese with English abstract).
- 1713 Wu, C., Zhang, Z., Xiao, J., Fu, Y., Shao, S., Zheng, C., Yao, J., and Xiao, C. (2016) Nanhua manganese  
1714 deposits within restricted basins of the southeastern Yangtze Platform, China: Constraints from  
1715 geological and geochemical evidence. *Ore Geology Reviews*, 75, 76–99.  
1716 <https://doi.org/10.1016/j.oregeorev.2015.12.003>.
- 1717 Wu, N., Farquhar, J., and Fike, D.A. (2015b) Ediacaran sulfur cycle: Insights from sulfur isotope  
1718 measurements ( $\Delta^{33}\text{S}$  and  $\delta^{34}\text{S}$ ) on paired sulfate–pyrite in the Huqf Supergroup of Oman.  
1719 *Geochimica et Cosmochimica Acta*, 164, 352–364. <https://doi.org/10.1016/j.gca.2015.05.031>.
- 1720 Xi, X. (1987) Characteristic and Environments of Sinian Evaporite in Southern Sichuan, China. In T.M.  
1721 Peryt, Ed. *Lecture Notes in Earth Sciences: Evaporite Basins*, p. 23–29. Springer-Verlag Berlin  
1722 Heidelberg, Berlin.
- 1723 Xiao, S. (2014) Oxygen and early animal evolution. In H.D. Holland, and K.K. Turekian, Eds. *Treatise on*  
1724 *Geochemistry* (2nd Edition), vol. 6 (The Atmosphere - History), 6(The Atmosphere - History), p.  
1725 231–250. Elsevier, Oxford.
- 1726 Xiao, S., Narbonne, G.M., Zhou, C., Laflamme, M., Grazhdankin, D.V., Moczyłowska-Vidal, M., and  
1727 Cui, H. (2016) Toward an Ediacaran time scale: Problems, protocols, and prospects. *Episodes*, 39,  
1728 540–555. <https://doi.org/10.18814/epiiugs/2016/v39i4/103886>.
- 1729 Xiao, S., Zhou, C., and Zhu, M. (2014) International Symposium and Field Workshop on Ediacaran and  
1730 Cryogenian Stratigraphy. *Episodes*, 37, 218–221.
- 1731

- 1732 Xie, Q.-L., Chen, D.-F., and Chen, X.-P. (1999) Characteristics of sedimentary organic matter in Songtao  
1733 manganese deposits, Guizhou. *Acta Sedimentologica Sinica*, 17, 280–284 (in Chinese with English  
1734 abstract).
- 1735 Xie, X.-F., Qin, Y., Wen, G.-G., and Xie, X.-Y. (2014) Relation between Datangpo Formation and  
1736 manganese mineralization in Songtao manganese mining area of Tongren in Guizhou. *Guizhou  
1737 Geology*, 31, 32–37 (in Chinese with English abstract).
- 1738 Xu, X., Huang, H., and Liu, B. (1990) Manganese deposits of the Proterozoic Datangpo Formation, South  
1739 China: genesis and palaeogeography. In J. Parnell, L. Ye, and C. Chen, Eds. *Sediment-Hosted  
1740 Mineral Deposits*, 11, p. 39–50. The International Association of Sedimentologists, Blackwell  
1741 Publishing Ltd., Oxford, UK.
- 1742 Yang, R., Ouyang, Z., Zhu, L., Wang, S., Jiang, L., Zhang, W., and Gao, H. (2002) A new understanding  
1743 of manganese carbonate deposits in early Sinian Datangpo Stage. *Acta Mineralogica Sinica*, 22, 329–  
1744 334 (in Chinese with English abstract).
- 1745 Yin, C., Wang, Y., Tang, F., Wan, Y., Wang, Z., Gao, L., Xing, Y., and Liu, P. (2006) SHRIMP II U-Pb  
1746 zircon date from the Nanhuan Datangpo Formation in Songtao County, Guizhou Province. *Acta  
1747 Geologica Sinica*, 80, 273–278 (in Chinese with English abstract).
- 1748 Yu, W., Algeo, T.J., Du, Y., Zhou, Q., Wang, P., Xu, Y., Yuan, L., and Pan, W. (2017) Newly discovered  
1749 Sturtian cap carbonate in the Nanhua Basin, South China. *Precambrian Research*, 293, 112–130.  
1750 <https://doi.org/10.1016/j.precamres.2017.03.011>.
- 1751 Yuan, Y.-S., Ma, Y.-S., Hu, S.-B., Guo, T.-L., and Fu, X.-Y. (2006) Present-day geothermal  
1752 characteristics in South China. *Chinese Journal of Geophysics*, 49, 1005–1014.  
1753 <https://doi.org/10.1002/cjg2.922>.
- 1754 Zhang, F., 2014, The Formation Mechanism of Datangpo Manganese Ore Deposits during Nanhua Period  
1755 in South China and the Paleo-redox Conditions of Nanhua Marine Basin: Master Degree Thesis (in  
1756 Chinese with English abstract), Chinese Academy of Geological Sciences, Beijing, 121 p.
- 1757 Zhang, F., Zhu, X., Gao, Z., Cheng, L., Peng, Q., and Yang, D. (2013) Implications of the precipitation  
1758 mode of manganese and ultra-high  $\delta^{34}\text{S}$  values of pyrite in Mn-carbonate of Xixibao Mn ore deposit  
1759 in Northeastern Guizhou Province. *Geological Review*, 59, 274–286 (in Chinese with English  
1760 abstract).
- 1761 Zhang, M., Konishi, H., Xu, H., Sun, X., Lu, H., Wu, D., and Wu, N. (2014) Morphology and formation  
1762 mechanism of pyrite induced by the anaerobic oxidation of methane from the continental slope of the  
1763 NE South China Sea. *Journal of Asian Earth Sciences*, 92, 293–301.  
1764 <https://doi.org/10.1016/j.jseaes.2014.05.004>.
- 1765 Zhang, S., Jiang, G., and Han, Y. (2008) The age of the Nantuo Formation and Nantuo glaciation in South  
1766 China. *Terra Nova*, 20, 289–294. <https://doi.org/10.1111/j.1365-3121.2008.00819.x>.
- 1767 Zhou, C., Tucker, R., Xiao, S., Peng, Z., Yuan, X., and Chen, Z. (2004) New constraints on the ages of  
1768 Neoproterozoic glaciations in south China. *Geology*, 32, 437–440. <https://doi.org/10.1130/g20286.1>.
- 1769 Zhou, Q., Du, Y.-S., Wang, J.-S., and Peng, J.-Q. (2007) Characteristics and significance of the cold seep  
1770 carbonates from the Datangpo Formation of the Nanhua series in the northeast Guizhou. *Earth  
1771 Science - Journal of China University of Geosciences*, 32, 339–346 (in Chinese with English  
1772 abstract). <https://doi.org/10.3321/j.issn:1000-2383.2007.03.006>.
- 1773 Zhou, Q., Du, Y., and Qin, Y. (2013) Ancient natural gas seepage sedimentary-type manganese  
1774 metallogenic system and ore-forming model: A case study of Datangpo type manganese deposits  
1775 formed in rift basin of Nanhua Period along Guizhou-Hunan-Chongqing border area. *Mineral  
1776 Deposits*, 32, 457–466 (in Chinese with English abstract). [https://doi.org/10.16111/j.0258-  
1777 7106.2013.03.001](https://doi.org/10.16111/j.0258-7106.2013.03.001).
- 1778 Zhu, G., Wang, T., Xie, Z., Xie, B., and Liu, K. (2015) Giant gas discovery in the Precambrian deeply  
1779 buried reservoirs in the Sichuan Basin, China: Implications for gas exploration in old cratonic basins.  
1780 *Precambrian Research*, 262, 45–66. <https://doi.org/10.1016/j.precamres.2015.02.023>.

- 1781 Zhu, G., Zhang, S., Liang, Y., and Li, Q. (2007a) The genesis of H<sub>2</sub>S in the Weiyuan Gas Field, Sichuan  
1782 Basin and its evidence. Chinese Science Bulletin, 52, 1394-1404. [https://doi.org/10.1007/s11434-](https://doi.org/10.1007/s11434-007-0185-1)  
1783 [007-0185-1](https://doi.org/10.1007/s11434-007-0185-1).
- 1784 Zhu, G., Zhao, W., Zhang, S., Liang, Y., and Wang, Z. (2007b) Discussion of gas enrichment mechanism  
1785 and natural gas origin in marine sedimentary basin, China. Chinese Science Bulletin, 52, 62-76.  
1786 <https://doi.org/10.1007/s11434-007-6016-6>.
- 1787 Zhu, X., Peng, Q., Zhang, R., An, Z., Zhang, F., Yan, B., Li, J., Gao, Z., Tan, Y., and Pan, W. (2013)  
1788 Geological and geochemical characteristics of the Daotuo super-large manganese ore deposit at  
1789 Songtao County in Guizhou Province. Acta Geologica Sinica, 87, 1335–1348 (in Chinese with  
1790 English abstract).
- 1791